

## INFORMATION TO USERS

This dissertation was produced from a microfilm copy of the original document. While the most advanced technological means to photograph and reproduce this document have been used, the quality is heavily dependent upon the quality of the original submitted.

The following explanation of techniques is provided to help you understand markings or patterns which may appear on this reproduction.

1. The sign or "target" for pages apparently lacking from the document photographed is "Missing Page(s)". If it was possible to obtain the missing page(s) or section, they are spliced into the film along with adjacent pages. This may have necessitated cutting thru an image and duplicating adjacent pages to insure you complete continuity.
2. When an image on the film is obliterated with a large round black mark, it is an indication that the photographer suspected that the copy may have moved during exposure and thus cause a blurred image. You will find a good image of the page in the adjacent frame.
3. When a map, drawing or chart, etc., was part of the material being photographed the photographer followed a definite method in "sectioning" the material. It is customary to begin photoing at the upper left hand corner of a large sheet and to continue photoing from left to right in equal sections with a small overlap. If necessary, sectioning is continued again — beginning below the first row and continuing on until complete.
4. The majority of users indicate that the textual content is of greatest value, however, a somewhat higher quality reproduction could be made from "photographs" if essential to the understanding of the dissertation. Silver prints of "photographs" may be ordered at additional charge by writing the Order Department, giving the catalog number, title, author and specific pages you wish reproduced.

### **University Microfilms**

300 North Zeeb Road  
Ann Arbor, Michigan 48106

A Xerox Education Company

72-19,018

CHARBA, Jerome Paul, 1944-  
GRAVITY CURRENT MODEL APPLIED TO ANALYSIS  
OF SQUALL-LINE GUST FRONT.

The University of Oklahoma, Ph.D., 1972  
Meteorology

University Microfilms, A XEROX Company, Ann Arbor, Michigan

THE UNIVERSITY OF OKLAHOMA  
GRADUATE COLLEGE

GRAVITY CURRENT MODEL APPLIED TO ANALYSIS  
OF SQUALL-LINE GUST FRONT

A DISSERTATION  
SUBMITTED TO THE GRADUATE FACULTY  
in partial fulfillment of the requirements for the  
degree of  
DOCTOR OF PHILOSOPHY


BY  
JEROME PAUL CHARBA

Norman, Oklahoma

1972

GRAVITY CURRENT MODEL APPLIED TO ANALYSIS  
OF SQUALL-LINE GUST FRONT

APPROVED BY

  
Philip S. Gage  
M. L. Rasmussen  
Stanley L. Barnes

**PLEASE NOTE:**

Some pages may have

indistinct print.

Filmed as received.

**University Microfilms, A Xerox Education Company**

## DEDICATION

To my sister, Charlene, and brother-in-law, C. T. Dawson, who provided the initial opportunity and encouragement to pursue a university education. For this I am forever grateful.

## ACKNOWLEDGMENTS

The author extends sincere appreciation to Professor Yoshikazu Sasaki whose timely personal encouragement and technical guidance were major contributions towards the undertaking and completion of this research. He also deserves credit for stimulating me to actively participate in the Fifth and Seventh Severe Local Storms Conferences, in NSSL's field observation programs, and in Mr. Abe Bernstein's (Air Resources Lab) field experiments. This involvement provided valuable experience and inspiration for pursuing this research.

The author is deeply indebted to all the NSSL personnel who were responsible for gathering the data used in this study. Special thanks are due to Dr. Edwin Kessler, NSSL director, who made available the data and provided the use of NSSL's special equipment for aiding the data analysis. Mr. J. T. Dooley's responsiveness in assembling the data packages and assisting in the data interpretation is especially appreciated. Dr. S. L. Barnes, Mr. K. E. Wilk, and Mr. D. Sanders contributed many helpful suggestions and criticisms during the course of this research.

It is a pleasure to acknowledge with thanks the contributions of fellow students, staff, and faculty members. Discussions of thorny theoretical problems with Don Holyoke and analytical results with Bill Parton were quite useful. Consultations with Bob Sheets on aspects of the data smoothing were particularly helpful. Credit is due to Carlos

Droescher who performed the superb drafting of the figures. Keven Amrein is complimented for her diligence in the manuscript typing.



TABLE OF CONTENTS

	Page
LIST OF TABLES. . . . .	vii
LIST OF ILLUSTRATIONS . . . . .	viii
ABSTRACT. . . . .	x
 Chapter	
I. INTRODUCTION. . . . .	1
II. METHODS OF DATA PROCESSING AND ANALYSIS . . . . .	4
III. EVOLUTION OF THE SQUALL LINE WITHIN THE LARGE SCALE PATTERN . . . . .	10
IV. EVOLUTION OF THE SQUALL-LINE THUNDERSTORMS AND THE GUST FRONT WHICH ENTERED THE NETWORK. . . . .	13
V. ANALYTICAL STRUCTURE OF THE THUNDERSTORM OUTFLOW LEADING THE SQUALL LINE . . . . .	18
VI. APPLICATION OF THEORIES AND MODELS TO THE ANALYSIS. . .	30
VII. SUMMARY . . . . .	56
BIBLIOGRAPHY. . . . .	60

LIST OF TABLES

Table	Page
1. Storm damage reports. . . . .	63
2. Radar echo properties of damaging thunderstorms . . . .	64
3. Gravity current relationships applied to the gust- front air mass. . . . .	65

## LIST OF ILLUSTRATIONS

Illustration	Page
1. High density, surface observation network, and instrumented TV-tower facility . . . . .	66
2. Sub-synoptic section maps: (a) and (b) . . . . .	67
" " " (c) and (d) . . . . .	68
" " " (e) and (f) . . . . .	69
" " " (g) and (h) . . . . .	70
" " " (i) and (j) . . . . .	71
3. Sequence of frontal positions . . . . .	72
4. Time sequence of radar echo pictures of the 31 May 1969 squall line . . . . .	73
5. Pattern of tracks of peak echo-reflectivity elements .	74
6. Time sequence of PPI displays showing the "thin line" echo propagating ahead of the heavy precipitation echoes . . . . .	75
7. Schematic of major analytical surface features of squall line at 2337½ CST . . . . .	76
8. Sequence of the windshift and gust-surge isochrones. .	77
9. Network and tower wind analysis: (a) . . . . .	78
" " " " " (b) . . . . .	79
" " " " " (c) . . . . .	80
" " " " " (d) . . . . .	81
" " " " " (e) . . . . .	82
" " " " " (f) . . . . .	83
" " " " " (g) . . . . .	84
" " " " " (h) . . . . .	85
10. Spatial variations of surface wind, pressure, and temperature across the gust front. . . . .	86
11. Network and tower temperature analysis: (a) . . . . .	88
" " " " " (b) . . . . .	89
" " " " " (c) . . . . .	90
12. Surface pressure analysis. . . . .	91

13. Schematic of important analytical features of the leading part of the squall line. . . . .	92
14. Comparison of the observed and theoretical pressure jump of 31 May 1969. . . . .	93
15. Vertical profiles of temperature and density at WKY. .	94
16. A saline "density current" (gravity current) undercutting pure water in a transparent tank . . . . .	95
17. Atmospheric gravity currents . . . . .	96
18. Schematic flow model of a gravity current. . . . .	97
19. A composite analysis of a cold front in Australia. . .	98
20. Internal circulation regime of laboratory gravity currents . . . . .	99
21. A composite model of the analysis of the windshift and gust front leading the squall line of 31 May 1969. . .	100

## ABSTRACT

The structure of a severe gust front which led the squall line of 31 May 1969 is examined from analysis of measurements from the National Severe Storm Laboratory (NSSL) network of surface stations located in central Oklahoma. Utilizing the analysis of the structure and the horizontal displacement of the cold outflow air mass, the mechanics of motion of the gust front is investigated.

In a vertical plane normal to the leading edge of the cold-air current the following analytical features were revealed. The front edge of the profile of the air-mass surface exhibited a projecting "nose" overlying the lagging front at the ground. Along the top, the air-mass profile featured a height maximum of 1700 m near the front ("head") followed by a near-constant upstream height of 1350 m. The wind pattern with respect to a coordinate axis translating with the head at  $20 \text{ m sec}^{-1}$  displayed (a) a strong ambient-air flow towards the nose which was lifted over the head (upward velocities at 400 m above the ground were up to  $2.5 \text{ m sec}^{-1}$ ), (b) a closed circulation cell within the head, dominated by a high-speed forward current along the bottom as exhibited by a  $13 \text{ m sec}^{-1}$  current only 180 m above the ground. Upstream cold air flowed into the head circulation field, apparently maintaining the cold air against erosion effects resulting

from (c) turbulent entrainment of ambient air below the nose and, more importantly, in the wake of the head crest. These analytical features are remarkably similar to analogous characteristics of gravity currents in stratified fluids produced in laboratory experiments by Keulegan (1958), Middleton (1966) and Simpson (1969).

The gust front was found to be in approximate dynamic similarity to theoretical and experimental gravity currents. In this regard, it is speculated that high horizontal-momentum air in the thunderstorm downdraft, injected into the outflow current, has the tendency to increase the gust front's propagational speed and thus its internal Froude number from that which it would have if gravity were the only motive force. However, analytical evidence indicates this effect was small in the 31 May case.

GRAVITY CURRENT MODEL APPLIED TO ANALYSIS  
OF SQUALL-LINE GUST FRONT

CHAPTER I

INTRODUCTION

As air transport has been mushrooming during recent years, an increasingly serious air traffic congestion problem near airports is often aggravated by the potential danger posed by the cold outflow of a nearby thunderstorm. Among aviators it is commonly agreed that the strong low-level wind gusts and the extreme wind shears which characterize this air mass pose a serious hazard to aircraft in their landing or take-off patterns. This problem has recently spurred some meteorologists to a renewed interest in this severe wind phenomenon (Fujita, 1966; Barclay and Wilk, 1970; Sasaki, 1970; and Colmer, 1971). Because of its characteristic gusty winds this cold outflow air mass has been called gust front by the above researchers. In this paper the term gust front is adopted for general reference to this cold airmass.

A scan of the meteorological literature for documented studies on the severe low-level winds associated with thunderstorms points up a need for further investigation. Byers and Braham (1949) made detailed analyses of the surface wind fields of an assortment of convective storms in Florida and Ohio and were among the first to serve notice of the potential

danger posed by such winds to aircraft. Barclay and Wilk (1970) and Sasaki (1970) emphasized the structural aspects of severe surface wind fields revealed by objective analysis of several squall-line cases. Fujita (1966) examined the turbulence structure of a squall-line gust front in the layer 1-2 km above the ground from aircraft flight records. Colmer (1971) investigated a few key features of the structure of the initial gust in the surface-to-500 m layer in 13 gust-front cases. There remains a need for a complete definition of the structure of kinematic and thermodynamic variables in three dimensions. Furthermore, with a view towards improved forecasting of the gust front, it will be necessary to obtain a better understanding of the mechanism of formation and maintenance of the gusty air mass and to clarify the mechanics of its horizontal propagation outward from the parent storm.

This study is a detailed analysis of the structure and horizontal propagation of the severe gust front connected with the squall line of 31 May 1969. The wind and thermal fields of the outflow air mass are analyzed in three dimensions. Important features of these fields are compared to corresponding fields of gravity currents formed in laboratory tank experiments by Keulegan (1958), Middleton (1966) and Simpson (1969) and in a numerical simulation by Daley and Pracht (1968). The investigation touches on the mechanism of formation of the gust front as well as the mechanism involved in its subsequent maintenance during a horizontal displacement spanning about 100 nm. The dynamical relationship between the horizontal momentum of the airmass and the horizontal hydrostatic pressure gradient across the frontal surface is examined at length. The clarification of these aspects is implemented by applying the theory of gravity currents formulated by von Kármán (1940) and Prandtl (1952), and Benjamin (1968) to the analytical structure of the gust front. Theoretical results from this



application are then compared to experimental observations of gravity currents.

To the author's knowledge, such an investigation of the cold air outflow of thunderstorms has heretofore not appeared in the literature. This is undoubtedly due mainly to the scarcity of high resolution measurements, especially in the vertical direction. On the other hand similar investigations (but in less detail) have been made of larger scale atmospheric gravity-type flows, e.g., seabreeze fronts and the leading edge of cold fronts, by Berson (1958), Clarke (1961), and Simpson (1969). This study considers some of the fundamental similarities and differences between the structure and dynamic character of these phenomena and the gust front.

## CHAPTER II

### METHODS OF DATA PROCESSING AND ANALYSIS

#### Special Data Utilized

The special data provided for this study by NSSL was of three types: radar scope photographs, surface mesonet network, and tall-tower measurements.

NSSL made available radar scope photographs of the horizontally scanning WSR-57 and vertically scanning MPS-4. The PPI (plan-position indicator) of the WSR-57 was photographed with each 1-min scan and the RHI (range-height indicator) of the MPS-4 was also filmed at intervals of 1 min. This radar coverage, to a maximum range of 100 nm in all directions from Norman, Oklahoma (NRO), gave a complete picture of the development and ensuing approach of the squall line towards surface station network from the west-northwest direction. Volunteer observer reports and Storm Data tabulations of severe weather and damage inflicted by the thunderstorms were used in conjunction with the radar pictures for identification of severe echoes. Each year NSSL sends standard checklist forms to about 400 volunteer observers located within the area of radar coverage. Although it is not known exactly how many persons receiving the forms respond to them, the large number of reports received by NSSL combined with additional reports compiled in Storm Data gives reasonable assurance that large severe storms were not missed. The severe weather reports connected with the 31 May 1969 squall-line echoes are shown in Fig. 2 and in Tables 1

and 2.

The analysis of the squall-line gust front utilized measurements obtained from NSSL's high density network of surface stations and the tall, instrumented WKY-TV tower shown in Fig. 1. The average distance between adjacent surface stations in 1969 was 9 km. Surface wind, pressure, temperature, relative humidity and rainfall measurements were recorded automatically at each station on strip charts in analog form. NSSL maintenance personnel took a high degree of care in 1969 to insure instrument calibration to meet National Weather Service (NWS) standards and chart time accuracy to  $\pm 1$  min. Instruments at seven level of the tower recorded wind and temperature measurements to a maximum height of 444.4 m (see Carter, 1970 for complete description). Accuracy of the tower records easily exceeded the requirements for this analysis.

#### Data Extraction and Smoothing

The pressure and wind data extracted from the analog charts were smoothed in order to remove small scale random variations. In the case of the station pressure the microbarogram was digitized at 1.25-min intervals and then smoothed by the application of a three-point "hanning" filter designed to remove waves whose periods are less than 2.5 min (or 3 km wavelength).<sup>1</sup> The wind records were smoothed directly by hand in accordance with the criterion of removing waves of periods up to 2.5 min. These smoothed data define the "characteristic" pressure and wind of the gust front.

During the period of the gust-front passage the wind speed records exhibited large amplitude fluctuations. At a particular analysis time the

---

<sup>1</sup>The short-term transformation from the time to the space domain assumes steadiness of the measured gust-front parameters over the short time interval involved.

maximum and/or minimum wind speed was defined as an average of the consecutive speed peaks and/or consecutive speed minima, respectively, over a time interval of 2.5 min centered at the analysis time. These maximum and minimum wind speed data are utilized as a measure of the wind gustiness (discussed later).

#### Time-to-Space Conversions

Conversions of chart records from the time to the space dimension were employed in the analysis of both the network and tower measurements. The method is discussed by Fujita (1963) and employed in network analysis by Charba and Sasaki (1971). This method of utilizing continuous measurements at a station for extrapolation to points between stations was found to be necessary for accurate analysis of wavelengths as short as 12 km.<sup>1</sup> The conversion from the time to the space dimension was similarly applied to WKY tower records to implement the analysis of the wind and thermal structure of the gust front in a vertical plane section.

#### Special Analysis Techniques

The procedure followed in the analysis of parameters derived from the wind measurements and the method used to analyze the surface pressure field require elaboration. Discussed first are the procedures used to obtain the divergence and streamline fields of the surface wind and the stream function and gustiness fields of tower winds in a vertical plane normal to

---

<sup>1</sup>The plotted data fields used to construct the surface patterns appearing in Figs. 9-13 are not shown due to the lack of space. However, the reader can see the basis of the analyzed patterns from analog records (at several selected stations) in which the time dimension is converted to the space dimension in the direction of displacement of the gust front. The stations selected and the section lines along the direction of displacement are shown in Fig. 7 while the sections showing the variations of pertinent surface parameters are shown in Fig. 10.

the leading edge of the gust front (x-direction; see Fig. 7 for coordinate orientations).

The computation of the surface wind divergence employed a rectangular grid whose spacing was 5 km. The wind direction and speed was interpolated at grid-point locations from isogon and isotach patterns (Figs. 9a and 9e). The horizontal velocity divergence at grid point  $i, j$  is computed according to

$$\text{Div}_{i,j} = (u_{i+1} - u_{i-1} + v_{j+1} - v_{j-1})/2d \quad (1)$$

where  $d$  is the grid spacing while  $u$  and  $v$  are the respective wind components normal (x-direction) and tangent (y-direction) to the leading edge of the gust front;  $i$  increases by 1 as  $x$  increases by  $d$  and likewise for  $j$  in the  $y$ -direction. The divergence field is shown in Fig. 9c.

Streamline patterns were constructed both at the surface level and in the vertical plane defined above. The streamlines representing the surface flow pattern were constructed entirely by hand from a field of plotted wind vectors (Fig. 9c). The spacing of the streamlines qualitatively shows the wind speed pattern, i.e., the closer the spacing the greater the wind speed. The computation of the stream function field was found to be valid in the  $x$ - $z$  plane in the vicinity of the gust surge since  $\frac{\partial v}{\partial y}$  was an order of magnitude smaller than  $\frac{\partial u}{\partial x}$  at the surface level. Assuming that  $\frac{\partial v}{\partial y}$  is negligibly small compared to  $\frac{\partial u}{\partial x}$  everywhere in the vertical plane from the surface to 444 m, the mass continuity equation for incompressible flow becomes

$$\frac{\partial u}{\partial x} + \frac{\partial w}{\partial z} = 0 \quad (2)$$

where the vertical velocity component,  $w$ , is positive in the upward ( $z$ ) direction. Following Clarke (1961) a stream function,  $\psi$ , satisfying (2) is defined by

$$u = - \frac{\partial \psi}{\partial z} \quad (3a)$$

$$w = \frac{\partial \psi}{\partial x} \quad (3b)$$

Since  $u$  is known as a function of height,  $h$ , in the  $x$ - $z$  plane from tower winds, the  $\psi$ -field is computed by

$$\psi = - \int_0^h u \, dz \quad (4)$$

After  $\psi$  has been computed  $w$  can be obtained from (3b). The stream function field is shown in Fig. 9d.

The gustiness,  $G$ , of the network and tower winds is defined by

$$G = \bar{V}_{\max} - \bar{V}_{\min}$$

where  $\bar{V}_{\max}$  and  $\bar{V}_{\min}$  are the respective 2.5-min averages of consecutive peak and minimum wind speed data defined earlier. Thus the gustiness represents the magnitude of wind speed fluctuation, i.e., gusts, about the characteristic wind speed. Analyzed fields of  $G$  are shown in Figs. 9g and h.

The analysis of surface pressure employed a special method which removes instrument calibration errors, eliminates the necessity of reducing the pressure to a common reference level, and separates the mesoscale disturbance from larger scale pressure changes. The removal of instrument calibration, pressure reduction, and scale separation problems for a particular station is accomplished at once by determining the actual station pressure trace representing large scale variations, i.e., wavelengths > 500 km. The latter pressure trace, called the pressure trend by Charba and Sasaki (1971), is subtracted from the original trace smoothed only to remove small-scale fluctuation, i.e., wavelengths < 3 km. The resulting pressure deviations from the trend represent the mesoscale disturbances in the

approximate wavelength range of 5-500 km. The entire process of obtaining the mesoscale pressure variation at a station for a particular analysis time, is accomplished in four steps; (i) the original trace is digitized at 45-min intervals over a time span of 24 hours centered on the storm event, (ii) the resulting discrete data set is smoothed by a centered nine-point moving average operator (this operator effectively removes waves of periods 12 hr and less), (iii) linear interpolation is used to obtain the pressure trend value for an analysis time between the smoothed points and (iv) the interpolated pressure trend value is subtracted from the corresponding ambient pressure value (previously smoothed only to remove small scale variations). This process is repeated for each network microbarogram to obtain the pressure deviations for all stations. The spatial variation of both the pressure trend and the smoothed ambient pressure within the gust front is shown for station WKY in Fig. 10a. The analysis of the surface pressure is shown in Fig. 12.

#### Concluding Comments on Analysis Approach

It is recalled that all the data extraction and much of the processing was performed manually. However, it is emphasized that objective criteria and techniques were established and employed as periodic checks on the hand processing to insure a relatively high degree of objectivity. Of course, the disadvantage inherent in the "hand" process is the tedious effort required. However, this disadvantage is to a great degree over-compensated by the more effective use of the experience and physical insight of the analyst in detecting key subtle features in the data records which might be left unnoticed or smoothed out if fully automated techniques were used. Such is the case in an analysis where little is known about the phenomenon prior to the investigation. This gust front analysis certainly falls into the above category.

## CHAPTER III

### EVOLUTION OF SQUALL LINE WITHIN LARGE SCALE PATTERN

#### Synoptic

The synoptic pattern which spawned the convective outbreak in the Southern Great Plains was typical for severe storm occurrences in that region. At 1800 CST, 31 May 1969 a vigorous late-season cold air mass was pushing southeastward across Colorado, Kansas, and Iowa behind a deep closed low pressure center located just west of Lake Superior. A low pressure trough extended southwestward from the low to El Paso, Texas at all tropospheric levels.

#### Sub-synoptic

The sub-synoptic pattern at 1800 CST over the area of interest is revealed in the section maps shown in Fig. 2 a-f. At the surface and 850 mb levels, a warm, moist southerly current is seen to meet the northerly cold-air surge over extreme northwest Oklahoma to eastern Kansas. Hot, dry air from west Texas was drifting towards western Oklahoma. At 500 mb weak cool-air advection was occurring over Kansas. The implied differential thermal and moisture advection in the vertical direction created a potentially unstable stratification as indicated by lifted index values of -3 and -4 at Dodge City (DDC) and Oklahoma City (OKC).<sup>1</sup>

---

<sup>1</sup>Whitehead (1971) employed this case to investigate the use of special indices to map areas of large potential instability for correlation with severe thunderstorm outbreaks.



Several mechanisms over western Oklahoma and Kansas evidently provided the upward air-motion which unleashed the potential instability. Among them was: (i) the mechanical lifting provided by the undercutting cold air mass. Fig. 3 illustrates the southward acceleration of the front which occurred during the afternoon and evening of 31 May. The southward push increased from 8.5 to 16.0 m sec<sup>-1</sup> across Colorado and the Texas panhandle. Certainly mechanical lifting was substantial in this area in the face of the southward cold-front push. Upward motion also occurred ahead of the front over the Texas panhandle and western Oklahoma in connection with convergence of the 850-mb flow into a low pressure area (div =  $-1.5 \times 10^{-11}$  sec<sup>-1</sup>) and divergence of the 500 mb flow ahead of a short wave trough (div =  $1.4 \times 10^{-4}$  sec<sup>-1</sup>) in that area. Upward motion was further aided in the area because of topographical upslope flow. Applying Sasaki's numerical variational analysis method to the NWS's synoptic rawinsonde network data, Maxwell (1971) and Sullivan (1971) obtained significant areas of upward motion along and ahead of the front in northwest Oklahoma and southern Kansas.

Thunderstorms made an initial appearance near the cold front in the extreme northwest panhandle of Oklahoma and southwest Kansas at about 1600 CST according to NWS radar summaries (see Whitehead, 1971 for complete details). A squall line rapidly formed and moved eastward at 15-20 m sec<sup>-1</sup>. This displacement speed is significantly greater than the mean wind in the troposphere revealed by two TIK (Tinker Air Force Base in Oklahoma City) soundings, 1800 CST 31 May and 0600 CST 1 June,

displaced 6 hr in time from the 0000 CST 1 June squall-line passage over the rawinsonde site. The mean wind vector revealed by these soundings had a magnitude of  $10 \text{ m sec}^{-1}$  from 262 deg. The 5-10  $\text{m sec}^{-1}$  discrepancy between the mean wind and the propagational speed of the cumulonimbi suggests that the rawinsonde winds were not representative of the steering current ambient to the squall-line thunderstorms. This is not surprising since a mesocyclone developed along the front in western Oklahoma and moved rapidly across the northern part of the state (Fig. 2h). The radar echoes embedded in the high-speed southern "wing" of the wave moved about 8-10  $\text{m sec}^{-1}$  faster than those to the north, in apparent association with the cyclonic circulation. By 0000 CST, the southern extension of the squall-line wave passed over the OKC-NRO area (Fig. 2e and f). The heavy rain area was preceded by a severe gust front which produced wind gusts up to  $35 \text{ m sec}^{-1}$  at the WKY tower. Note the intense pressure and temperature gradients normal to the squall line in central Oklahoma in Figs. 2h and 2i.

## CHAPTER IV

### EVOLUTION OF THE SQUALL-LINE THUNDERSTORMS AND GUST FRONT WHICH ENTERED THE NETWORK

The analysis of the network measurements and its subsequent interpretation was greatly aided by an initial investigation of the temporal variations in certain gust-front properties within the period encompassing the analysis time. This required the identification of the parent echo (which in the case of a squall line, may be a formidable task) so that the temporal and spatial variations of the intensity and propagational character of both the gust front and the parent thunderstorm could be described prior to the analysis. Towards this end diligent use is made of the NSSL radar pictures and volunteer observer and Storm Data reports.

#### Echo Patterns and Related Wind Damage

Among meteorologists possessing extensive experience with radar observations of severe thunderstorms, it is common knowledge that thunderstorms whose echoes are organized in a wave pattern are often severe. Nolen (1961) was first to recognize and define the line-echo-wave pattern (LEWP) as an echo feature often associated with occurrences of tornadoes. Cook (1961) found that tornadoes

are most likely to occur within a region 50 nm to the south of the crest of the fast-moving ( $\geq 40$  kt) LEWP particularly when the line is scattered or broken. Severe windstorms are predominate in the same area when the line is solid.

In the case of the 31 May - 1 June squall line, a distinct line-echo-wave pattern (LEWP) developed in western Oklahoma in apparent association with the mesocyclone discussed earlier. In Fig. 4a-c notice how the fast-moving echo A overtakes B during the period 2130-2300 CST; thereafter A and B eventually amalgamate. At the same time echo A grew continuously along its southern tip, and by 2330 a solid echo line extended 60 nm to the south of the point of amalgamation of A and B. While A and B were merging, A accelerated eastward relative to B, thus forming the LEWP. The relative vorticity within the echo wave, calculated from the differential displacements of peak reflectivity elements during the period 2255-2335 CST (Fig. 5) was  $+5.4 \times 10^{-4} \text{ sec}^{-1}$ . On the other hand, storm C, was obviously not part of the LEWP to the north of it and showed no wave configuration of its own.

Virtually all the severe wind damage appeared to be associated with the protruding wing of the LEWP, i.e., echo A, in agreement with the finds of Cook (1961). This is established from the volunteer observer and Storm Data wind damage reports compiled in Table 1. Greatest wind damage was reported from the Dover (DVR) area (report number 2d in Table 1 and Fig. 3). Notice that the leading edge of the protruding echo of the LEWP was just west of DVR when the high winds began. Quite in contrast, storm C apparently imparted relatively little wind destruction during the period spanned in Fig. 4.

### Echo Characteristics and Related Wind Damage

Focusing on the individual echoes within the squall line, there appears to be a definite correlation between certain echo properties and the severity of the wind damage. Table 2 lists the translation speed, prior active duration, echo diameter, height of top, and reflectivity of the echo which passed over the point of reported wind damage. The echo property having the clearest correlation to the wind damage is the translation speed. In Fig. 5 the echo speeds are indicated in bold numbers ( $\text{m sec}^{-1}$ ) below paths of peak reflectivity elements. Comparing this speed pattern to the damage pattern (Table 1 and Fig. 3) it is generally seen that the greater the rate of echo displacement the greater the wind damage and vice versa. Note the especially high echo speeds of  $25\text{-}30 \text{ m sec}^{-1}$  in the DVR area. Colmer (1971) observed a similar relationship from a plot of maximum wind gust versus echo speed obtained from 13 gust-front cases within the NSSL network in 1969-70. The remaining parameters in Table 2 also generally reveal a parallel between their magnitudes and the severity of the wind damage. Utilizing these relationships as criteria, it is inferred from Fig. 3 and Table 2 that echo A (LEWP) was in the mature stage during 2300-2315 CST but began to weaken by 2342 CST (Fig. 3g) just prior to entrance to the NSSL surface network.<sup>1</sup> This observation agrees with the reports of lesser wind damage downwind from A's 2342 CST position. On the other hand, storm C, which entered the southwestern part of the network was in its mature stage at 2342 CST but at no time indicated winds as strong as those associated with echo A.

---

<sup>1</sup>The appendage at the southern tip of echo A, i.e., echo A', made an initial appearance in the preceding picture and is not considered to be part of echo A or the LEWP.

### Origin and Evolution of the Gust Front Entering the Network

The severe gust front which entered the surface network at 2320 CST appears to have originated from echo A. This is suggested by a time sequence of positions of a "thin line" radar echo and the direction of the cold outflow current with respect to the precipitation echoes. During the period it traversed the network (see Fig. 7), the thin line was consistently found to be positioned at the leading edge of the gust front. (This relationship between a radar thin line and a surface cold front has previously been observed by Lidga and Bigler, 1958 and Fujita, 1966.) Assuming such a correspondence existed prior to the network entrance, the orientation of the thin line gives a clear impression that the gust front emerged from echo A (Fig. 5). This is in accord with the network streamline field in Fig. 9c, which suggests that the source of the cold outflow coincides with the center of echo A (Fig. 7).

Quite typically the forward edge of the cold outflow air mass of thunderstorms lies within several miles of the main rain area when the convective cells are in the initial part of the mature stage but as much as 20-30 mi ahead of the parent storms during the latter part of their mature or dissipating stage (Byers and Braham, 1949; and Colmer, 1971). Fig. 4 and Table 2 demonstrate that during the mature stage of echo A, i.e. 2300-2315 CST, damaging winds occurred within 5 nm of the forward echo boundary. On the other hand, during the time period the squall line approached and crossed the NSSL network, the forward gust-front boundary was increasing its lead over the forward echo boundary from 8.5 to 12.0 nm (Fig. 5).

Concluding Remarks

Although this analysis of the gust-front's history is based on relatively crude data the findings discussed above, when logically integrated, yield a rather complete description of the gust front prior to and during its passage over the network. The main source of the gust front was echo A. The gust front became well organized and quite severe as echo A attained high forward speed during the development of the LEWP. Later, as the parent A echo decelerated to some degree, the gust front pushed ahead of it. By the time the southern extremity of the LEWP had reached the northern part of the NSSL network the echoes were in the "late mature" stage and the gust front had moved to a position of about 10 nm downstream from the echo's forward boundary. This distance increases only slightly as the squall line passed over the network. It is important to point out (as will be seen in the last chapter) that while the gust front, pushing in the east-to-south quadrant from echo A, swept over the entire network, only the northern extremity of the network was traversed by the southern tip of the eastward bound echo. The major part of the network was traversed, partly by newly developed echoes along the southern tip of echo A and partly by echo C, both characterized by winds of less severity than those produced by the original A echo.

## CHAPTER V

### ANALYTICAL STRUCTURE OF THE THUNDERSTORM OUTFLOW

#### LEADING THE SQUALL LINE

The width of the gusty outflow leading the squall line precipitation echoes was only slightly less than the width of the network. Thus, the entire outflow air mass leading the echoes was within the network boundaries for a short time interval and complete analysis was possible only during this time. Since time-to-space transformations of data measurements were required for the analysis, the validity of the assumption of steadiness of the gust front and echo properties had to be investigated beforehand. In the preceding chapter the broad-scale temporal and spatial changes of the morphology and propagation of the gust front and precipitation echoes were examined during the period spanning the approach and passage over the network. Here we focus on the smaller scale characteristics of these aspects while the outflow was passing over the network. Following this brief survey, the analytical structure of outflow is discussed in detail.

#### Displacement Character of Squall System

Two distinct surface wind change lines were featured between the uniform, warm southerly flow and the cold, gusty northwesterly current of the squall-line outflow. The initial discontinuity was an abrupt wind direction change from uniform southerly to northwesterly. The line along



which this direction shift occurred is called the windshift line (Fig. 7). The 230 deg isogon in Fig. 9a is used to define this line since this isogon is located in the zone of maximum wind direction gradient. Note in Fig. 7 that a "pressure-jump line", i.e., a line marking the leading edge of a steep pressure rise, was practically coincident with the windshift line. Following the windshift and pressure-jump lines in Fig. 7 is a line marking an intense surge in the speed and gustiness of the wind; this wind-surge line is called the gust surge. The gust-surge line is represented by the  $12 \text{ m sec}^{-1}$  isotach in Fig. 9e because it lies within the region of maximum speed gradient. Note that the temperature "break" line (TB in Fig. 7), marking the leading edge of a sharp temperature fall, lies parallel to and several km behind the gust-surge line.

At  $2337\frac{1}{2}$  CST the windshift and gust surge were separated by a distance of 5 km at WKY but over the entire network the average distance was 8 km (Fig. 7). The radar thin line is seen to occupy the strip between the windshift and gust-surge lines.<sup>1</sup> The wind change lines near WKY lie about 19 km ahead of the forward boundaries of echoes A and A'.

Significant differential displacements among the echo boundary, gust surge, and windshift occurred during the period  $2313\frac{1}{2}$ - $2358\frac{1}{2}$  CST. Assuming the position of the gust surge is well approximated by the thin line during this period (as it was during the entire period that both were over the network, i.e., 2325-2350 CST), Figure 6 shows the gust surge to increase its lead over the echo boundary from 8.5 nm (15 km) to 12.0 nm (22 km) during the period  $2313\frac{1}{2}$ - $2358\frac{1}{2}$  CST. A sequence of isochrones of the thin-line positions (not shown) indicated the gust surge maintained a

---

<sup>1</sup>In the preceding chapter the thin line was used as an indicator of the position of the gust-surge line during the period prior to the gust front's entrance into the network. The slight difference in the positions of the thin line and gust surge introduces negligible error into the former consideration.

practically steady displacement speed of  $22 \text{ m sec}^{-1}$  during this period. At the same time the echo boundary propagated at a steady speed of  $19 \text{ m sec}^{-1}$ . The gust surge had a substantially greater displacement speed than the windshift while both were over the network. This can be seen from the sequence of isochrones of the windshift and gust surge positions in Fig. 8; in the vicinity of WKY the displacement of the gust surge had a speed of  $21 \text{ m sec}^{-1}$  compared to the windshift's  $15 \text{ m sec}^{-1}$ .

Thus, it is found that the echo boundary and the gust surge maintained a steady eastward translation in a 45-min period prior to and during passage over the network although the gust surge moved  $3 \text{ m sec}^{-1}$  faster than the echo. The windshift moved  $6 \text{ m sec}^{-1}$  slower than the gust surge; this speed difference was taken into account in the transformations from time to the space domain and accounts for the space scale discontinuity near 10 km in the vertical cross-sections. Based on the observed speeds of the echo boundary and gust surge the system velocity of the gust front which was employed in the scale conversions was chosen as  $20 \text{ m sec}^{-1}$ .

### Analytical Structure

#### Windshift

Byers and Braham (1949), Fujita (1966), and Colmer (1971) have reported that a wind direction change often precedes the severe gust front. This author has also observed this feature in many actual observations and from preliminary data analysis of several gust-front cases. In the case of 31 May 1969, the windshift was quite distinct as illustrated in Fig. 9a and c. The surface wind flow veered quite sharply from uniform southerly to northwesterly behind the windshift line (see also Fig. 10). The vertical cross section (Fig. 9b) reveals that the windshift sloped upstream with height at an angle of only 7 deg above the horizontal. Fig. 9e and f exhibit a distinct speed minimum coincident with the windshift at all levels.

Based on the author's experience the speed minimum seems to be a quite typical feature, corresponding to the commonly known "lull before the storm". The horizontal wind velocity divergence at the base of the windshift was about  $-15 \times 10^{-4} \text{ sec}^{-1}$  (Fig. 9c) in connection with a uniform upward motion field computed to be  $1 \text{ m sec}^{-1}$  at 400 m (Fig. 9d).

No change in the thermodynamic air properties occurred across the windshift. The ambient temperature and wet-bulb potential temperature patterns (Fig. 11a and b, respectively) are virtually isothermal across this wind discontinuity; thus, no change in air mass is indicated (also see Fig. 10).

The most striking change coinciding with the windshift was the sharp pressure rise measured at the surface (Fig. 10 and 12). The pressure rise was quite uniform along the line. The average pressure increment across the windshift was  $3\frac{1}{2} \text{ mb}$  and the horizontal gradient was  $0.6 \text{ mb km}^{-1}$ . This change satisfies the National Weather Service's definition of a pressure jump (PJ in Fig. 10 and 12). Immediately following the pressure rise a return to a constant level (PL) persisted until the arrival of the gust surge.

#### Gust Front

Generally, the analyses revealed the gust front as a high speed, gusty wind current of practically uniform direction led by an intense gust surge. Depicted qualitatively by the spacing of the streamlines in Fig. 9c, the intensity of the gust surge and speed of the upstream current was significantly greater in the region of stations WKY and 2C than at 5C and 6A. Focusing on the analysis at WKY, Fig. 9a and 9b show that only minor horizontal wind veering accompanied the gust surge (point b) and a secondary surge (point d). Wind direction changes in the vertical

direction were similarly weak. The isotach pattern in the vertical section (Fig. 9f) displays the gust surge as an intense wind-surge "wall" which is retarded near the ground. This frictionally induced surface retardation is evidenced by a forward gust-surge slope described by a rise of only 250 m within 2 km in the downstream direction. The horizontal speed gradient increased with height to a maximum value of  $10 \text{ m sec}^{-1} \text{ km}^{-1}$  at 335 m. At the crest of the gust surge a peak in the horizontal wind speed occurred as shown in the network isotach analysis (Fig. 9c). (Note that the speed maximum near stations 2C and WKY was about  $8 \text{ m sec}^{-1}$  greater than at stations 5C and 6A (see also Fig. 10)). The speed pattern in the vertical plane at WKY (Fig. 9f) shows that the speed maximum occurred at the gust-surge crest at all levels. Interestingly, the maximum speed core of  $33 \text{ m sec}^{-1}$  was located only 177 m above ground. In conjunction with the low-level speed maximum an extreme vertical shear value of  $160 \text{ m sec}^{-1} \text{ km}^{-1}$  occurred in the layer 0-to-50 m.

About 9 km upstream from the initial surge a secondary wind surge and speed maximum occurred within the gust front. It is located by point e in Fig. 9e and f. The network speed pattern indicates it had a small horizontal extent although its definition throughout the vertical section is rather clear; thus, it apparently was a relatively small-scale secondary surge within the larger scale gust front.

The large surface wind convergence within the gust surge reflected the large upward motion above. Typical divergence values are shown to be about  $-25 \times 10^{-4} \text{ sec}^{-1}$  (Fig. 9c). However, on a grid much finer than the 5 km grid employed in the computation of the surface velocity divergence, a maximum surface value of  $-5 \times 10^{-3} \text{ sec}^{-1}$  is obtained. Above 250 m the peak divergence was  $-1.2 \times 10^{-2} \text{ sec}^{-1}$ ; this value is in agreement with convergence values obtained above an intense surface cold front by Browning and Harrold (1970). The stream function pattern and the inserted wind

vectors (Fig. 9d) exhibit upward velocities as high as  $2.5 \text{ m sec}^{-1}$  within the gust-surge zone at the 400 m level. In the wake region of the maximum speed core a broader area of weaker downward motion featured typical values of  $0.8 \text{ m sec}^{-1}$  at the same level. Upstream from the gust-surge crest, the divergence pattern was no longer uniform in the y-direction reflecting the cellular pattern of the velocity field in the region of the secondary surge. In that region the assumption inherent in the stream function calculation, i.e.,  $\frac{\partial u}{\partial x} \gg \frac{\partial v}{\partial y}$ , in the x-z plane is not valid and the stream function pattern must be considered suspect. However, it seems safe to interpret the stream function pattern insofar as to state the flow pattern about the secondary surge has a qualitative resemblance to that of the initial surge.

The wind gustiness at the ground is found to be proportionate to the surface wind speed, but above 100 m a quite different pattern is revealed. The surface network analysis (Fig. 9g) illustrates that areas of maximum gustiness coincide with maximum speed areas (Fig. 9e). On the other hand, Fig. 9h shows that above the ground relatively low values of gustiness coincided with the maximum speed axis. Instead high gustiness occurred both beneath the forward sloping maximum speed core and, upstream, in the wake of the maximum speed core in a zone of relatively low wind speeds. A similar pattern appeared in connection with the secondary surge.

Several important aspects of the gust front's thermal structure are illustrated in the analysis shown in Fig. 11. (i) A narrow temperature ridge (point r Fig. 11c) appears at low levels just ahead of a steep fall. The magnitude of the temperature ridge is greater in the lower levels but it disappears at ground level. The vertical temperature gradient within this ridge in the layer 100-444 m was superadiabatic. (ii) Upstream of the thermal ridge peak a sharp temperature fall is featured (also see Fig. 10).

The horizontal temperature gradient at the ground was only  $1\text{C km}^{-1}$  but aloft it was  $4\text{C km}^{-1}$ . The large thermal gradient also appears in the surface wet-bulb potential temperature field (Fig. 11b). (iii) Just upstream of the temperature fall zone a minimum temperature axis appears but only above ground level (point c in Fig. 11). The minimum temperature core coincides with the maximum speed axis below 100 m but lags behind it by 1 km at higher levels. (iv) Upstream of the cold core is a broader zone of warmer air coinciding with the downward motion region appearing in the stream function field (Fig. 9d). This thermal ridge, exhibiting a magnitude of almost  $2\text{C}$  at the tower top, appears as only an isothermal region in the surface network analysis (point  $T_L$  in Fig. 10 and 11a). (v) And finally, in connection with the secondary surge (point t) a rather ill-defined thermal pattern is illustrated; however, the thermal structure near the 400 m level of the tower bears some resemblance to the thermal pattern of the initial cold surge.

Over the network the surface pressure surge connected with the gust surge was in proportion to the latter's intensity (Fig. 10 and 12). Between stations 5C and 6A the pressure rise following the gust surge was only about 20 milli-inches Hg (0.7 mb). At the same time the pressure rise in the region of 2C and WKY was quite steep and the total was in excess of 60 milli-inches Hg (2 mb). The pressure head ( $P_h$  in Fig. 10) was centered in the isothermal zone ( $T_L$  in Fig. 12) following the sharp temperature fall at the surface. Immediately upstream from the pressure head the pressure pattern became invariant at the elevated value and remained so up to the position of the heavy rain gushes (labeled R in Fig. 10).

The analytical features in all the vertical cross sections at WKY are combined in the schematic model shown in Fig. 13. The surface pressure trace at WKY is also shown.

## CHAPTER VI

### APPLICATION OF THEORIES AND MODELS TO THE ANALYSIS

#### Relationship of Windshift to Gust Front

Recall from the previous chapter that the leading edge of the cold outflow in the layer below 444 m was preceded by a sharp surface pressure jump coinciding with a windshift. In view of the objective of constructing a complete structural picture of the 31 May gust front it is necessary to determine if the windshift and pressure jump were an integral part of the gust front or if they were only somehow indirectly related to it. We initially proceed towards this determination by considering two hypothetical cases. Case X depicts a physical situation in which the cold air-mass current was mechanically pushing warm air horizontally ahead of it causing a low-level "back-current" (see Fujita, 1963, Fig. 28). The forward edge of the backcurrent would correspond to the windshift. In case Y the windshift is hypothesized to be the remnants of a former gust surge since diffused by turbulent mixing. The windshift would be considered part of the outflow air mass whereas in case X it is related but not considered an integral part of it. Now comparing the analytical characteristics against the imagined properties of the hypothetical cases to check for physical inconsistencies, case X is inconsistent with these analytical features: (i) the windshift and gust surge were not parallel, (ii) the latter propagated  $6 \text{ m sec}^{-1}$  faster than the former and (iii) most decisively, a large uniform pressure rise existed across the windshift. Case Y is in

disaccord with the (i) observed sharp pressure gradient coincident with the windshift and (ii) more importantly, with the observed lack of any evidence of a density change across the windshift line. These inconsistencies rule out the applicability of either of these two mechanisms to explain the initial pressure- and wind-change lines.

Other documented case studies of severe squall lines by Tepper (1950) and Fujita (1959) have revealed leading discontinuities which were partly or totally independent of changes directly related to the squall line. From his investigation of the squall line of 16 May 1948 over the Ohio Cloud Physics network, Tepper (1950) found that a surface pressure jump led all other surface weather changes. On the basis of the time sequence and nature of the surface parameter changes following the pressure jump, he concluded that "the pressure jump is independent of other parameters and that the behavior of the pressure profile can be explained only in part by the temperature break, wind shift, and/or rain gush." Fujita's (1958) mesoanalysis of the Severe Local Storms, Kansas-Oklahoma Network data of the 25 June 1953 squall line showed a pressure jump- and windshift line more than 50 mi ahead of a second pressure-surge line accompanied by vigorous thunderstorm activity. Fujita (1959) postulated the leading pressure-jump line was not directly coupled with the one which followed.

The nature of the leading windshift and pressure jump of the 31 May 1969 squall line is similar to that found by Tepper (1950) and Fujita (1959) in that the surface pressure and wind changes could not be attributed to changes occurring upstream. Recall from Fig. 11c that no significant density changes occurred across the windshift below 444 m. The density surge associated with the gust front at WKY was 10 km upwind of the windshift and the precipitation echo at all heights was much further upstream.



Analytical findings showing the surface pressure-jump and windshift lines to be practically coincident but lacking a density change across them, throughout the period of their translation over the network, leads to the suggestion that the windshift was a manifestation of horizontal accelerations of air parcels in response to the passing pressure gradient. The practically undisturbed thermal structure of air-layer below 444 m implies that the atmospheric phenomenon causing the pressure disturbance was substantially above the tower summit. The following section considers a possible mechanism of such a disturbance.

#### Gravitational Wave Model Applied to Windshift

Following his studies on the nature of pressure-jump lines through mesoscale and dynamic analysis Tepper (1950) proposed a mechanism of the pressure jump as an analogy to the hydraulic jump in liquids. According to his theory the initial stage of a pressure jump occurs when a sudden forward acceleration of a cold front acts as a piston to elevate the characteristic temperature inversion surface in the warm air ahead of the front. The elevated density interface then propagates horizontally ahead of the front as a gravitational wave. The propagating temperature inversion wave gradually develops a very steep slope on its forward side. Tepper drew analogy of this density-interface jump to the hydraulic jump which can propagate on the interface of stratified fluids of different densities. Because the sharp surface pressure rise in the atmospheric case is a reflection of the passage of the density interface jump aloft, he called it a pressure jump. He further postulated that the pressure jump serves as an effective mechanism for the development and maintenance of the pre-frontal squall line.

An investigation of the evolution of the 31 May 1969 squall line yielded substantial evidence of the applicability of such a mechanism. It

was found that (i) rawinsondes at Amarillo, Texas (AMA), Dodge City, Kansas (DDC), and TIK revealed thermal inversions near the 750-mb level exceeding the 5C potential temperature increment across them which Tepper specified to be sufficient for gravity-wave maintenance. (ii) As illustrated in Fig. 3 a sudden frontal acceleration occurred in Colorado and Kansas during the afternoon of 31 May 1-2 hr prior to thunderstorm development in the southern extremity of those states. (iii) Pressure jumps were reported ahead of the front from AMA to Tulsa, Oklahoma (TUL) and about 10 nm ahead of the heavy precipitation echoes of the squall line at Hobart (HBR), OKC and Ponca City (PNC) (note PJ's in Figs. 3 and 4b, 4c and 4f).

Five years later Tepper (1955) developed a simple pressure-jump model whereby the equations of motion and mass continuity for frictionless, incompressible flow were applied to a two-layer, hydrostatic atmospheric model. Each layer was homogeneous in density and the density of the lower layer was greater than the density of the upper layer. The lower layer was initially injected with a narrow, high-momentum air-current impulse oriented in a north-south direction. Graphical integration of the governing equations revealed that within 2 hr of the initial perturbation a density interface jump, accompanied with an eastward component of air motion, was propagating eastward from the axis of the initial current.<sup>1</sup> At the same time an interface depression was traveling westward from the identical origin. After a period of about 6-8 hr the eastward propagating gravity wave had undergone dramatic steepening of the slope of the interface and sharp intensification of the eastward flow speed across the jump zone (Figs. 9 and 11 of Tepper's 1955 article). In an atmospheric application, Tepper found that the steepened gravity wave appearing in his model could also

---

<sup>1</sup>Presumably, an initial perturbation caused by an abrupt frontal acceleration would also initiate such a traveling wave.

develop and propagate on naturally-occurring atmospheric thermal inversions; the surface manifestation of such an inversion surface jump is a pressure jump and a related windshift.

Tepper's (1955) model was applied to the ambient atmosphere over the network on the evening of 31 May. First consider the thermal and density profiles shown in Figs. 14a and 15, representing conditions just prior to the squall line onset. These profiles were obtained from the 1800 CST 31 May 1969 TIK sounding, modified in the lowest 444 m by substituting the surface pressure and tower temperatures at WKY at 2300 CST. The slight temperature inversion at 2300 m (Fig. 15, inset) had a density ratio,  $\frac{\rho_2 - \rho_1}{\rho_1}$ , ( $= \frac{\Delta\rho}{\rho_1}$ ) of  $1.14 \times 10^{-2}$ , where  $\rho_1$  and  $\rho_2$  are the respective air-parcel densities above and below the inversion layer extrapolated linearly to 2300 m as shown in Fig. 15. In this sense  $\rho_1$  and  $\rho_2$  represent the densities of air parcels specified by the ambient pressure and hypothetical temperatures  $T_1$  and  $T_2$  at 2300 m.

Following Tepper's model the phase speed,  $c_0$ , of a gravitational-wave jump in the initial stage of development propagating on the density interface of height,  $h$ , separating the two layers is given by

$$c_0 = \sqrt{\frac{\Delta\rho}{\rho_1} gh} \quad (5)$$

where  $g$  is the gravitational constant. Assuming that the density interface in the atmosphere over the network on 31 May could be taken as the 2.3 km thermal inversion and inserting its associated numerical parameters into (5) yields a  $c_0$  value of  $17.7 \text{ m sec}^{-1}$ . Tepper's numerical results (Fig. 8, in his article) specify that by the time the wave is fully developed the phase speed of its crest is  $1.15 c_0$  or  $20.2 \text{ m sec}^{-1}$ .<sup>1</sup> These values correspond

---

<sup>1</sup>This result assumes an atmospheric Froude number  $F_0$  of the initial perturbation equal to 1.

closely to the network-average propagational speed of the windshift and pressure jump, observed as  $15.5 \text{ m sec}^{-1}$ . The shape of the thermal inversion profile within the gravitational wave jump, as obtained by application of Tepper's numerical results to the 31 May atmosphere, is sketched in Fig. 14b. The inversion is seen to be elevated about 1 km at the crest of the wave. As the jump propagates along the interface, ambient air parcels are displaced upward, undergoing adiabatic cooling as they ascend, and resulting in a new temperature profile as shown by the dashed line in Fig. 14a. The temperature profile was obtained by lifting air parcels on a thermodynamic chart 1 km at the density interface while parcels above and below were raised an amount in accord with a linear reduction of lifting from 1 km at the interface to zero 1.5 km away. The plot of the computed hydrostatic pressure increase due to the cooling is shown in Fig. 14d. Comparison of the network-averaged pressure profile in the jump zone to the computed pressure profile below the interface jump shows almost identical magnitudes of the total pressure change; however, the observed pressure gradient is almost twice as large as the theoretical value. Similar correspondence is seen in the observed and theoretical wind regimes (Fig. 14e and f, respectively). The wind pattern within the theoretical jump was obtained directly from Fig. 8 of Tepper's (1955) article while the observed windshift pattern represents the result obtained by averaging the measured wind speed components in the vertical plane normal to the windshift. Just as in the case of the pressure, the magnitudes of the observed and theoretical wind change across the jump are remarkably similar but the former has a larger gradient than the latter.

Summarizing, evidence has been shown to demonstrate that atmospheric conditions, satisfying Tepper's theory of gravity wave formation and propagation on a thermal inversion in connection with squall line development, prevailed on 31 May 1969. Regular weather station reports of

a pressure jump ahead of a cold front and leading a squall line suggest that a gravitational-wave jump was associated with these features. The application of numerical results from Tepper's dynamic pressure jump model to the ambient atmosphere over the network yielded a gravity-wave jump whose associated phase speed, surface pressure pattern, and windshift were quite similar to corresponding changes accompanying the observed pressure jump and windshift. The profile of this theoretical inversion surface jump in the x-z plane is revealed in a composite schematic of analytical features of the forward portion of the squall line shown in Fig. 21.

The above deductions give substantial evidence to the validity of the gravity wave hypothesis to explain the observed pressure jump and windshift ahead of the gust front but a conclusive statement in this regard cannot be made because verifying observations and/or measurements were not made.<sup>1</sup> Even if such a theory could be adequately verified the question regarding the coupling to the gust front would still remain to be answered. On the other hand, an adequate basis has been established to conclude that the pressure and wind changes ahead of the gust surge were not inherent structural features of the outflow air mass of the precipitation echoes. This is actually the only conclusion relevant to the examination of the gust front structure which will be considered next.

#### Gravity Current Model Applied to Gust Front

A gravity current (often called density current) is a stream of high density fluid flowing along the horizontal bottom and displacing an

---

<sup>1</sup>Colmer (1971) and this author as well have observed that a windshift, often accompanied by a sharp pressure surge, is a frequent feature preceding the initial surge of the cold outflow of thunderstorms. This problem remains and deserves further examination.

ambient fluid of smaller density. The motive force is a horizontal pressure gradient across the lateral interface separating the two fluids which arises because of the relatively larger hydrostatic pressure within the heavy fluid (Benjamin, 1968). In the steady phase of gravity flows, there exists a dynamic balance between shear stresses and the pressure gradient force. Among common examples of gravity currents in nature is that which occurs when a body of saline water intrudes into a fresh water estuary or when a mass of muddy water displaces clear water along the bottom of a reservoir ("turbidity" current), a phenomenon often noted even by the casual observer. An excellent photograph of a gravity current simulated in a laboratory is seen in Fig. 16a (taken from Simpson, 1969). The white fluid mass is a saline water solution of specific gravity of 1.01 which is surging to the left along the bottom of a long trough filled with pure water. Gravity currents in the atmosphere are less obvious because of the complexities of atmospheric flows introduced by horizontal and vertical inhomogeneities of air density, compressibility effects, flow over irregular terrain, and the effects of earth rotation. Then, there is the added problem that atmospheric gravity currents are usually invisible since they are normally devoid of condensation. However, in some cases dust is picked up by strong surface winds and carried to great heights, i.e., 1 to 2 km, near the front of such cold surges making the "nose" of the currents clearly visible. Two examples are illustrated in the photographs appearing in Fig. 17. Fig. 17a is a large scale cold front in Kansas and Fig. 17b is a "downdraft haboob," the name given to the cold outflow of thunderstorms carrying high wind gusts and suspended sand in Sudan. Berson (1958), Clarke (1961) and Simpson (1969) have shown that such atmospheric flows have similarities to gravity currents, as defined at the beginning of this section and as

revealed in laboratory experiments. Sea-breeze flows having a duration of less than a day have also been shown to display some common structural and displacement characteristics with gravity currents by Clarke (1961) and Simpson (1969).<sup>1</sup> The object of this portion of this study is to examine the gust front for structural and displacement features which characterize gravity currents.

The nature of gravity currents has been investigated theoretically as well as in laboratory and numerical simulation experiments. Von Kármán (1940) introduced a simple theoretical model of a "perfect-fluid" gravity current propagating steadily along the horizontal bottom of an infinitely deep tank of relatively less dense fluid. This allowed him to assume that the environment fluid is undisturbed relative to the propagating heavy fluid and that the latter flow is energy conserving. Utilizing a coordinate system translating along with the gravity current of speed,  $V$ , he applied Bernoulli's equation for steady, incompressible, irrotational flow to points A and B along the streamline on the interface separating the gravity current and the ambient fluid (see Fig. 18). This equation applied to the upper fluid of density,  $\rho_1$ , (assuming A is a point of stagnation) gives

$$P_A = P_B + g\rho_1 d + \frac{1}{2}\rho_1 V^2$$

The same equation applied to the heavy fluid of density,  $\rho_2$ , and mean depth,  $d$ , (realizing that the gravity current is stationary relative to

---

<sup>1</sup>Air-mass currents having a lifetime of a day or more tend towards geostrophic balance. In this regard the relatively long lifetime of typical large scale cold fronts, i.e., sometimes many days, would tend to rule out the applicability of gravity-current motion. However, the large horizontal and vertical wind shears, generally found at the leading edge of large scale cold fronts, result in shear stresses which exert a much greater control over the motion than that due to the coriolis effect; thus, gravity-current motion occurs at the leading edge of cold fronts (Clarke, 1961). This aspect is further considered in a later section.

the assumed coordinate system) gives

$$P_A = P_B + g\rho_2 d$$

where  $P$  is the ambient pressure and  $g$  is the gravitational constant.

Combining the above two equations yields

$$v = \sqrt{2gd \left( \frac{\rho_2 - \rho_1}{\rho_1} \right)} \quad (6)$$

Gravity currents have previously been simulated in laboratory tank experiments by Keulegan (1958), Middleton (1966) and Simpson (1969) (a photograph of such a simulation, discussed earlier, is shown in Fig. 16a) as well as in a numerical experiment conducted by Daley and Pracht (1968). The experiments have demonstrated that greatest changes in the structure and displacement occur in the early stages of the flow, i.e., immediately following the removal of the lateral partition confining the high density fluid. Following the transient stage the current quickly assumes a quasi-steady geometric shape and density structure. This is confirmed by the near-steady displacement over the extent of the trek along the trough. In this steady stage the displacement obeys the relation

$$v = k \sqrt{gd \left( \frac{\rho_2 - \rho_1}{\rho_1} \right)} \quad (7)$$

where the symbols are the same as before. From the numerous experiments conducted by Keulegan (1958), employing an assortment of trough geometries, and for fluid density ratios typical for alleged atmospheric gravity currents, i.e.,  $0.01 \leq \frac{\rho_2 - \rho_1}{\rho_1} \leq 0.02$ ,  $k$  was found to have an average value of 1.1. The corresponding theoretical value of  $k$  implied by (6), as deduced from a frictionless flow model, is 1.414. Benjamin (1968) obtained



a theoretical value of 1.23 for a model gravity current in a reservoir of finite depth where dissipative energy losses at the current front are taken into account (see Lamb, 1932, p. 280). This summary of documented results demonstrates reasonable consistency in findings from independent investigations and thus gives assurance of the validity of (6) and (7) to describe gravity current motion.

(In view that the present examination of the gust front is for structural similarities to gravity currents, the boundary of the gust front must now be considered identical to the boundary of the constituent cold air. This consideration implies that the leading edge of the gust front is the zone of the sharp temperature drop. Thus, the previous definition of the leading edge, i.e., the gust-surge line, is discarded and the density-surge line in Fig. 13 (identical to the temperature-break line in Fig. 7) is assumed to be the forward air-mass boundary.)

The initial step which is taken in the examination of the 31 May gust front for behavior as a gravity current is to apply (6) and (7) to its analytical structure and compare the theoretical result with analytical findings. In the proper application of these equations  $V$  is the displacement speed of the gust front relative to the flow of the ambient troposphere or, vice versa, the ambient flow relative to a coordinate system attached to the gust front. In a paragraph to follow it is shown that the outflow air mass had a maximum height of about 1700 m above the ground. It seems reasonable to assume that the tropospheric flow above about 3400 m did not influence the propagation of the gust front. The mean wind vector in the surface-to-3400-m layer, revealed by the 1800 CST TIK rawinsonde, was directed almost parallel to the y-direction in Fig. 9c; the component in the x-direction was only  $+1 \text{ m sec}^{-1}$ . Since the propagation speed of the gust front near WKY was  $21 \text{ m sec}^{-1}$  in the

positive x-direction, the x-component of ambient-air flow,  $u$ , is directed towards the gust front with a speed of  $20 \text{ m sec}^{-1}$  as seen by a coordinate axis attached to the gust front. It can also be shown from Figs. 9b and 9f that in the warm air ahead of the gust front the layer-mean of the y-component of wind speed,  $v$ , varies less than  $4 \text{ m sec}^{-1}$  along the x-direction. Assuming that the latter result is general throughout the ambient-air layer below 3400 m, then the  $v$ -component can be ignored in the derivation of the displacement speed,  $V$ , (see p.33) without significant error since  $u^2 \gg v^2$ . Thus, in Fig. 18,  $V \approx u$  ( $= 20 \text{ m sec}^{-1}$ ) and the s-coordinate corresponds to the (-x)-coordinate in Fig. 9c.

The application of (6) and (7) further requires that the mean depth  $d$  of the gust front's associated cold air and the density ratio,  $\frac{\bar{\rho}_2 - \bar{\rho}_1}{\rho_1}$ , be determined (the bars over the density symbols denote mean values of the respective cold and ambient-air densities in the atmospheric layer accommodating the gust front.). The atmospheric measurements available for this analysis do not supply this information directly because they do not extend to the height of the cold-air dome. In fact, the vertical thermal cross section (Fig. 11c) implies that the gust front was far higher than the top level of the tower. According to Byers and Braham (1949) and Fujita (1963) the horizontal temperature difference between environment air and the cold outflow near its upper boundary is quite small. Fig. 11c shows that the temperature drop at 444 m is almost as large as that exhibited at lower levels. Furthermore, the surface pressure rise following the cold surge was far greater than that which could be attributed to a layer of cold air less than 500 m thick.

The depth of the cold air was realistically inferred by extrapolating the horizontal environment-to-gust-front temperature decrease to a height above the tower such that the computed hydrostatic pressure at the ground matches the observed value. Since the mean depth  $d$  is desired

the mean surface pressure rise and the temperature upstream from the density surge were employed. The mean pressure increment following the gust surge at WKY is shown as 2.2 mb in Fig. 13. Warm-to-cold air temperature decreases of 4C and 5C were obtained from Fig. 11c, the first value representing the average fall from undisturbed environment and the second corresponding to the fall from the narrow thermal ridge just ahead of the density surge (see Fig. 11c). In order to arrive at the gust-front temperature profile above the tower these temperature drop values were subtracted from the modified TIK sounding as illustrated in Fig. 15 and Table 3. The cold-air depth required to account for the total pressure rise, combining rises occurring during windshift and gust surge (shown as 6.2 mb in Fig. 13) was also computed according to the procedure described above (CASE II in Fig. 15 and Table 3). This depth value is to be utilized for a consideration discussed later.

Radiosonde ascents penetrating the cold outflow of thunderstorms conducted by Thunderstorm Project personnel usually revealed the upper thermal boundary below 1525 m (Byers and Braham, 1949). Farquahrson (1937) and Freeman (1952) cited by Simpson (1969) have reported depths of intense haboobs in Sudan of 1100-1500 m. The depth values in CASE I indicate the 31 May 1969 outflow air mass was relatively deep. On the other hand the depth values under CASE II exceed all previous cold-outflow depth estimates known to the author.

The density ratio,  $(\bar{\rho}_2 - \bar{\rho}_1)/\bar{\rho}_1$ , comprised of layer-means of the high density gust-front air and the lesser density ambient air displaced by the gust front, is obtained in a manner illustrated in Fig. 15. Since the density versus height curves in Fig. 15 are practically straight lines, the values of  $\bar{\rho}_2$  and  $\bar{\rho}_1$  are assigned the densities at the mid-levels of the respective air layers. The density ratios are tabulated in Table 3.

The substitution of these numerical values of the mean depths and density ratios into Eqs. (6) and (7) gives the displacement speed of the gust-front air mass propagating as a gravity current. For CASE I, gratifying agreement to the observed speed<sup>1</sup> is obtained from both equations especially for the 4C temperature drop (considered to be a more realistic value). The larger theoretical speed given by von Kármán's relation (second "displacement speed" column in Table 3) is expected, as energy dissipation processes which retard horizontal motion in the actual flows, are not taken into account. These computational results indicate that if the assumption about the upper temperature profile of the cold air is not grossly incorrect the overall agreement between theory and observation indicates that the governing dynamics of the 31 May gust front was fundamentally that of a gravity current.

The exceedingly large value of the gravity current displacement speed computed for CASE II is due to the inherent large value of cold-air depth. (Recall that this depth value was computed assuming that the successive pressure rises associated with the windshift and gust surge were due to the influx of high density air comprising the gust front.) This result adds support to the hypothesis (already employed previously) that the depth of cold air comprising the gust front is defined by the second pressure rise only, in agreement with the picture implied by the analytical fields (Figs. 9-12). This reasoning adds further support to the conclusion arrived at previously (see p. 31), that the forerunning windshift and pressure jump were not characteristic features of the gust front structure.

---

<sup>1</sup>The "observed speed" in Table 1 is the gust front displacement relative to the flow of the lower tropospheric environment.

### Comparison of Detailed Structure of Gravity Currents and Gust Front

In the previous section the gross density structure of the 31 May gust front was employed for examination of its horizontal propagation as a gravity current. Application of elementary gravity current theory demonstrated that its observed displacement did approximate that of a gravity current according to a model on which the theory is based. We have already alluded to an example of a laboratory gravity current (Fig. 16a) which exhibited a distinctive boundary surface shape. Such laboratory currents have further revealed a systematic internal circulation and mass entrainment pattern near the leading edge. In the following paragraphs the detailed analytical structure of the gust front is examined for analogous features.

#### Geometric Shape

Laboratory gravity currents display a typical surface boundary geometry as exhibited in the photograph shown in Fig. 16a. The surface profile of the gravity current in a vertical plane normal to the current front reveals a projecting nose a small distance above the lagging current front at the bottom. In upper regions the density interface slopes backward; crests, and then slopes downward to form an elevated head at the current front. In this photograph the head depth appears to be only slightly greater than the mean upstream value, however, Kuelegan's (1958) heads had about twice the depth of the upstream current for density ratios (as previously defined) similar to the gust front. The density interface upstream of the head, has been generally found to display a near-constant height.

The vertical profile of the density surge of the gust front below 444 m combined with the underlying surface pressure pattern imply a protruding nose some distance above the tower summit. The density-surge

line exhibited a forward slope near the ground as shown in Fig. 13; the average slope in the lowest 100 m is  $65^{\circ}$ .<sup>1</sup> This density-surge slope is maintained throughout the tower depth. But, assuming the surface pressure at WKY, directly below the density discontinuity, is hydrostatic, the cold-air boundary above the tower top must begin a rearward slope within several hundred meters to be consistent with the surface pressure change. Thus, a protruding nose is envisioned similar to those seen in the photographs in Fig. 17. Simpson (1969) observed similar nose shapes in sea-breeze fronts. Note that the deduced gust-front nose, as well as the noses in the other examples referenced above, have a general shape similar to those leading gravity-current surges in the laboratory (Fig. 16a). However, in other studies, Koschmieder (1936, 1941) found that the leading cold-air profile changes in time and space in individual sea-breeze fronts and Colmer (1971) observed that the leading horizontal wind-shear profile varied from one gust-front case to the other. This finding prompted them to suggest that the cold air comprising the projecting nose periodically collapses into the warm air beneath it (due to friction) in a cyclic manner. In this regard, the narrow thermal ridge ahead of the density-surge line (Fig. 11c) and beneath the just inferred nose, may be indicative of subsiding air motion in conjunction with the beginning stage of the nose collapse.<sup>2</sup> The stream function analysis does not reveal

---

<sup>1</sup>The forward slope of the gust surge was  $85^{\circ}$ , significantly greater than that exhibited by the density-surge line, in agreement with the findings of Goldman and Sloss (1969). The probable reason for the greater slope of the gust-surge profile is the unlimited frictional retardation of the wind near the ground. On the other hand the slope of the thermal profile is limited by overturning which commences when the overlying cold air projects too far over the warm air.

<sup>2</sup>Observations of the wind and thermal structure at the leading edge of gust fronts, suggestive of all stages of this cyclic process, have been noted in preliminary investigation of other gust-front cases by the author.

downward flow below the nose, i.e., in the area of Fig. 9d bounded by the time interval 2338-2339 CST and the layer 0-300 m. However, this apparent contradiction can be subjectively countered by considering that such a small scale feature as a collapsing nose would probably not be defined by such an analysis. Therefore, downward air motion below the projecting nose is inserted in Fig. 21, consistent with the thermal ridge in Fig. 11c.

The surface pressure distribution and thermal structure of the overlying gust front, just upstream of the protruding nose, was utilized to infer an elevated crest of cold air. The pressure traces at WKY and 2C exhibit a pressure peak just upstream of the maximum wind cell (Figs. 10 and 13). This excess pressure maximum at WKY, assumed to be hydrostatic, is shown as 2.5 mb in Fig. 13. In the region of the pressure maximum, the average surface-to-444 m temperature difference from the displaced warm air is only  $3.5^{\circ}\text{C}$ . Employing these parameter values to compute the depth of the cold air, according to the procedure described previously, yields 1700 m. This depth exceeds the uniform upstream level of 1220 m (CASE I, Table 3) by 480 m. Henceforth, this vertical bulge in cold-air height will be called "elevated head," in conformity with the term applied to an analogous feature in laboratory gravity currents. The horizontal distance between the elevated head and the density-surge nose is 4 km; the uniform depth upstream begins 7.5 km from the nose (Fig. 21). The mean dimensions of heads appearing in Keulegan (1958) laboratory gravity currents, "blown-up" to the scale of the gust front, are: head of height 2500 m, positioned 5 km upstream from the nose while the upstream constant depth region begins at 7.5 km from the nose. This comparison shows that the vertical dimension of the gust-front head is much suppressed compared to heads exhibited by gravity currents in stratified liquids in Keulegan experiments, although the horizontal dimension is similar.

A scan of meteorological literature for previous discoveries of elevated heads at the front of cold surges yielded several examples. From plots of the height of the vertical wind shear maximum (assumed to coincide with the frontal surface) with horizontal distance from the leading edge of four cold fronts in Australia, Berson (1958) found that most cases revealed a shallow "dip" in otherwise upsloping shear profiles. An example, reproduced from his article, is seen in Fig. 19. Berson called the small maximum in the shear profile between the leading edge and the dip a "friction head" as an analogy to heads in laboratory gravity currents. The horizontal distance of the dip from the surface position of the shear zone was in the range 13-59 km, as the actual location varied from front-to-front as well as in time and space in individual fronts. Clarke's (1961) vertical section analyses through cold fronts and sea-breeze fronts in Australia in many cases exhibited vertical bulges in the temperature and streamline fields near the leading edge, suggestive of frontal heads on a scale similar to those found by Berson (1958). In view that vertical and horizontal dimensions of laboratory gravity-current heads are not far different, Clarke would not submit that these bulges were the counterpart of heads seen in the laboratory. Instead, he reserved the possibility that heads of much smaller horizontal dimension may have existed in the fronts he examined but could not be identified because of insufficient density of pibal and rawinsonde measurements. With the aid of doppler wind measurements and rawinsondes, Browning and Harrold (1970) deduced a small frontal surface "nose" (identical to the head as defined in this paper) at the crest of an abrupt rise of the leading cold-air boundary to 1 km followed by a temporary upstream fall. The horizontal dimension was about 10 km. However, an attempt to interpret this head as an analogy to gravity-current heads requires that



great caution be exercised.<sup>1</sup> In conclusion, in view that the typical gust front is of a smaller scale than cold fronts and since it usually exhibits a more intense initial surge, it is not surprising that the 31 May gust-front head had a larger vertical dimension and smaller horizontal dimension than those previously observed in cold fronts and sea-breeze fronts.

The shape of the top of the cold-air surface of the gust front, upstream of the elevated head, was also inferred from the surface pressure pattern in conjunction with the observed and inferred thermal distribution in overlying cold air. Figs. 10 and 13 show that the pressure at WKY and 2C was practically invariant upstream from the head region up to the position of the heavy rain area denoted by R in Fig. 10.<sup>2</sup> The thermal distribution is shown in Fig. 11a and 11c to be slowly decreasing in the coincident region upwind of the head. Assuming the surface pressure over this horizontal distance is hydrostatic and barring compensating mass transfers above the gust front, these pressure and thermal fields imply that the depth of cold air was relatively uniform or perhaps decreasing upstream of the elevated head. For simplicity the cold-air depth in this

---

<sup>1</sup>The scale of Browning and Harrold's (1970) analysis (as well as of the squall-line analyses performed by Newton, 1950) implies that the identification of a feature the scale of the head would be quite difficult and, furthermore, an attempt to interpret such a feature is frustrated by likely complications introduced by the overhead intense convection currents associated with the heavy precipitation. On the other hand a gust front, which is the low-level cold outflow from the convective precipitation, is a smaller scale atmospheric current, requiring a relatively small scale analysis to identify a feature the size of the head such as that found in the case of the 31 May gust front. Since the head deduced in the latter analysis was 15-20 km downstream from the heavy precipitation its interpretation is less difficult.

<sup>2</sup>The surface pressure is known to rise sharply in the region where heavy rain is accompanied by intense cold downdrafts as shown by Fujita (1963).

region is assumed to have a constant value and equal to 1350 m which is a rough average of CASE I in Table 3 (see Fig. 21). Recall that the laboratory gravity currents also feature a uniform depth in the analogous span of the current.

The observation of uniform depth of cold air in the sector of cold surges where frictional stress and horizontal pressure forces are in approximate balance has some documented precedence. From a theoretical analysis, Ball (1960) has shown that when frictional stress is taken into account in the equations of motion the solutions reveal that the slopes of frontal surfaces are grossly different than the frontal slope given by the Margules relation for geostrophic flow. In the former case the frontal inversions tend to become horizontal with increasing distance from the cold front. Clarke (1961) showed that approximate frictional balance extends up to about 30 km upstream of the leading edge of cold fronts and sea-breeze fronts in Australia. At farther upstream distances geostrophic balance predominates. These findings by Ball (1960) and Clarke (1961) seem to be consistent with the shallow dips appearing in Berson's (1958) and Browning and Harrold's (1970) frontal analysis.

In view of Ball's and Clarke's results it is likely that the air motion within the 31 May gust front was almost entirely governed by frictional stress and horizontal hydrostatic pressure gradient. Recall that the gust front thermal inversion was deduced to be horizontal or even downward-sloping with increasing distance from the leading edge. Furthermore, the observation of steady horizontal displacement (see p.17) suggests that air motion inside the gust front maintained a balance between the frictional and the pressure gradient force. It is not surprising that such large frictional stresses, as are necessary to balance the observed horizontal pressure gradient, apparently occurred inside the gust front considering the extreme horizontal and vertical wind shears which existed

at the boundaries of the air mass (see bottom of p. 22).

Thus, it has been demonstrated that the observed and deduced shape of the 31 May gust front's bounding surfaces exhibit a clear resemblance to the shape of experimental gravity currents. In addition, some gross deductions based on the results of Ball's (1960) and Clarke's (1961) studies indicated the steady, horizontal air current comprising the gust front was governed by a balance of forces, identical to those acting in gravity flows. However, we have yet to consider the analytical three-dimensional circulation and gustiness patterns inside the gust front on the one hand and identical features observed in gravity currents on the other.

#### Internal Circulation and Gustiness

Laboratory studies of gravity currents have revealed the environment flow relative to the forward motion of the head and the internal circulation fields in vertical planes normal to the leading edge of such flows. Middleton's (1966) observations of the flow field relative to the motion of the elevated head resembles a flow pattern characteristic of flow around a solid body of identical dimensions. This picture implies that when the head is translating horizontally at a rapid rate upward motion of ambient fluid above the nose would be substantial. The internal flow of laboratory gravity currents features a strong forward horizontal current a small height above the bottom called an undercurrent. The speed of the undercurrent is greater than the forward speed of the head. Consequently, the flow is deflected upwards through the nose and then rearward near the crest of the head (Fig. 20).

The analysis of the flow pattern in vertical planes features a strong ambient air flow towards the head of the gust front and large upward ambient-air motion near the nose indicative of upsliding flow over the head. This flow pattern is constructed by first considering that

relative to a coordinate axis attached to the head, the environment flow in the lower 500 m is directed towards the head at approximately  $20 \text{ m sec}^{-1}$ . Now, the stream function field (Fig. 9d) discloses an upward velocity ahead of the nose as high as  $2.5 \text{ m sec}^{-1}$  at the 400 m level. Substantially greater values are likely above the tower summit as the extreme velocity convergence of  $10^{-2} \text{ sec}^{-1}$  is maintained from just above the ground to the top level. A rough upper-bound estimate of the average vertical velocity of air parcels, being mechanically lifted by the head from the ground to 1700 m, is  $4 \text{ m sec}^{-1}$ . This estimate is in accord with doppler radar vertical velocity measurements over an intense cold front accompanied by convective precipitation reported by Browning and Harrold (1970).

The stream function analysis of the wind current normal to the density-surge line can be shown to disclose that cold air actually flowed across the density-surge zone. This is seen from Fig. 9d by an initial consideration that there is no relative flow across the superposed  $20 \text{ m sec}^{-1}$  isotach with respect to the coordinate system adopted. However, immediately to the left of this isotach the streamline flow is forward and thus across the superposed density-surge line. This result is not without uncertainty, however, because the distance separating the  $20 \text{ m sec}^{-1}$  isotach and the density-surge line is small and the accuracy of stream function field is questionable on such a small scale, particularly near the discontinuity zones.

The ambient air flow towards and over the cold outflow head and the cross-density-surge flow of the cold air is illustrated in Fig. 21. Although the streamlines are drawn schematically their spacing qualitatively depicts the flow speed. The streamline flow at heights above the nose was drawn subjectively but with qualitative adherence to the conservation of mass and also according to the assumption of no flow across the cold-air boundary. The ambient-air streamline pattern near the head is

quite similar to that observed in laboratory experiments (Middleton, 1966 and Simpson 1969). It is also consistent with atmospheric observations of dust being lifted to great heights at the leading edge of intense cold surges as exemplified in Fig. 17. The cross-density-surge flow is in accord with analyses of cold fronts and sea-breeze fronts by Berson (1958) and Clarke (1961). (An example, taken from Berson's article, is shown in Fig. 19.) Furthermore, it allows for dust to be picked up within the cold air (where winds are likely to be strongest as in this case) and then transported horizontally to the region of maximum vertical velocity just ahead of the projecting cold-air nose; in this position the dust could be transported upwards to the crest of the head as shown in Fig. 17.

The average speed of the cold-air current, upstream of the elevated head, was similar to the horizontal displacement speed of the gust-front head. This mean current speed, representing the average of horizontal velocity components in the vertical plane upstream of the initial surge in Fig. 9d, was  $21.5 \text{ m sec}^{-1}$ . The displacement speed of the head was  $21.0 \text{ m sec}^{-1}$ . Applying Prandtl's (1952) expression for the horizontal propagation of an ideal cold front to the gust front, yields about  $\frac{1}{2}$  the speed of the mean upstream current and, thus, seriously underestimates the actual propagation speed of the gust front. Clarke (1961) obtained a similar result in his application of Prandtl's relation to sea-breeze flows and cold fronts in Australia.

A distinct vertical circulation field in a vertical plane normal to the leading edge of the gust front is deduced from the surface-to-444 m vertical section analyses (Fig. 9d and 9f). In the region of the head a strong forward current of relative speed  $13 \text{ m sec}^{-1}$  is centered only 180 m above the ground (Fig. 9f). This jet-like current is henceforth termed undercurrent as an analogy to a similar feature appearing in laboratory gravity currents. (It is interesting to add that Simpson's (1969) laboratory

currents revealed a value of 1.3 for the ratio of the undercurrent speed to the propagation speed of the head. The analogous ratio for the gust front was 1.6.) The undercurrent was diverted upward in the region of the gust-front nose. Downward air flow occurred in the wake region of the head, in broad agreement with a similar feature appearing in the analysis of cold fronts and sea-breeze fronts by Berson (1958), Clarke (1961) and Browning and Harrold (1970). Fig. 9d reveals downward motion at 400 m approaching  $1 \text{ m sec}^{-1}$  in a region corresponding to the backside of the head, while upstream, the average downward component was only of the order of  $10 \text{ cm sec}^{-1}$ . Note that the zone of maximum downward speed in Fig. 9d coincides with a positive temperature anomaly of  $2\text{C}$  in Fig. 11c, implying subsidence of potentially warm air. Downward air parcel displacements of almost 200 m are indicated. These analytical features can be interpreted to mean that the cold-air flux that supplied the high-speed undercurrent came partly from air which had subsided some height on the back of the head and partly from the gradually subsiding forward current originating far upstream of the head. As regards the downward flow on the back and upward flow on the front side of the head (discussed earlier) mass continuity requires rearward air flow near the head crest. The actual flow pattern below 444 m and that envisioned above is illustrated in Fig. 21. The weak secondary surge beginning at 2345 CST is not considered to be an important feature of the gust front as concluded earlier.

The streamline flow pattern shown in Fig. 21 bears some resemblance to that obtained near the leading edge of a cold front by Berson (1958) (see Fig. 19). There is a more striking correspondence to Prandtl's (1952) flow model of a cold front as seen on pp. 369-370 of his textbook.

Coupled with the internal flow pattern the wind gustiness and thermal fields are utilized to infer a complex ambient-air entrainment mechanism. First of all, the broad gustiness maximum in Fig. 9h superimposed on Fig. 9f coincides with the wake region of the initial maximum wind speed cell. Recall from p. 8, the gustiness included airstream eddies of horizontal wavelength up to 3 km. Tower temperature records in the segment describing the broad thermal maximum and also coincident with the gustiness maximum revealed temperature oscillations of horizontal wavelengths similar to the wavelengths of gusts comprising the gustiness. The peak amplitude of these temperature oscillations was 0.4C, implying vertical air parcel displacements in the eddies of almost 40 m. Since such large eddies were concentrated in the wake region of the head where the vertical flow is towards the ground, it is reasonable to infer that turbulent mixing of cold and ambient air occurred along a diffuse interface on the back side of the head crest; thence the eddies were continuously carried downward to heights below 444 m by the general flow. A second gustiness maximum in Fig. 9h, smaller in area but greater in intensity than the one discussed above, was located beneath the projecting nose.<sup>1</sup> Recall that this region is characterized by extreme vertical wind shear and slightly superadiabatic temperature lapse rate. Thus, the large eddies in the shearing current are not suppressed in this air column. Furthermore, the implication of cold-and warm-air mixing is consistent with the analytical feature depicting cross-density-surge flow in this portion of the gust front.

The mixing zones and related regions of large eddies are schematically illustrated in Fig. 21, the latter by short, curled arrows. The

---

<sup>1</sup>This gustiness maximum would be a great hazard to aircraft in landing and take-off patterns at airports.

entrainment of ambient air into the head implies the gradual dilution of the cold air, however, this tendency is apparently counteracted by the continuous influx of cold air as shown in Fig. 21 by the inflowing streamlines originating far upstream.

Laboratory gravity currents reveal an ambient fluid entrainment mechanism similar to that deduced for the gust front. Keulegan (1958) and Middleton (1966) observed that the fluid volume in the wake region of the head is a mixture of environment and high density fluid. This eddy infested mixture gradually descends and is slowly entrained into the undercurrent. This turbulent region is shown in Fig. 16a.<sup>1</sup> Simpson (1969) examined the fine details of the mixing process in laboratory flows and observed that the upper boundary of the head consists of bulges which roll up as they are swept backward, resembling Kelvin-Helmholtz instability billows along a density interface with shear. Fig. 16b illustrates that large entrainment of ambient fluid occurs as the billows break up. Simpson (1969) suggested that a similar process occurs in sea-breeze fronts, following his examination of flight records of glider plane penetrations. The analyses of atmospheric cold surges by Berson (1958), Clarke (1961), and Browning and Harrold (1970), all show evidence of air entrainment upstream of the frontal head. A haboob photograph appearing in Farquharson (1937) reveals that in the upper region of the head the dust cloud texture resembles that shown in photographs of laboratory gravity currents appearing in Fig. 27 of Keulegan (1958). All of these examples of actual observations of turbulent entrainment are broadly consistent with the deduced entrainment mechanism of the gust front illustrated in Fig. 21.

---

<sup>1</sup>There is no evidence of mixing beneath the nose of laboratory gravity currents. This is due presumably to the fact that the nose projection over the less dense ambient fluid is quite small; in many experiments the nose overlap was not detected. In the atmosphere the analogous overlap can be large because of the large frictional retardation of the flow near the ground.



## Dynamic Similarity of Gust Front and Gravity Currents

Use has already been made of the equation

$$V = k \sqrt{gd \frac{\Delta\rho}{\rho_1}} \quad (8)$$

which relates the displacement speed,  $V$ , to the depth,  $d$ , of a gravity current of fluid density,  $\rho_2$ , and the density ratio,  $\frac{\Delta\rho}{\rho_1}$  ( $= \frac{\rho_2 - \rho_1}{\rho_1}$ ), where  $\rho_1$  is the ambient fluid density. As discussed previously, when (8) is applied to atmospheric gravity-current phenomena, layer-mean densities should be used. In (8)  $k$  is a non-dimensional number that can be interpreted as a ratio of the inertia of the current to the buoyancy force. This ratio defines the internal Froude number. From laboratory studies Keulegan (1958) found that when  $d$  is the mean depth of the gravity current  $k$  has a constant value of 1.1 for Reynold numbers greater than 1000. Recall that von Kármán's (1940) theoretical value was 1.414. When the depth of the elevated head from Keulegan's currents was substituted for  $d$  the mean value of  $k$  was found to be 0.76. Similar Froude numbers were obtained by Middleton (1966) in another laboratory study and by Daley and Pracht (1968) in a numerical simulation. While (8) has been applied previously to the mean gust-front structure (see p. 37), the object here is to establish the Froude number of the gust front and to compare it with experimental values. Dynamic similarity is then discussed taking into account physical similarities and differences in the source mechanism of both the gust front and gravity currents produced in the laboratory.

The internal Froude number computed for the gust front is found to be slightly larger than those determined from laboratory gravity currents and, in turn, even larger when compared to large scale atmospheric cold surges. For the case of the mean cold-air depth of 1350 m and density

ratio as shown in Table 3,  $k$  is equal to 1.25. When the head depth is employed in (8)  $k$  is 1.08. These two  $k$  values average about 25% greater than those obtained in Keulegan's experiments. In other documented examples of cold surges, four cold fronts examined by Berson (1958) and four by Clarke (1961) revealed almost identical Froude number averages, i.e., 0.55 and 0.59, respectively, about 25% less than experimental gravity currents. Froude numbers obtained from Clarke's (1961) and Simpson's (1969) sea-breeze analysis are somewhat conflicting but still average 12 per cent less than experimental values. On the other hand in the case of two haboobs exhibiting a mean propagation speed of  $12.5 \text{ m sec}^{-1}$  and mean depth 1300 m, Simpson (1969) reported a  $k$  value of 0.79. Since the 31 May gust front had about the same depth but moved almost twice as fast as these haboobs there is some suggestion that the  $k$  value of thunderstorm cold-air outflows is in proportion to the speed of the accompanying wind.

The larger Froude number obtained for the 31 May gust front is not unexpected in view of the apparent difference in the mechanism of its evolution and maintenance compared to laboratory gravity currents and other atmospheric examples exhibiting gravity current similarities. Recall from Chapter III that the gust front became severe as the parent echo attained high intensity and a large forward speed during the evolution of the mature stage of the LEWP. These observations suggest that the gust front initially evolved as high horizontal-momentum air inside the cumulonimbus cloud was transported to the ground in massive cold-air downdrafts. Then this mass of cold air at the base of the downdraft, already endowed with large horizontal momentum, spreads outwards as a gravity current. By this means the gust front could maintain greater

horizontal momentum than that derived from a balance of the frictional drag and the hydrostatic horizontal pressure gradient. The excess horizontal momentum of the outflow would in turn serve to make the Froude number larger. For the case of an ideal laboratory gravity-current experiment a constant pressure head is maintained at the source in order to provide the high density fluid with sufficient initial forward momentum to continuously supply the advancing current. In such a case the current momentum at the source does not effect the displacement speed of the advancing head. Considering this aspect, the source mechanism of laboratory gravity currents seems to be more similar to that of cold fronts and sea-breeze fronts than to the analogous mechanism of the gust front.

It is difficult to estimate the effect of vertical momentum transfer in the thunderstorm downdraft on the momentum of the cold outflow of thunderstorms. Adding to the uncertainty is the unknown relationship between the horizontal speed of a radar echo and the horizontal air speed inside the downdraft. It is comparatively clear that the horizontal momentum of the downdraft could be a significant factor only in the case that it is substantially greater than the horizontal momentum of the outflow due only to the influence of gravity.<sup>1</sup> This situation is likely in the formative stage of the gust front when the cold outflow is relatively shallow;<sup>2</sup> in such a case the gust front lies in the immediate vicinity of the downdraft and the streamline flow depicts a pattern envisioned when a jet of fluid strikes a plane surface at a small angle. In such a case

---

<sup>1</sup>Actually, one can reason that the horizontal momentum of air at the base of the downdraft, greater than the momentum of the gust-front head, is required for the maintenance of the latter because the outflow stream is expected to lose momentum continuously due to friction in the region of near-zero pressure gradient between the head and the downdraft.

<sup>2</sup>Recall from Eq. 7 that the speed of a gravity current is directly proportional to the square root of its depth.

the flow speed decreases sharply with normal distance from the jet core. Such a flow picture was revealed in another gust-front analysis performed by the author (to be reported at a later date).<sup>2</sup> However, once the amassed cold becomes sufficiently deep and/or the horizontal momentum of the downdraft becomes sufficiently small, the cold outflow air evidently propagates approximately as a gravity current under relatively little influence of the downdraft momentum.

At the time of analysis of the 31 May gust front the parent echo had already diminished somewhat in intensity and the density surge had moved outward to a position 20 km ahead of the forward echo boundary (see p. 17). At the same time the density surge was propagating  $3 \text{ m sec}^{-1}$  faster than the echo boundary. Assuming that the horizontal air speed within the downdrafts supplying the gust front was not far greater than the speed of the echo boundary, the effect on the propagational speed of the gust front head was probably minimal.

Thus, it is concluded that the predominate motive force for the gust-front propagation was due to gravity. The higher wind speeds over the northern part of the NSSL observation network (Fig. 9e) were due primarily to the stronger horizontal pressure gradient in that region, apparently reflecting a greater depth of air.

In summary, approximate dynamic similarity of the 31 May gust front to gravity currents has been demonstrated. While the likelihood is small that high horizontal momentum injected into the outflow by the thunderstorm downdrafts was responsible for the slightly excessive Froude number, the possibility cannot be ruled out and remains a problem. The fundamental role of the downdraft as a supply source for the outflow was

---

<sup>1</sup>This picture contrasts with the mean profile of the peak gust speed versus distance transverse to the direction of motion determined by Colmer (1971) from 13 gust-front cases. The speed is shown to drop off steadily but slowly from the peak speed at the center.

shown to be similar to the source mechanism used in experimental gravity current studies. However, the precise role of the downdraft is still problematic.

## CHAPTER VII

### SUMMARY

A severe gust front leading the squall line of 31 May 1969 was analyzed to determine its three-dimensional structure and to investigate the mechanics of its horizontal propagation. All data measurements obtained by NSSL were utilized in the analysis.

The entire analysis of the leading part of the squall line was combined into a composite schematic model (Fig. 21). The initial change line, which preceded the leading edge of the cold outflow by 8 km, was a coincident windshift and pressure-jump line. The lack of data definition above 445 m, during the passage of this discontinuity, prevented a complete analysis. No evidence could be found to indicate that the windshift and pressure jump were due to cold-air advection associated with the gust front. Instead, substantial evidence is demonstrated to indicate the discontinuity was due to a gravitational wave "jump" (Tepper, 1950, 1955) propagating on a 740-mb thermal inversion (Fig. 21). However, an attempt to determine a link between such a gravity wave and the gust front is beyond the scope of the analysis.

During the period of the analysis, the leading edge of the gust front was well ahead of the precipitation area (20 km ahead) and was propagating steadily at  $21 \text{ m sec}^{-1}$ . The radar echo from

which the outflow emanated was in the "late" mature stage and was moving  $3 \text{ m sec}^{-1}$  slower than the gust front.

The shape of the cold-air outflow constituting the gust front was defined in a vertical plane section taken normal to the line tangent to the leading edge. At the front of the cold air a "projecting nose" was found, whose foremost extension was located about 750 m above ground level and 1.3 km forward of the cold-air boundary at the ground. The depth of the cold air exhibited a maximum of 1700 m near the front of the outflow air mass and immediately decreased to a near-uniform upstream value of about 1350 m (Fig. 21). Thus, an "elevated head" appeared at the air-mass front. The geometry of the air-mass profile is quite similar to the characteristic profile of the steady-flow gravity currents formed in stratified liquids in laboratory tank experiments by Keulegan (1958). It is also in accord with the theoretical shape of cold "kata-fronts" (Ball, 1960) where frictional stress is taken into account.

The ambient air flow toward the head, which is deflected upwards in the nose region, and the circulation field inside the cold air mass is also similar to analogous flow features revealed by laboratory gravity currents. Just ahead of the nose upward velocities up to  $2.5 \text{ m sec}^{-1}$  at the 400 m level were computed and values up to  $5 \text{ m sec}^{-1}$  at higher levels were inferred as the ambient air flow was lifted up and over the head (as seen by a coordinate axis translating with the head at  $20 \text{ m sec}^{-1}$ ). Within the cold air-mass head the circulation field featured a horizontal wind speed maximum of  $13 \text{ m sec}^{-1}$  (with respect to the translating

reference axis) at a height of 180 m above the ground (Fig. 21). This feature corresponds to the "undercurrent" in laboratory gravity flows. This undercurrent is deflected upwards in the nose region and finally rearward near the crest of the head. In the wake region of the head, where general downward air motion is evidenced by analyzed downward components up to  $1 \text{ m sec}^{-1}$  at 400 m, the wind velocity and temperature fields were quite turbulent. Eddy mixing of ambient air in the wake of the head crest and a steady downward flux of this air mixture is postulated to explain these observations. Vigorous eddy mixing is also implied beneath the nose. These entrainment mechanisms evidently tended to erode the cold-air head but this erosion was counteracted by a steady upstream inflow of cold air. This ambient and internal flow field associated with the gust front is remarkably similar to analogous features of gravity currents as deduced by Prandtl (1952) and as observed in laboratory experiments by Middleton (1966) and Simpson (1969).

It was demonstrated that the gust front was approximately dynamically similar to theoretical and experimental gravity currents by the near-equivalent values of the respective internal Froude numbers. It was shown that the gust front Froude number was only 25 percent larger than those obtained in laboratory currents but this percentage excess was greater when compared to larger scale atmospheric cold surges. It is reasoned that Froude numbers of thunderstorm outflow air masses are sometimes larger because the horizontal displacement speed of the outflow is boosted by the injection of high horizontal-momentum air transferred to the ground in the storm downdraft. However, in the 31 May case this effect was likely to be small (as the near correspondence of Froude numbers would suggest).



because the gust front was propagating faster than the parent echo and the latter was in the late mature stage.

## BIBLIOGRAPHY

- Barclay, P.A. and K.E. Wilk, 1970: Severe thunderstorm radar echo motion and related weather events hazardous to aviation operations. National Severe Storms Laboratory, Tech. Memo No. 46, 63 pp.
- Benjamin, T.B., 1968: Gravity currents and related phenomena. Part 2, J. Fluid Mech, 31, 209-248.
- Berson, F.A., 1958: Some measurements of undercutting cold air. Quart. J.R. Meteor. Soc, 84, 1-16.
- Browning, K.A. and T.W. Harrold, 1970: Air motion and precipitation growth at a cold front. Quart. J.R. Meteor. Soc., 96, 369-389.
- Byers, H.R. and R.R. Braham, Jr., 1949: The Thunderstorm. Washington, D.C., U.S. Government Printing Office, 287 pp.
- Carter, J.K., 1970: The meteorological instrumented WKY-TV tower facility. National Severe Storms Laboratory, Tech. Memo. No. 50, 18 pp.
- Charba, J. and Y. Sasaki, 1971: Structure and movement of the severe thunderstorms of 3 April 1964 as revealed from radar and surface mesonet network data analysis. J. Meteor. Soc. Japan, 49, 191-214.
- Clarke, R.H., 1961: Mesostructure of dry cold fronts over featureless terrain. J. Meteor., 18, 715-735.
- Cook, B.J., 1961: Some LEWP observations and associated severe weather. Proc. Ninth Wea. Radar Conf., Kansas City, Missouri, pp. 181-185.
- Colmer, M.J., 1971: On the characteristics of thunderstorm gust fronts. Royal Aircraft Est., Bedford, Eng. 11 pp.
- Daly, B.J. and W.E. Pracht, 1968: Numerical study of density-current surges, Phys. Fluids, 10, 15-30.
- Farquharson, J.S., 1937: Haboobs and instability in Sudan. Quart. Jour. Royal Meteor. Soc., 63, 393-414.
- Fujita, T., 1959: Precipitation and cold air production in mesoscale thunderstorm systems. J. Meteor., 16, 454-466.

- \_\_\_\_\_, 1963: Analytical mesometeorology: A review. Meteor. Monogr., 5, 77-125.
- \_\_\_\_\_, 1966: Detailed investigation of mesometeorological conditions of the squall line of August 6-7, 1966 which crossed the air route between Kansas City, Missouri and Omaha, Nebraska. Part III: Turbulence in relation to the squall line. Prepared for the British Aircraft Corp. (USA), Inc., 27 pp.
- Koschmieder, H., 1932: Danziger Seewind Studien I. Forch Met. Inst., Danzig, 8, 49 pp.
- \_\_\_\_\_, 1941: Danziger Seewind Studien II, Ibid., 10, 39 pp.
- Kuelegan, G.H., 1958: Twelfth progress report on model laws for density currents; the motion of saline fronts in still water. U.S. Natl. Bur. Standards, Rept. No. 5831, 28 pp.
- Lidga, M.G.H. and S.G. Bigler, 1958: Radar echoes from a cloudless cold front. J. Meteor., 15, 494-501.
- Maxwell, B.L., 1971: Convergence of solution in variational analysis with application to wind fields and omega field analysis. Master's Thesis, (Unpublished) Univ. of Okla. 57 pp.
- Middleton, G.V., 1966: Experiments on density and turbidity currents. I. Motion of the head. Can. J. Earth Sci., 3, 523-546.
- Nolen, R.H., 1959: A radar pattern associated with tornadoes. Bull. Am. Meteor. Soc., 40, 277-279.
- Newton, C.W., 1950: Structure and mechanism of prefrontal squall line. J. Meteor., 7, 210-222.
- Newton, C.W. and H.R. Newton, 1959: Dynamical interaction between large convective clouds and environment and vertical shear. J. Meteor., 16, 483-353.
- Prandtl, L., 1952: Essentials of Fluid Dynamics. London, Blackie & Son., 452 pp.
- Sasaki, Y., 1959: A numerical experiment for squall-line formation. J. Meteor., 16, 347-353.
- Sasaki, Y., 1970: Numerical variational analysis with weak constraint and application to surface analysis of severe storm gust. Mon. Wea. Rev., 98, 399-410.
- Simpson, J.E., 1969: A comparison between laboratory and atmospheric density currents. Quart. J.R. Meteor. Soc., 95, 758-756.

- Sullivan, T.J., 1971: A study of variational analysis of wind fields with application to vertical motion ( $w$ ) fields, Master's Thesis, (Unpublished) Univ. of Okla., 58 pp.
- Tepper, M., 1950: A proposed mechanism of squall lines: The pressure jump line. J. Meteor., 7, 21-29.
- \_\_\_\_\_, 1955: On the generation of pressure jump lines by the impulsive addition of momentum to simple current systems. J. Meteor., 12, 287-297.
- von Kármán, T., 1940: The engineer grapples with nonlinear problems. Bull. Am. Math. Soc., 46, 615-683.
- Wallington, C.E., 1959: The structure of the sea-breeze front as revealed by gliding flights, Weather, 14, 263-270.
- Yih, C.-S., 1969: Stratified flows. The Annual Review of Fluid Mechanics. Palo Alto, Calif. Annual Rev., Inc., pp. 106-108.

TABLE 1  
STORM DAMAGE REPORTS

Rept. No.	Quoted Remarks of Volunteer Observers	Damaging Wind			Rain		
		Began (CST)	Ended (CST)	Dir.	Began (CST)	Ended (CST)	Amt (n.)
1b	Considerable damage to limbs of trees. Some damage to cotton and barley crops due to strong NW wind. Considerable blowing dust.	2200	0030	NW	--	--	0
2b	Winds were clocked up to 65 mph. Significant damage to trees and crops.	2200 (?)	0000	?	2200	0000	1.78
1d	Some trees uprooted and outbuildings damaged; gardens were flattened.	2245	0000	NW	2255	?	3.00
2d	Severe damage to vegetation. Every large tree suffered some limb breakage. Several large trees were blown over. Several trailer houses were severely damaged. Three persons received minor injuries.	2300	?	?	?	?	?
3d	Wind estimated 65-75 mph. Damage to barn two miles north. Storms raged for several hrs 20-40 mile N of us.	2300*	2310	N	?	?	0.20
1e	Three persons were injured in overturned camper trailer.	2300	?	?	?	?	?
2e	Hail 3/4 inches in diameter 2313-2320. No wind report.	?	?	?	2313	2320	0.30
3e	Tree-limb damage everywhere.	2310	?	NW	2316	2345	0.60
1f	Had 1/2 inch diameter hail during 2331-2333 CST. Little damage to trees(?)	2321	2340	W- NW	2333	2337	0.80
1g	Light damage to trees and utility lines in north and west Oklahoma City. Peak wind gust measured on WKY-TV tower was 76 mph.	2330	2345	NW	2345	--	--
2g	Wind estimated 60-65 mph. Little damage to trees and crops.	0000	0020	N- NE	0030	0050	0.50
3g	Hail 1/2 inches in diameter fell between 0000-0010. Little damage to crops by wind.	0010	0100	W- NW	?	?	0.30
4g	Little damage to trees.	0020	0100	NW	0030	0100	2.10
5g	Some leaves and branches broken off trees but damage was relatively small.	0030	0200	NW	0100	0245	0.40
6g	Little damage to trees by wind.	0050	0110	?	0118	0140	0.60

TABLE 2

## RADAR ECHO PROPERTIES OF DAMAGING THUNDERSTORMS

Storm	Rept. No.	Time (CST)	Translation Speed (kts)	Dia. (nm)	Height (kft)	Reflectivity Factor (dbZ) <sup>1</sup>	Prior Duration (hrs)
A	1 <sub>b</sub>	2200	20	20	54	52	2
B	2 <sub>b</sub>	2200	15-20	20	49	52	2
A	1 <sub>d</sub>	2245	25	25	51	45	3
A	2 <sub>d</sub>	2255	28	25	50	47	3
A	3 <sub>d</sub>	2300	21	20	48	48	3
C	1 <sub>e</sub>	2310	24	17	48	55	1½
C	2 <sub>e</sub>	2310	24	17	48	55	1½
A	3 <sub>e</sub>	2310	30	23	46	45	3½
A	1 <sub>f</sub>	2321	25	19	48	39	3½
A	1 <sub>g</sub>	2330	20	18	45	42	3 3/4
C	2 <sub>g</sub>	0000	20	18	48	50	1 3/4
C	3 <sub>g</sub>	0010	20	18	48	50	1 3/4
A	4 <sub>g</sub>	0020	-	Miss- ing	-	-	-
A	5 <sub>g</sub>	0030	-	"	-	-	-
A	6 <sub>g</sub>	0050	-	"	-	-	-

<sup>1</sup> Zero degrees elevation,  $p_{dbZ} = 10 \log \frac{Z}{(1 \times 10^0)}$ , Z--reflectivity factor

TABLE 3

## GRAVITY CURRENT RELATIONSHIPS APPLIED TO THE GUST-FRONT AIR MASS

	Temperature Deficit (°C)	Depth	Density Ratio	Displacement Speed (m sec <sup>-1</sup> )		
		d(m)	$\frac{\bar{\rho}_2 - \bar{\rho}_1}{\bar{\rho}_1}$	$1.1\sqrt{gd \frac{\bar{\rho}_2 - \bar{\rho}_1}{\bar{\rho}_1}}$	$1.4\sqrt{gd \frac{\bar{\rho}_2 - \bar{\rho}_1}{\bar{\rho}_1}}$	Observed
CASE I ( $\Delta P=2.2\text{mb}$ )	5	1220	$1.97 \times 10^{-2}$	16.9	21.9	20.0
	4	1500	$1.91 \times 10^{-2}$	18.6	23.6	"
CASE II ( $\Delta P=6.2\text{mb}$ )	5	3150	$2.00 \times 10^{-2}$	27.1	35.1	"
	4	3900	$1.93 \times 10^{-2}$	29.8	38.5	"

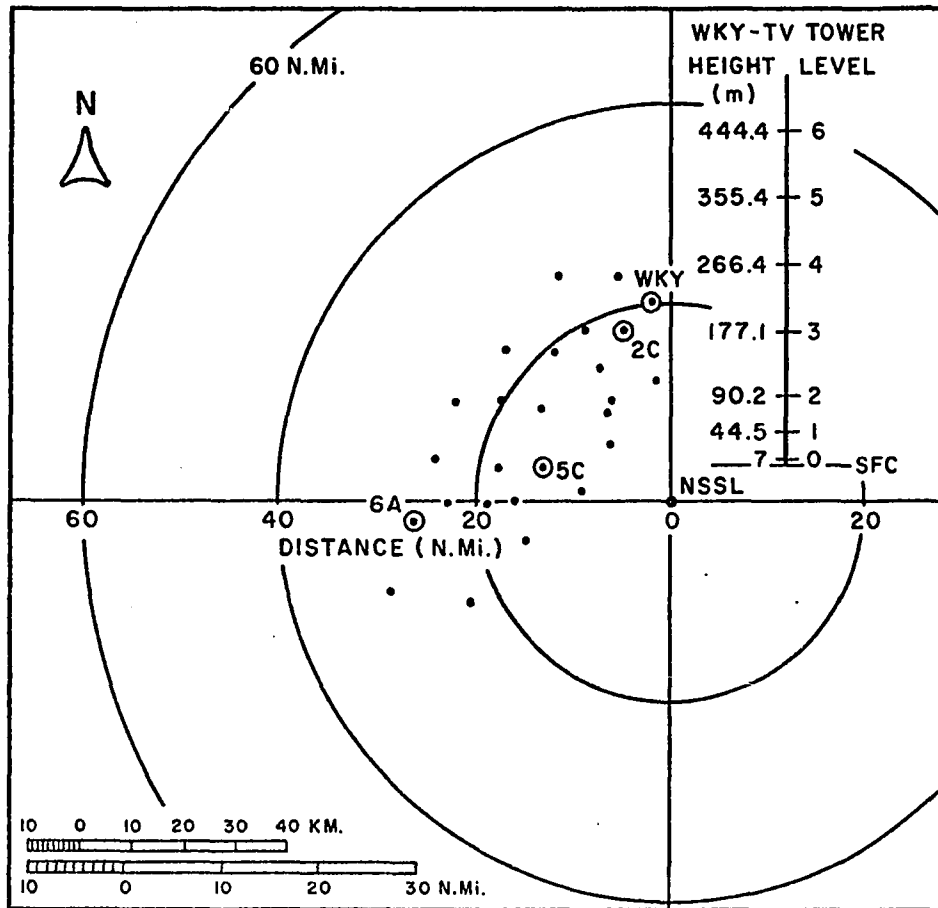


Fig. 1. High density surface observation network and instrumented TV-tower facility employed by the National Severe Storms Laboratory (NSSL), Norman (NRO), Okla. in 1969. Network stations WKY, 2C, 5C, and 6A are labeled as their records are later used for illustrating the surface weather changes. The range circles of the radar based at NSSL are at 20 nm intervals. The inset (upper right) shows the instrumented levels of the WKY-TV tower.



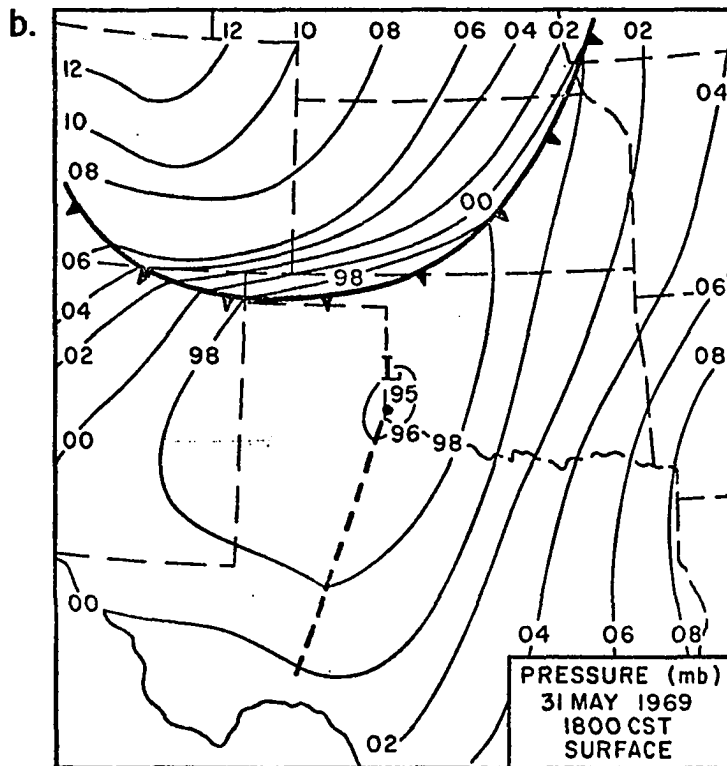
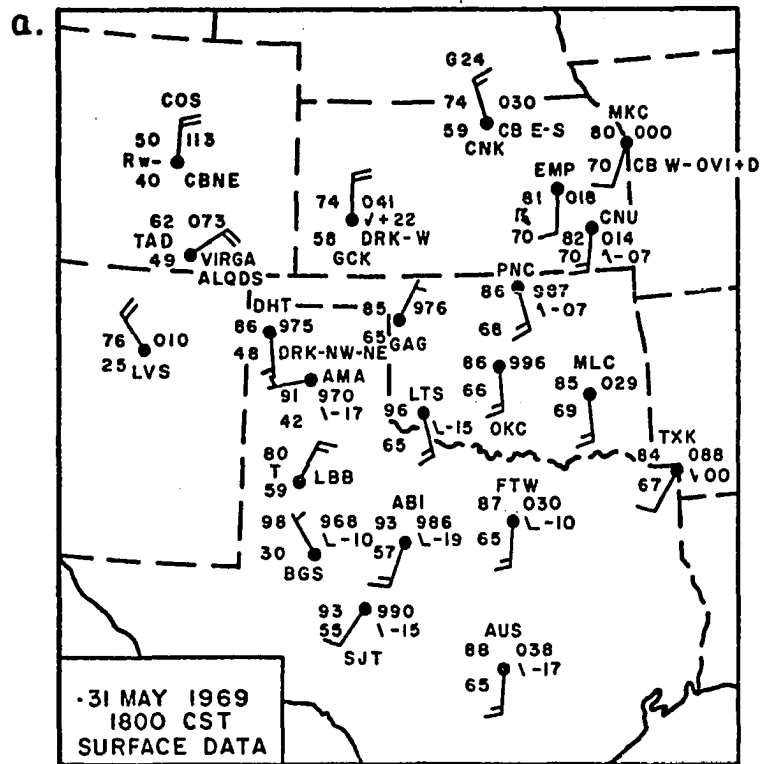


Fig. 2. Sub-synoptic section maps. Fig. 2a is the regular NWS surface station data for which analyses are shown in 2b, 2c, and 2d. In 2b isobars are drawn at 2-mb intervals.

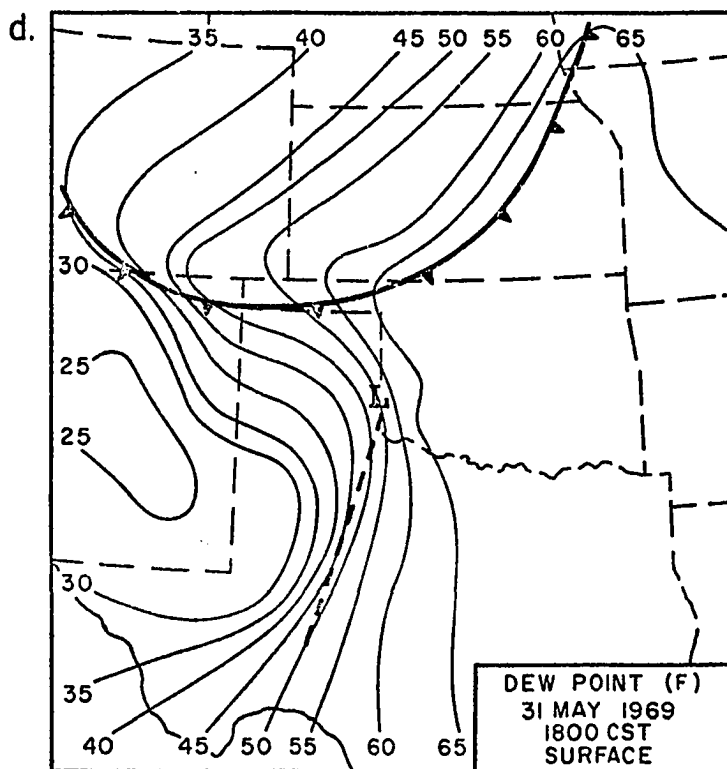
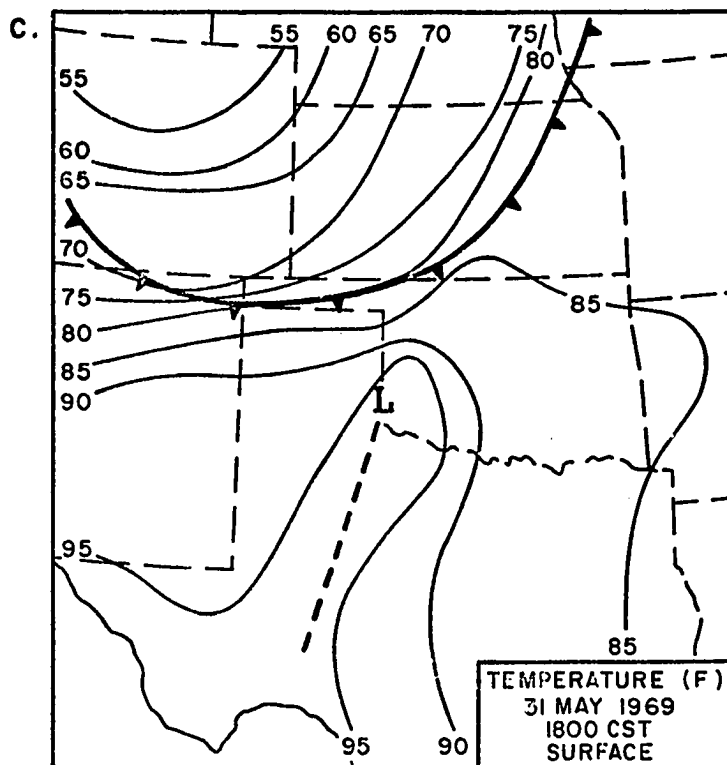


Fig. 2 cont. Isotherms and isodrosotherms shown in 2c and 2d, respectively, are at 5F intervals.

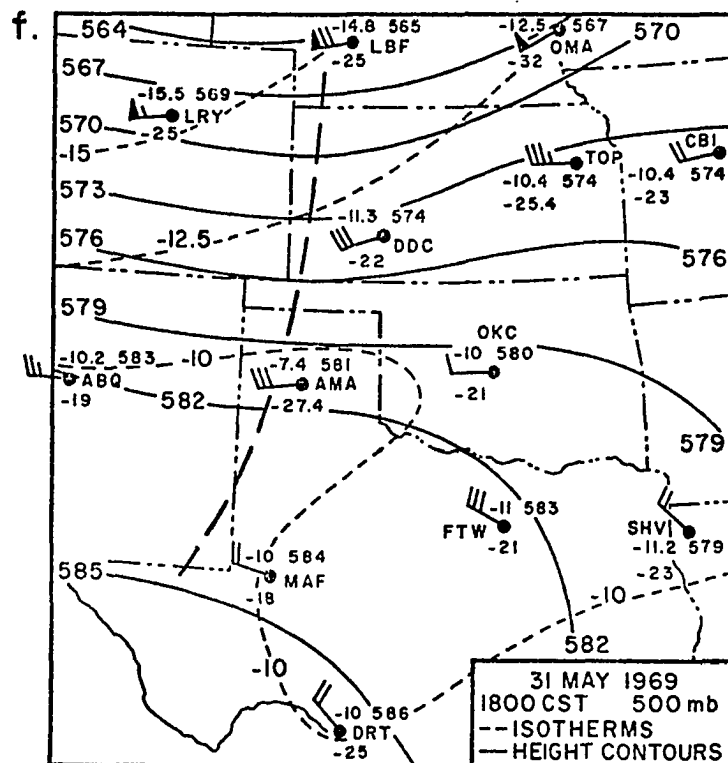
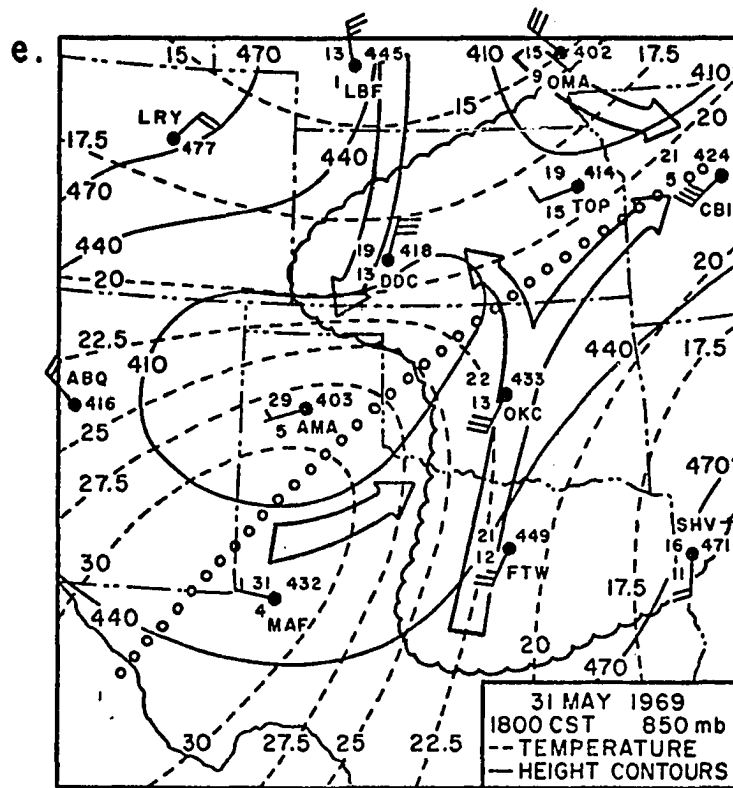


Fig. 2 cont. In both 2e and 2f height contours (decameters) are solid and isotherms (C) are dashed. The broad arrows in 2e indicate the dominant 850 mb currents and the area enclosed by the wavy line represents dew point temperatures in excess of 10C.

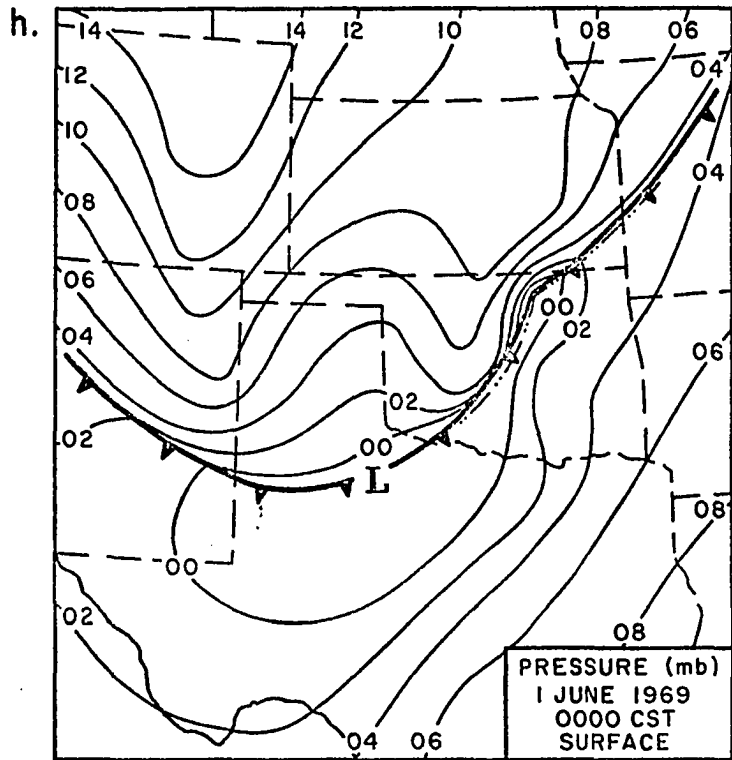
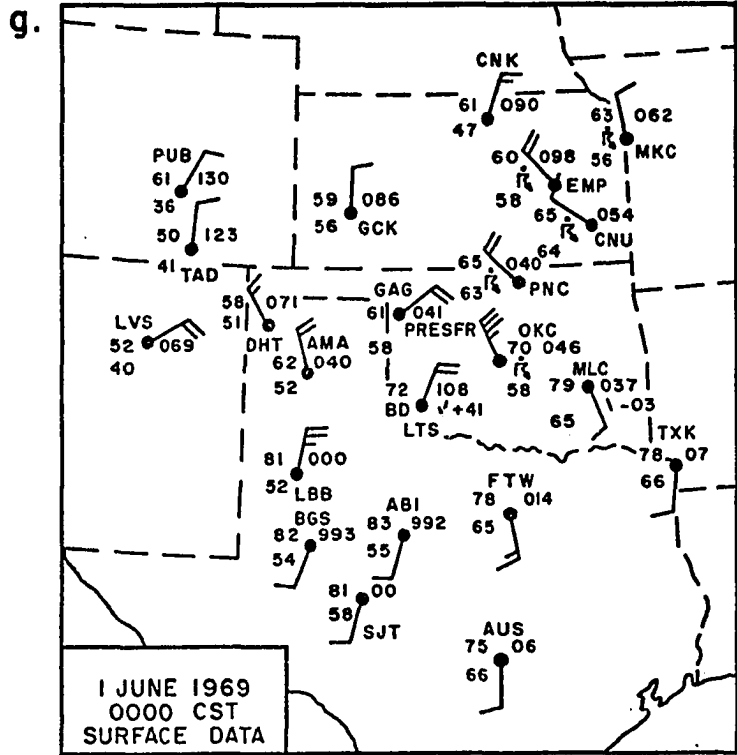


Fig. 2 cont. Fig. 2g and 2h have the same conventions as Fig. 2a and 2b.

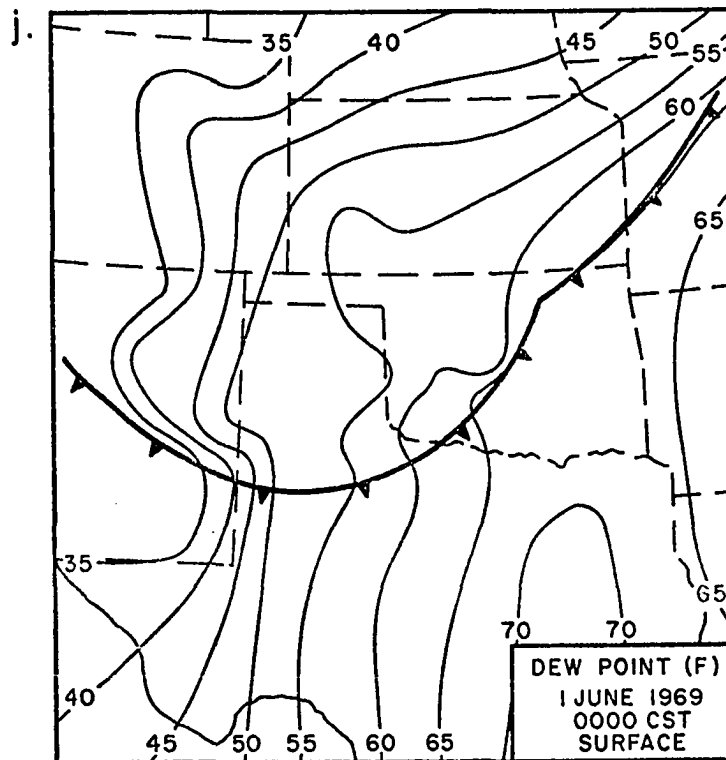
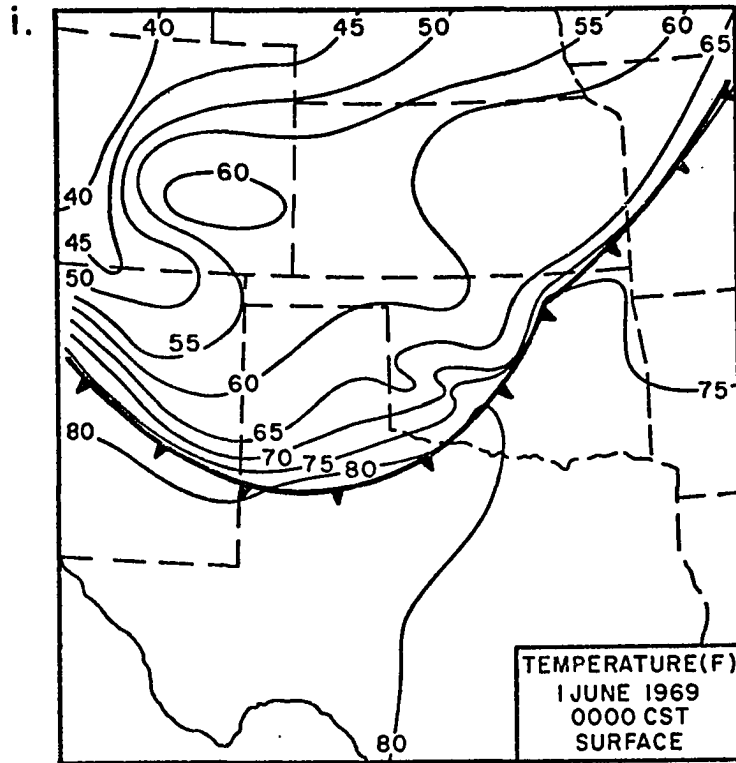


Fig. 2 cont. Fig. 2i and 2j have the same conventions as Fig. 2c and 2d.

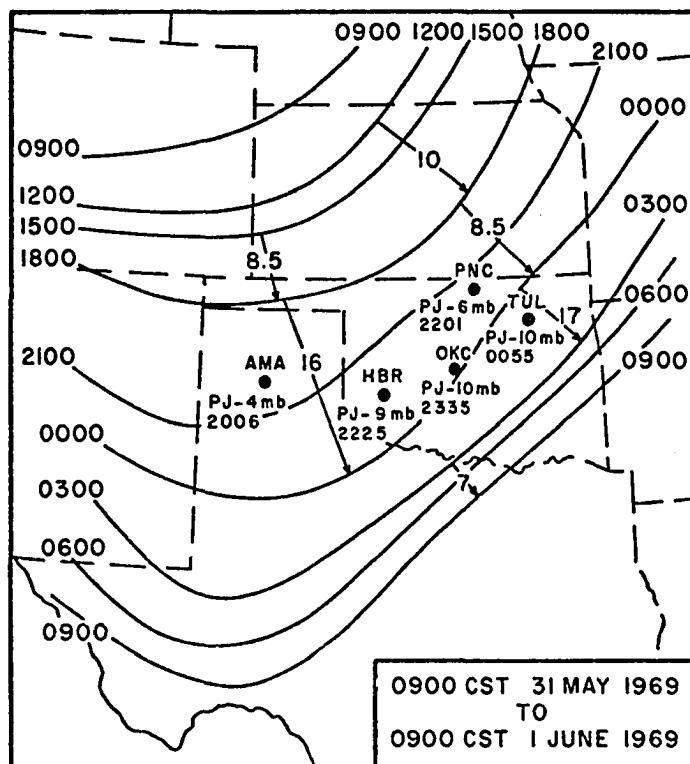


Fig. 3. Sequence of frontal positions. The average propagation speed ( $\text{m sec}^{-1}$ ) is shown within the time period spanned by the arrows. PJ denotes a pressure jump at the indicated time (CST).

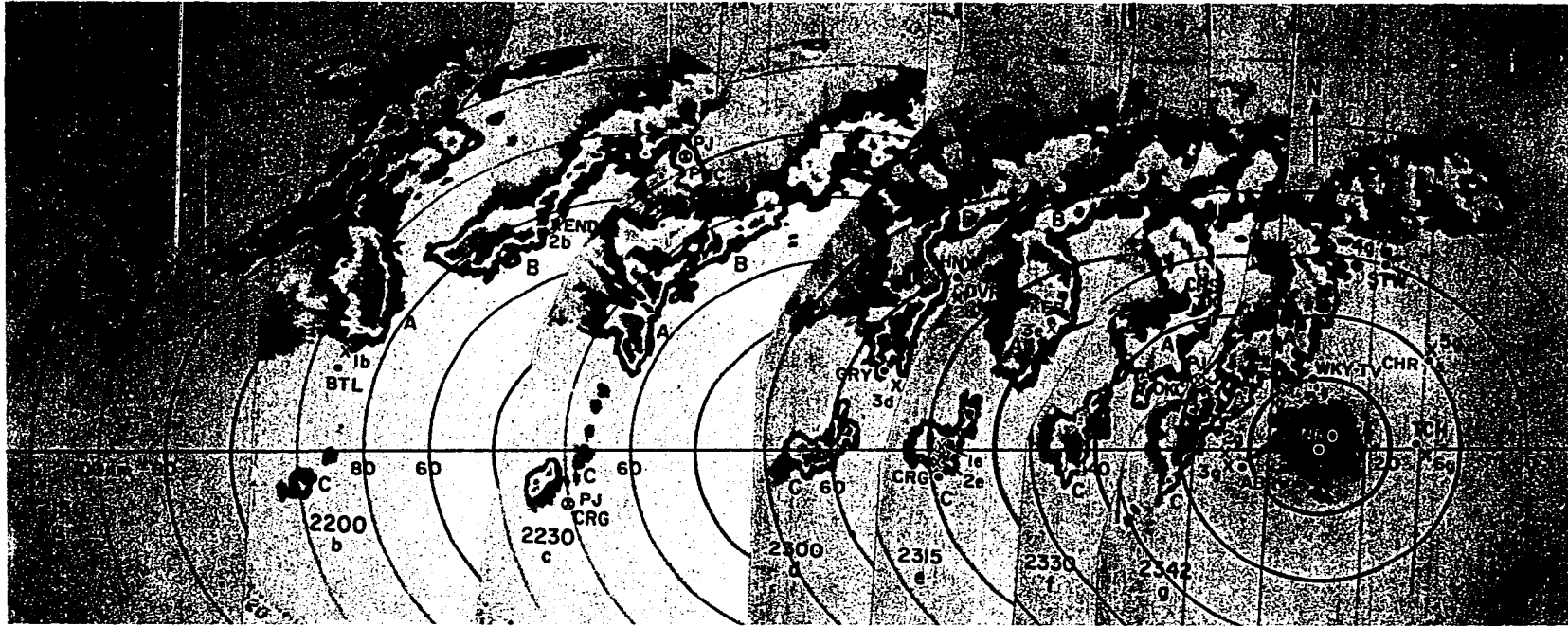


Fig. 4. Time sequence (CST) of the radar echo pictures of the 31 May 1969 squall line. These pictures are photographs of the PPI scope of the WSR-57 radar operating at zero degrees elevation from Norman, Oklahoma (NRO). The echoes are shade-contoured according to reflectivity factor thresholds beginning at about  $2 \times 10^1 \text{ mm}^6 \text{ m}^{-3}$  and thereafter incrementing by factors of 10. Storm damage reports are located by X-marks and labeled. Each report, identified by identical labels, is described in Table 1. Oklahoma towns near the damage reports are (from left-to-right) BTL (Butler), END (Enid), PNC (Ponca City), GRY (Geary), HNY (Hennessey), CRG (Carnegie), KFR (Kingfisher), CRS (Crescent), ABR (Amber), WKY-TV (instrumented TV tower in OKC), STW (Stillwater), CHR (Chandler), and TCH (Tecumseh).

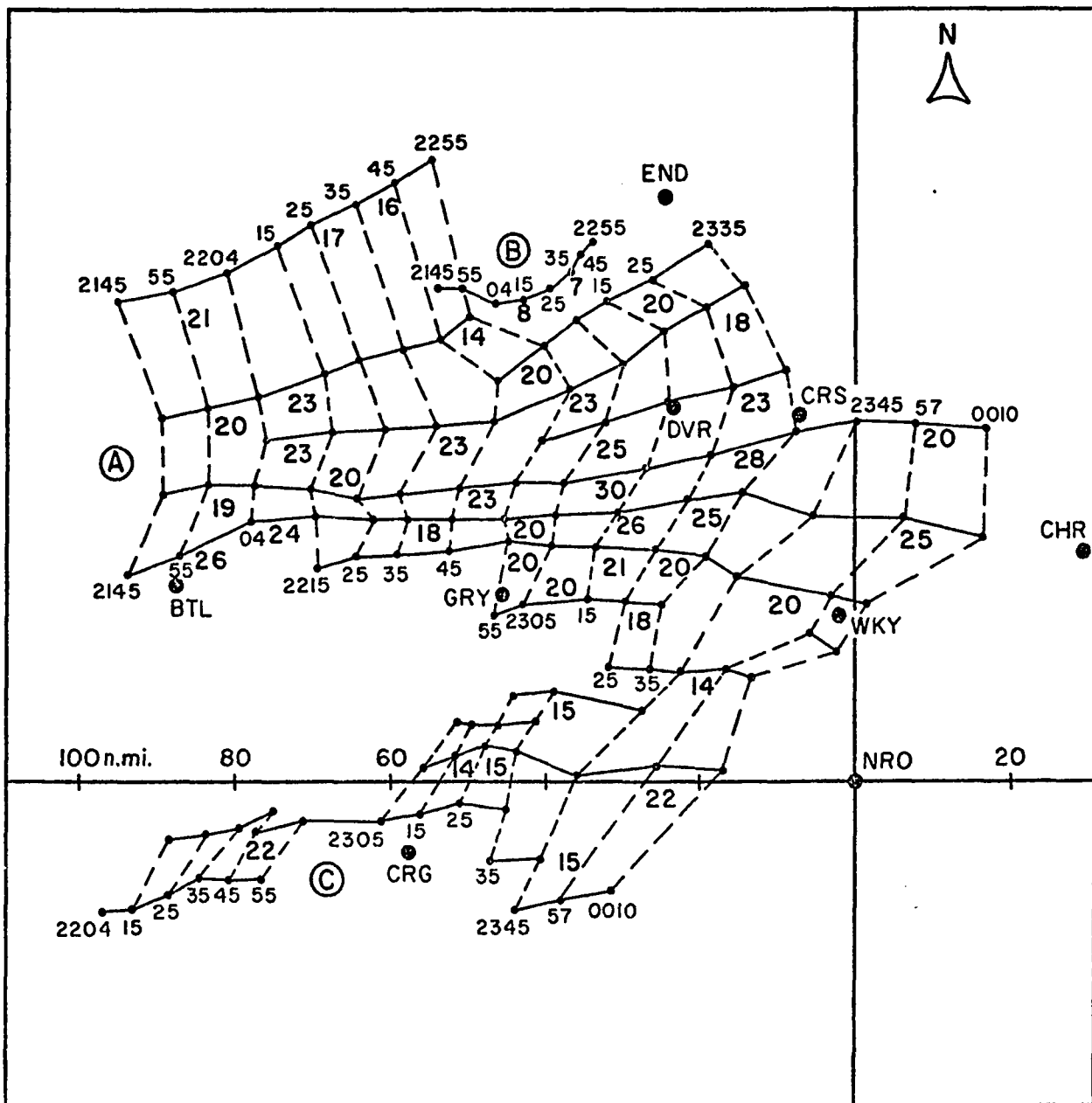


Fig. 5. Pattern of tracks (solid lines) of peak reflectivity elements of the echoes shown in Fig. 4. Dashed lines are peak echo element isochrones. Bold numbers are the echo speeds ( $\text{m sec}^{-1}$ ) averaged over 10-min. periods. A, B, and C refer to the major thunderstorm echoes in Fig. 4.



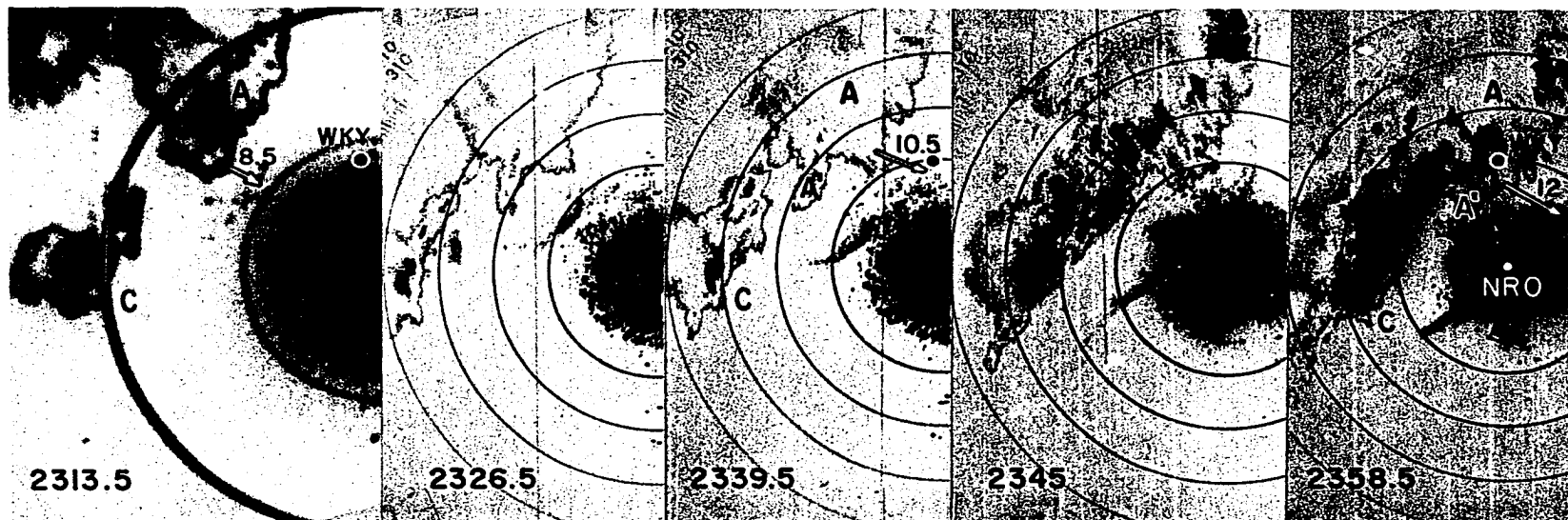


Fig. 6. Time sequence (CST) of PPI displays showing the "thin line" echo and the trailing precipitation echoes at zero deg. elevation. In the first picture (left) the range circles are at 25 nm intervals while the remaining four pictures have 10 nm range circles. Distances between the echo boundary and the "thin line" are spanned by arrows. Units: nautical miles.

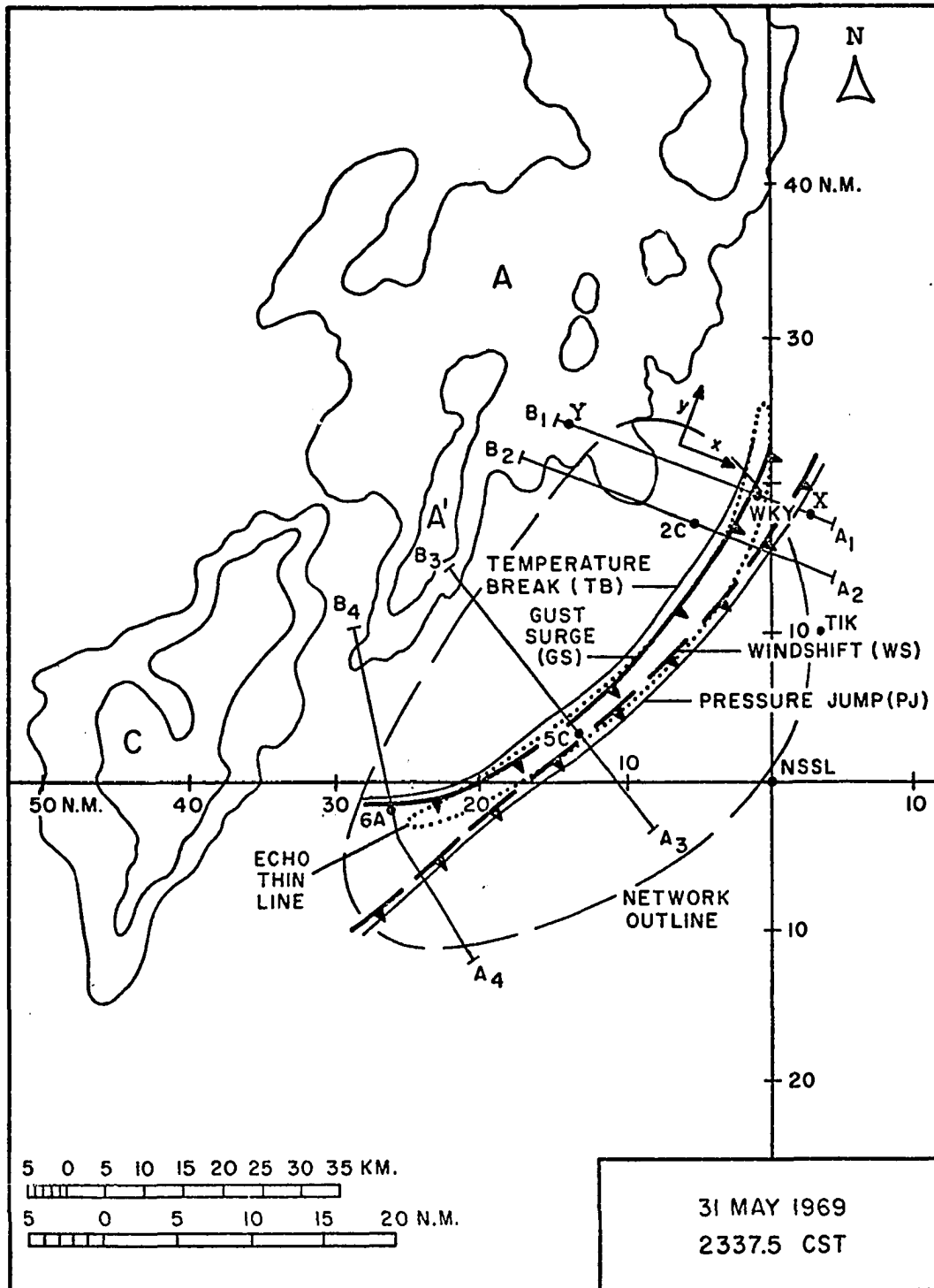


Fig. 7. Major squall line features at 2337 $\frac{1}{2}$  CST. The PPI radar echo tracing is of the  $2 \times 10^1$  and  $2 \times 10^4$   $\text{mm}^6 \text{m}^{-3}$  reflectivity factor contours. XY is the section line for the plane of vertical cross-section analysis of the WKY tower data shown in Figs. 9 and 11. A<sub>1</sub>B<sub>1</sub>, A<sub>2</sub>B<sub>2</sub>, etc. are section lines for the time-to-space converted surface network data traces of the stations indicated. The corresponding spatial traces are shown in Fig. 10.

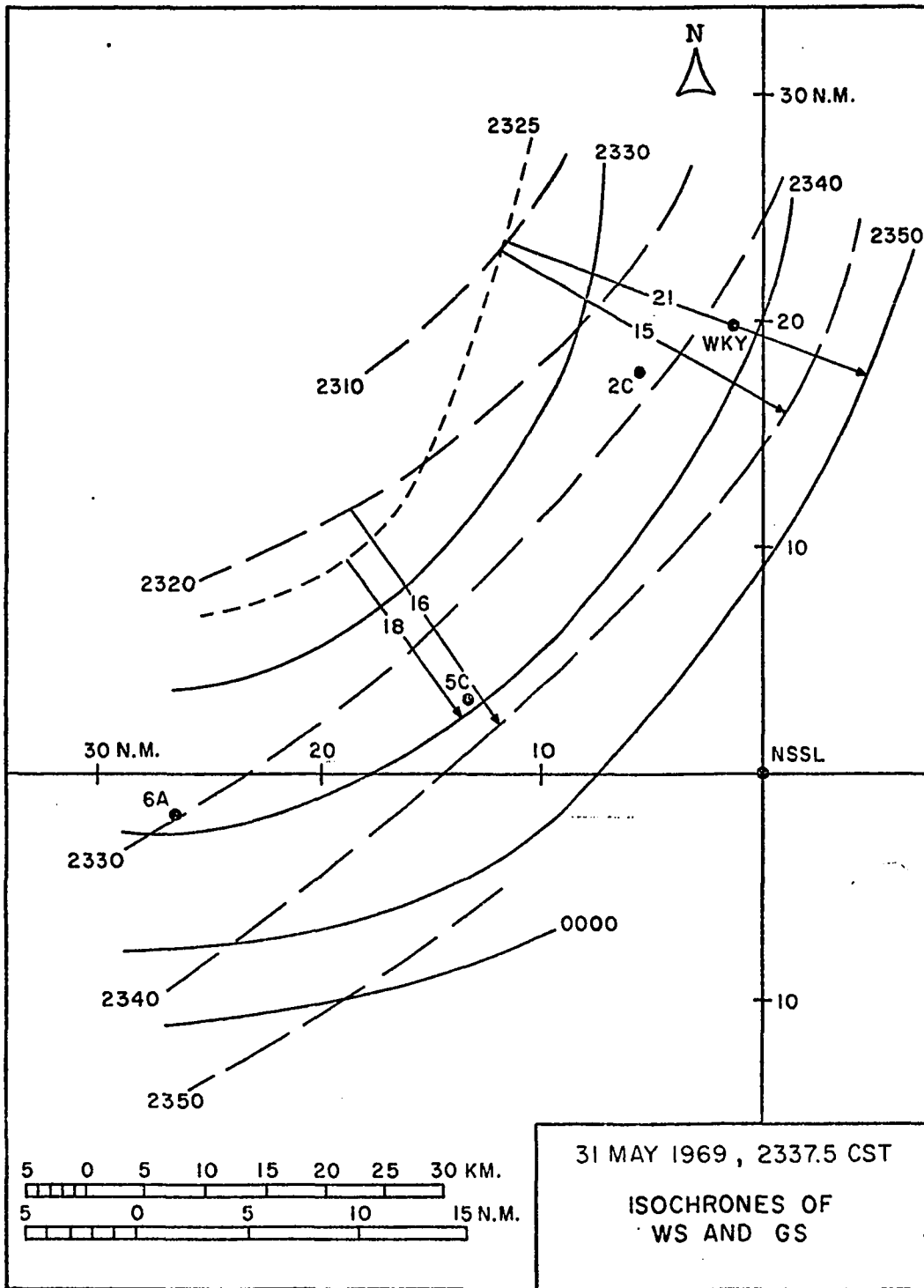


Fig. 8. Sequence of the windshift (dashed) and gust-surge (solid) isochrones. The isochrone displacement speeds ( $m\ sec^{-1}$ ) are also shown.

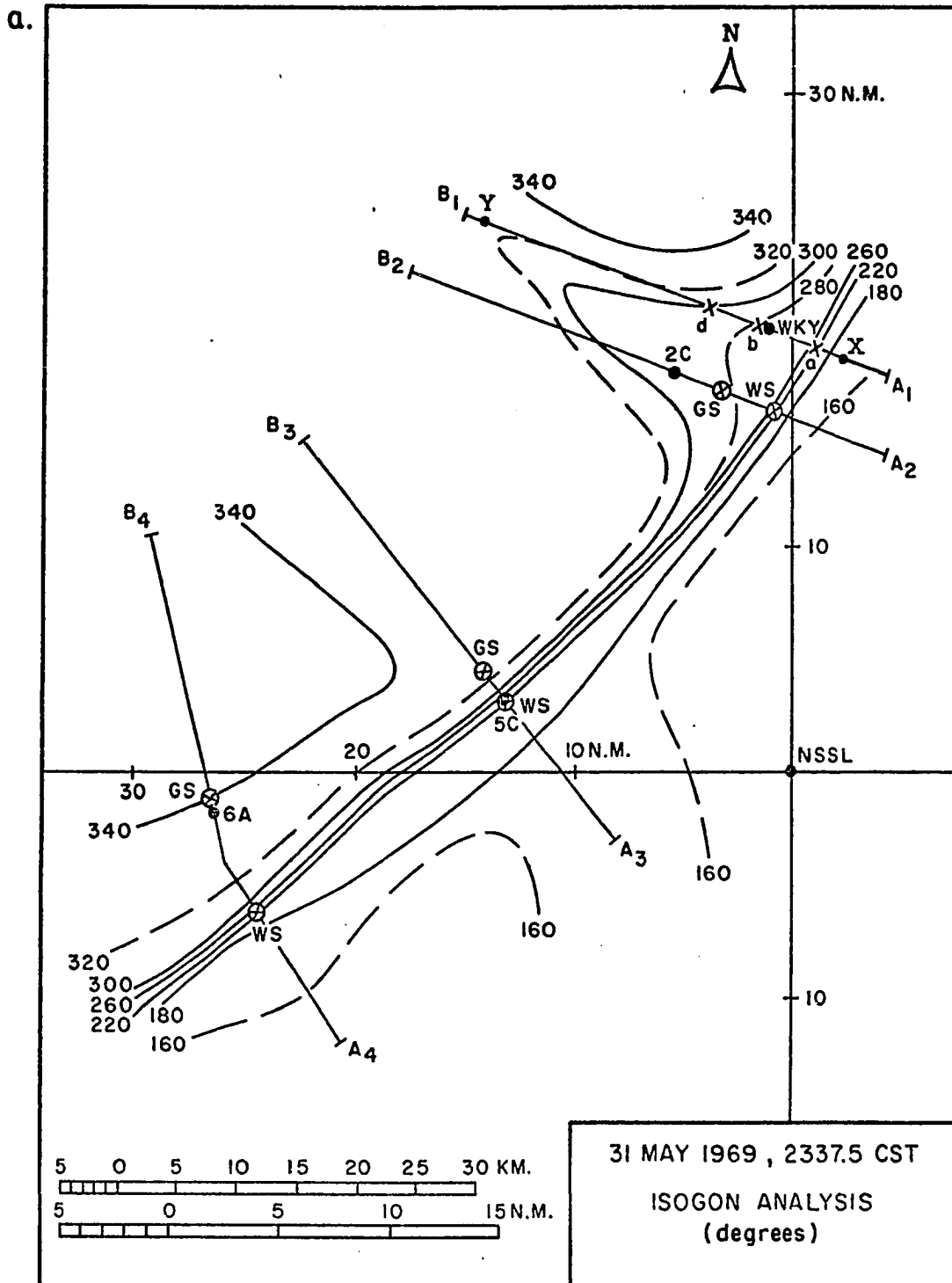


Fig. 9. Network and tower wind analyses. In the isogon analysis (9a, above) carefully note the labeling of each isogon. Included in all network wind fields, i.e. Fig. 9a, 9c, 9e, and 9g, are section lines for the spatial wind variations of surface network stations shown in Fig. 10. The points where the windshift and gust surge intersect these lines is labeled WS and GS respectively.

b. 31 MAY 1969, ISOGON ANALYSIS (degrees)

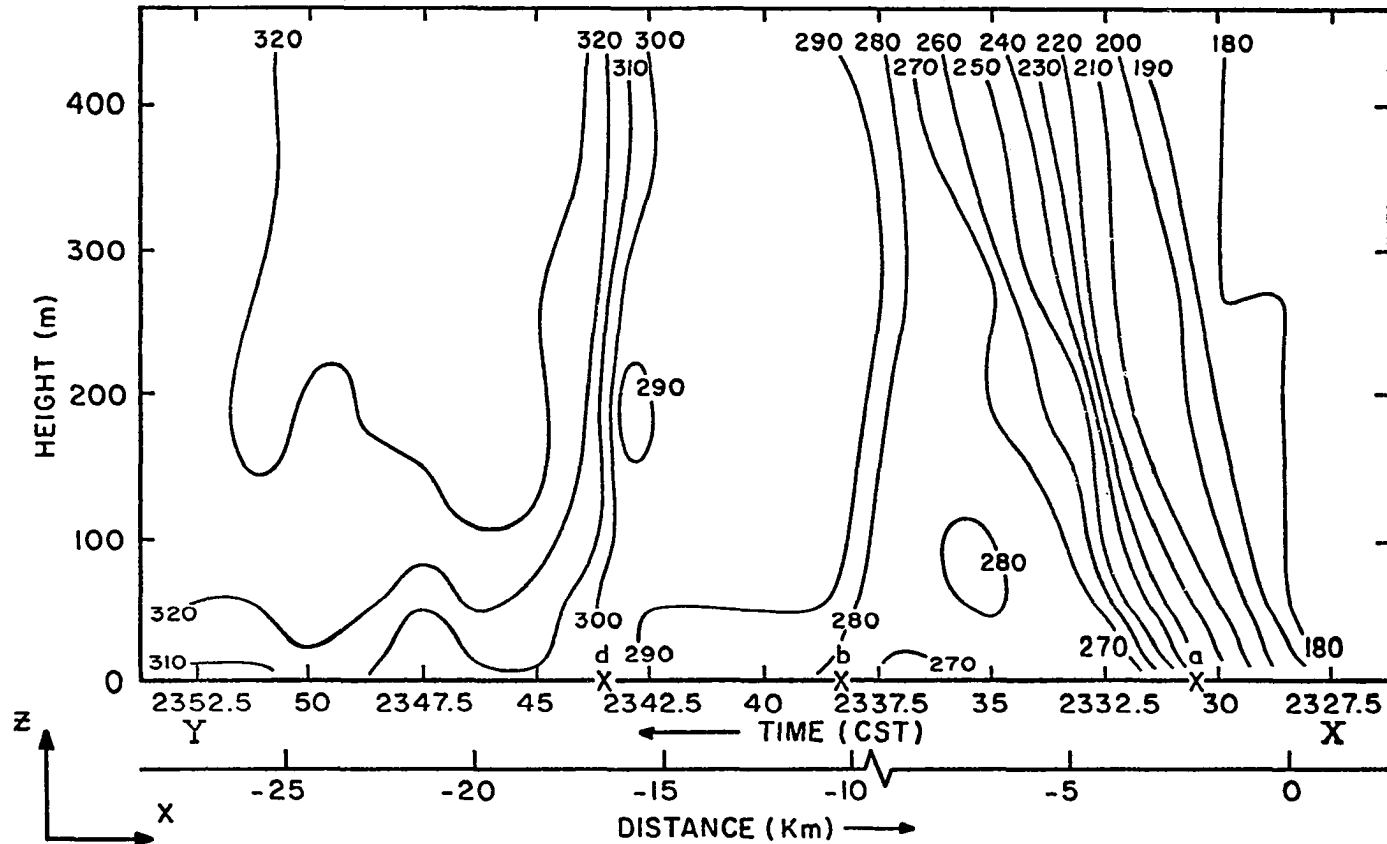


Fig. 9 cont. (9b). Vertical cross section isogon analysis at WKY. All the vertical sections at WKY, i.e., Fig. 9b (above), 9d, 9f, and 9h, are aligned in the direction of flow and their horizontal extent is indicated by XY in all network fields. Corresponding features appearing in the network fields and at the surface level of the vertical sections are labeled identically as shown.

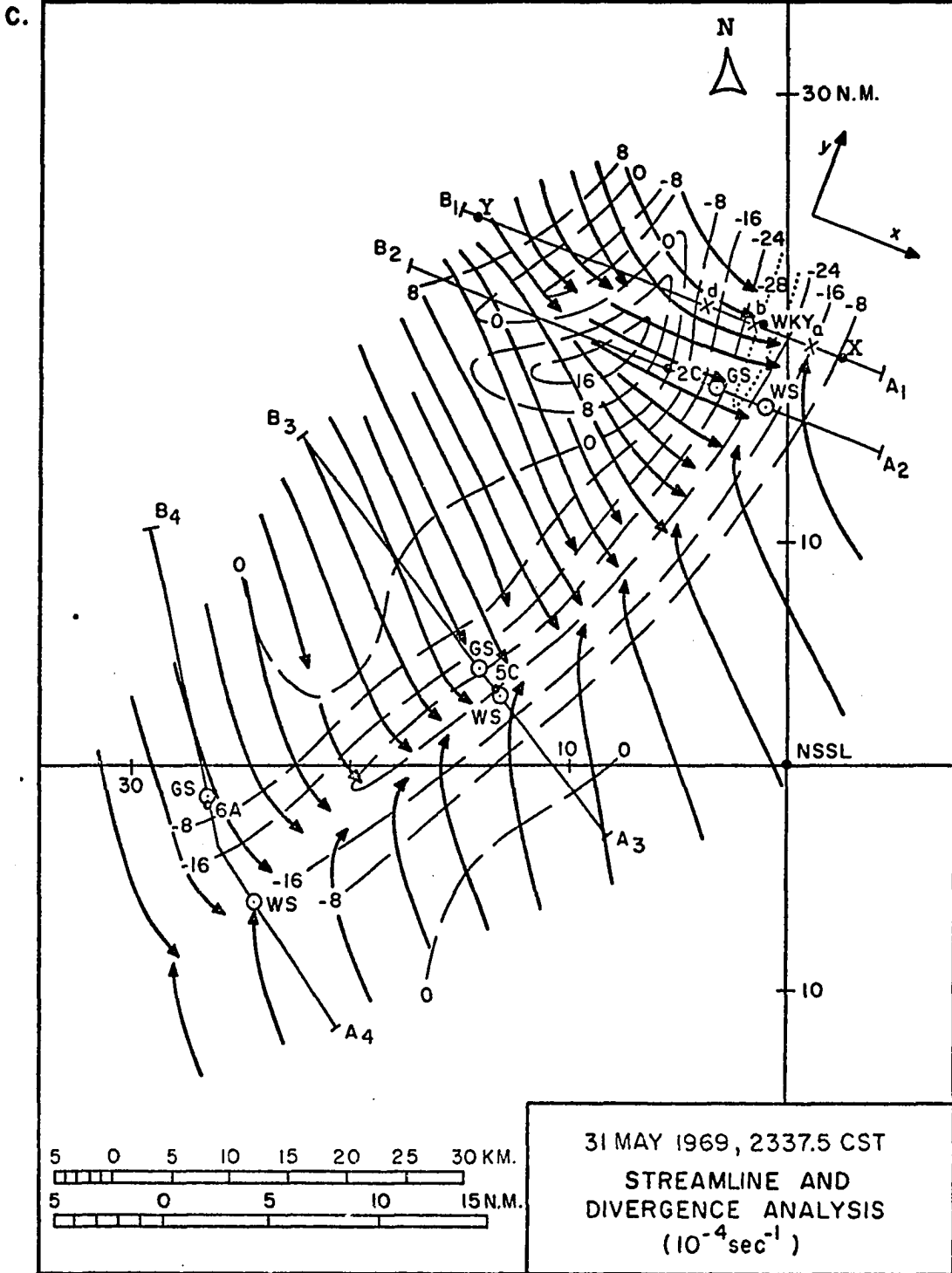


Fig. 9 cont.

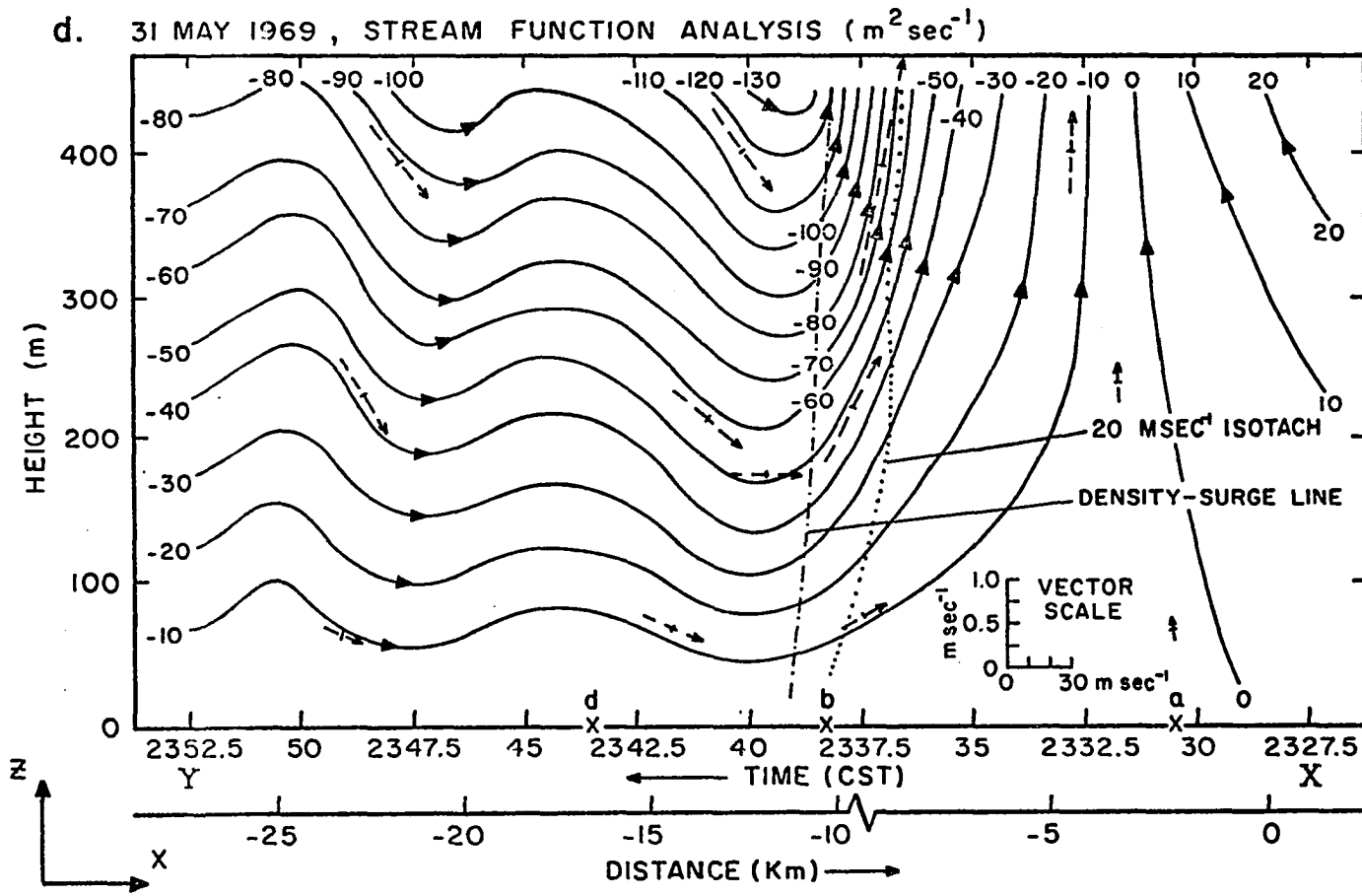


Fig. 9 cont.

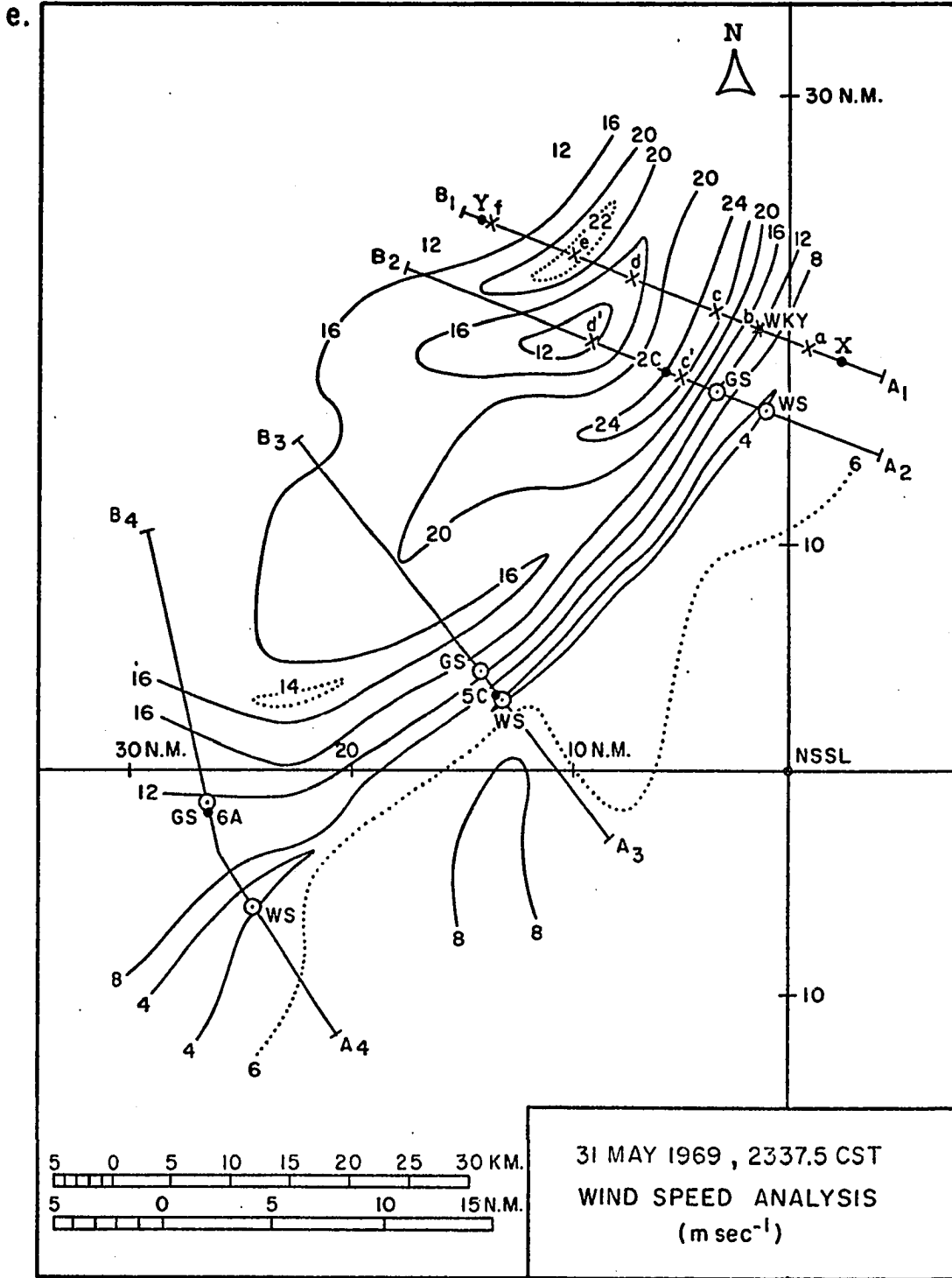


Fig. 9 cont.



f. 31 MAY 1969 , WIND SPEED ANALYSIS ( $\text{m sec}^{-1}$ )

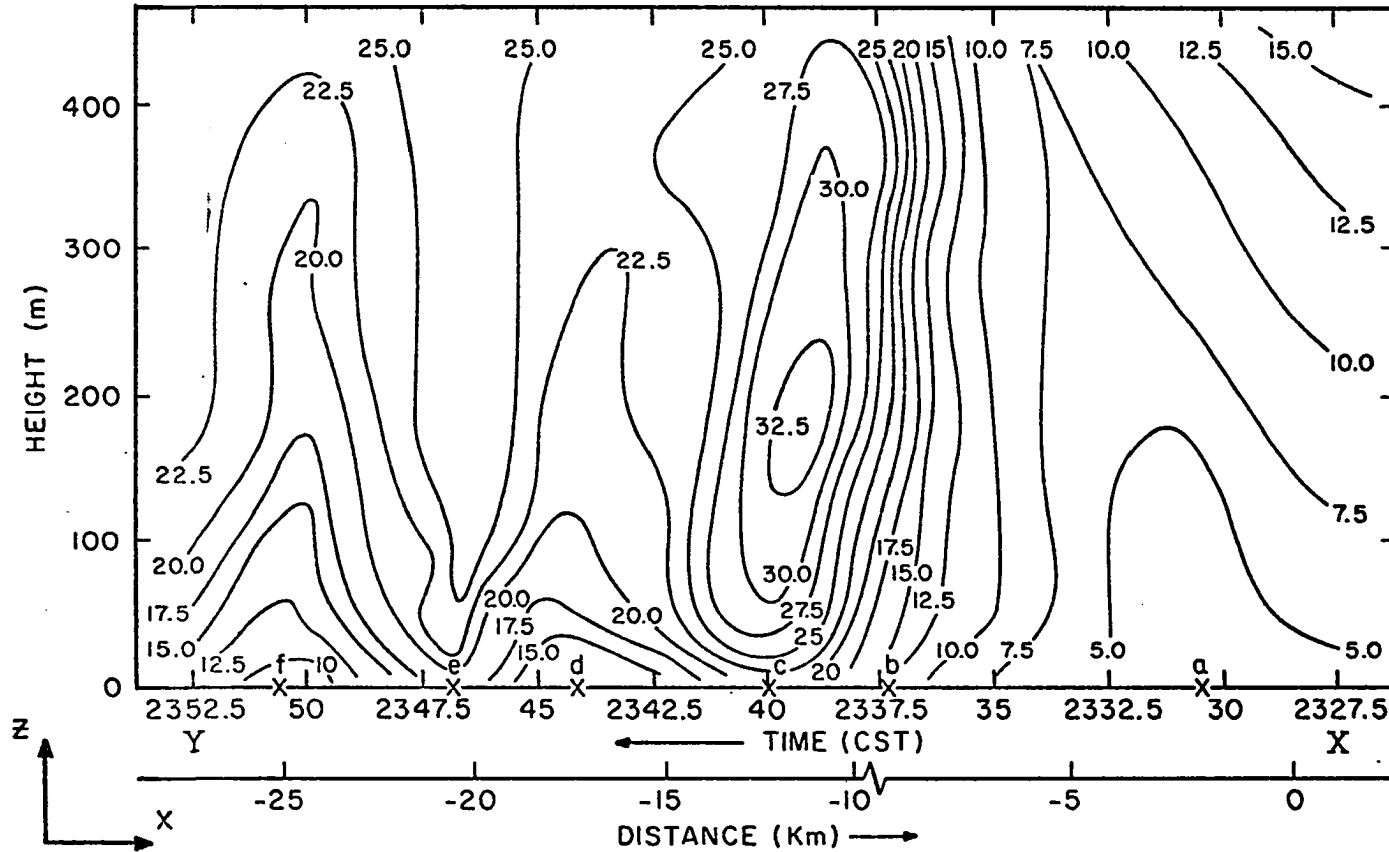


Fig. 9 cont.

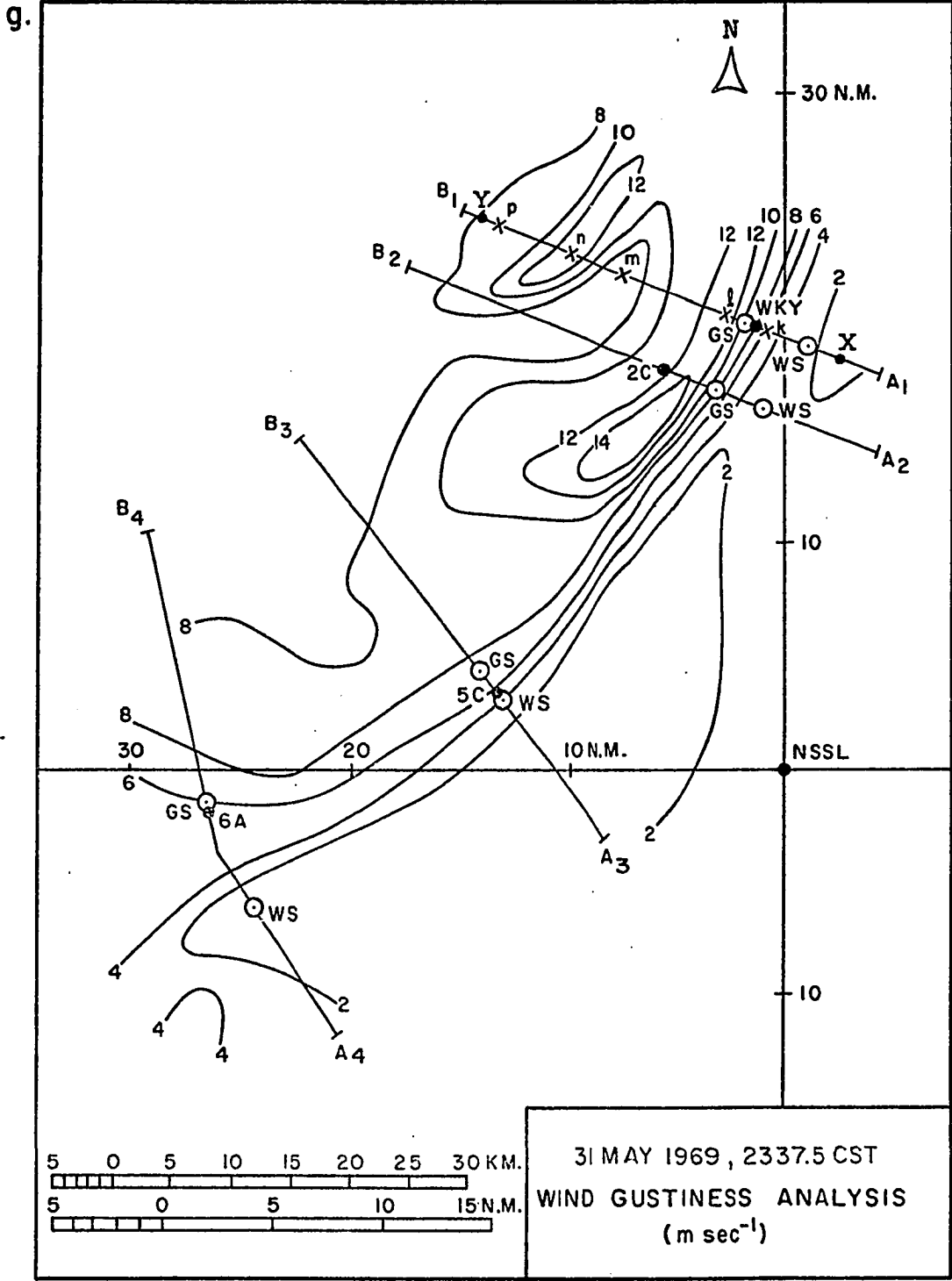


Fig. 9 cont.

h. 31 MAY 1969 , WIND GUSTINESS ANALYSIS ,  $V_{\max} - V_{\min}$  (m sec<sup>-1</sup>)

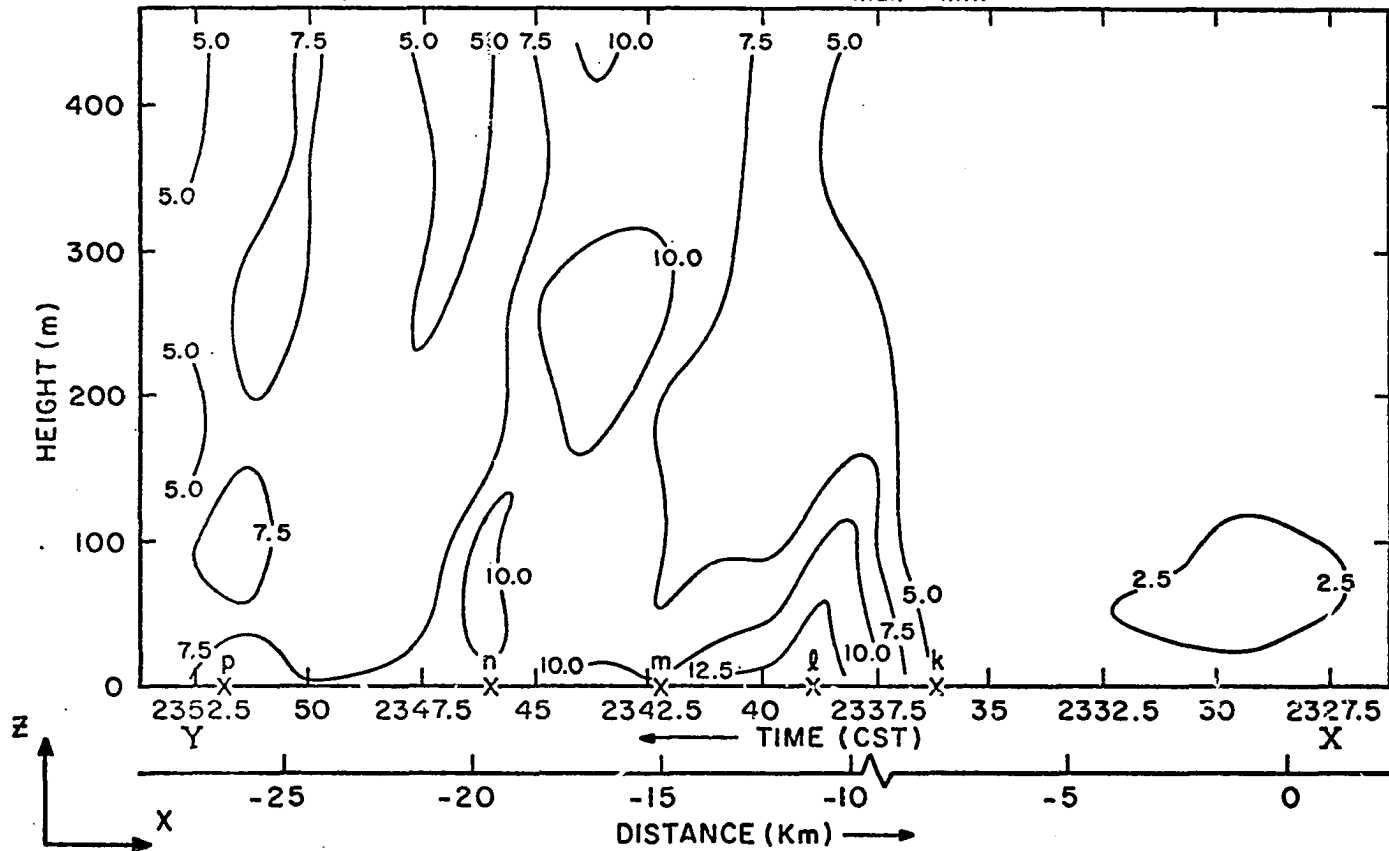


Fig. 9 cont.

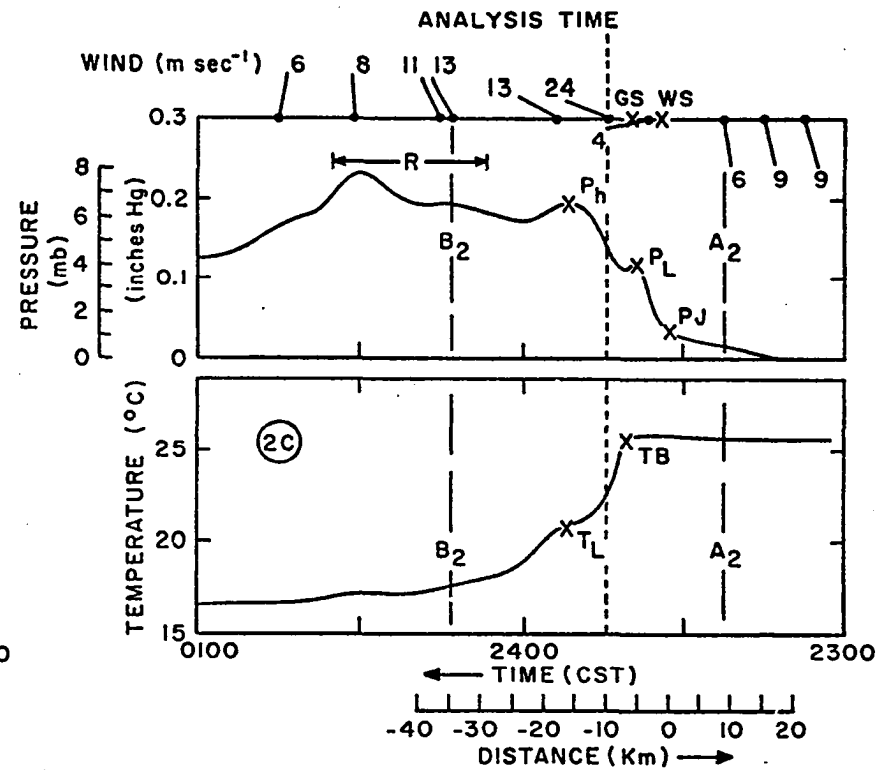
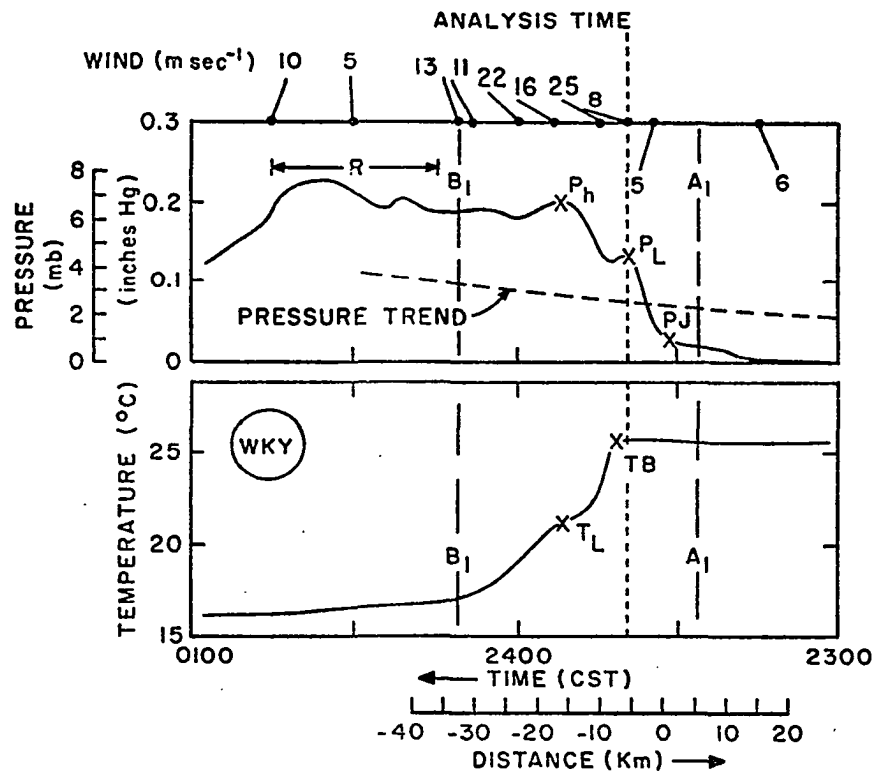


Fig. 10. Spatial variations of surface wind, pressure, and temperature at stations WKY, 2C, 5A, and 6A. The pressure trend for WKY is shown (dashed). The segments A<sub>1</sub>B<sub>1</sub>, A<sub>2</sub>B<sub>2</sub>, etc., span the surface network as shown in Figs. 9, 11, and 12. The significant features labeled in the wind (Fig. 9), temperature (Fig. 11), and pressure (Fig. 12) fields are also indicated above. The significant points in the pressure and temperature profiles denote: P<sub>J</sub>-pressure jump, P<sub>L</sub>-temporary leveling off period in the pressure curve, P<sub>h</sub>-pressure head (P<sub>h</sub>', if very weak), TB-temperature break, and T<sub>L</sub>-temporary leveling off period in temperature curve. The position of heavy surface rain is denoted "R".

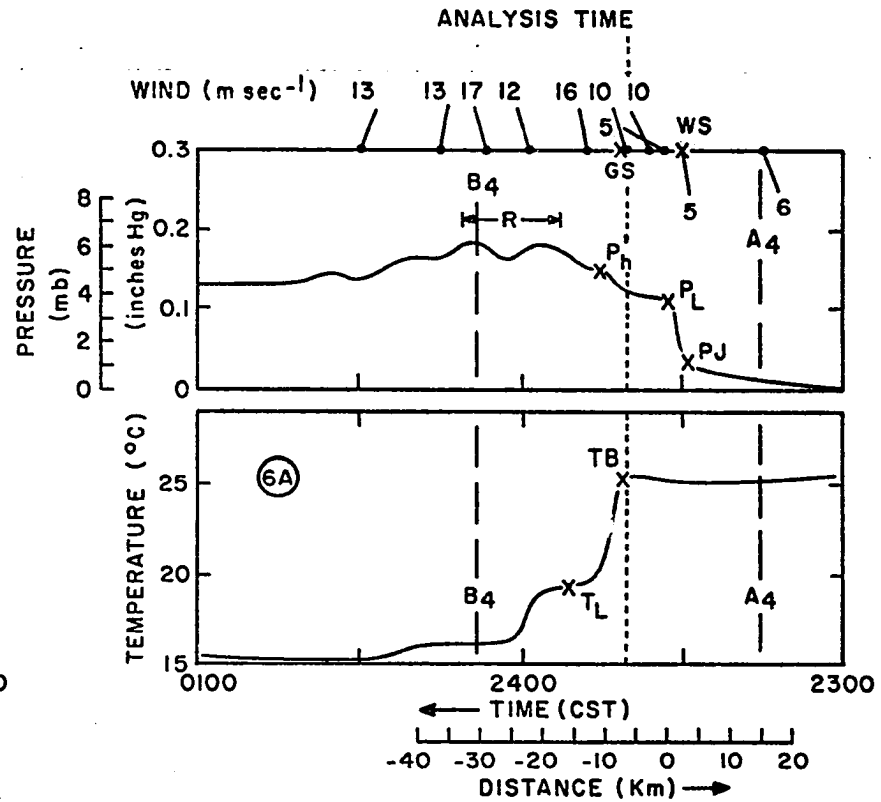
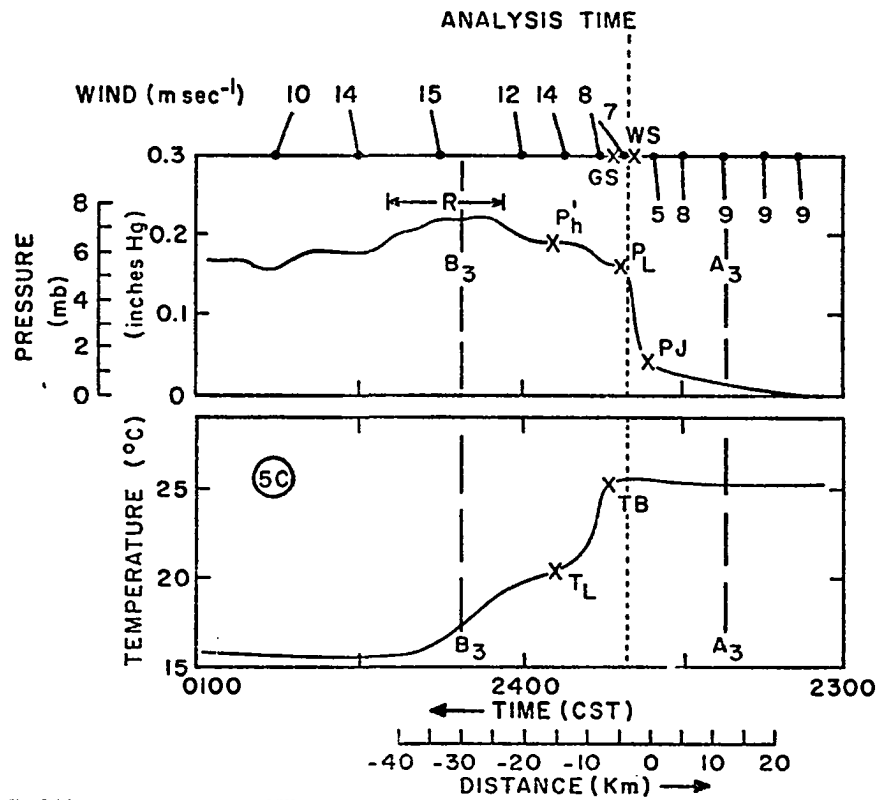


Fig. 10 cont.

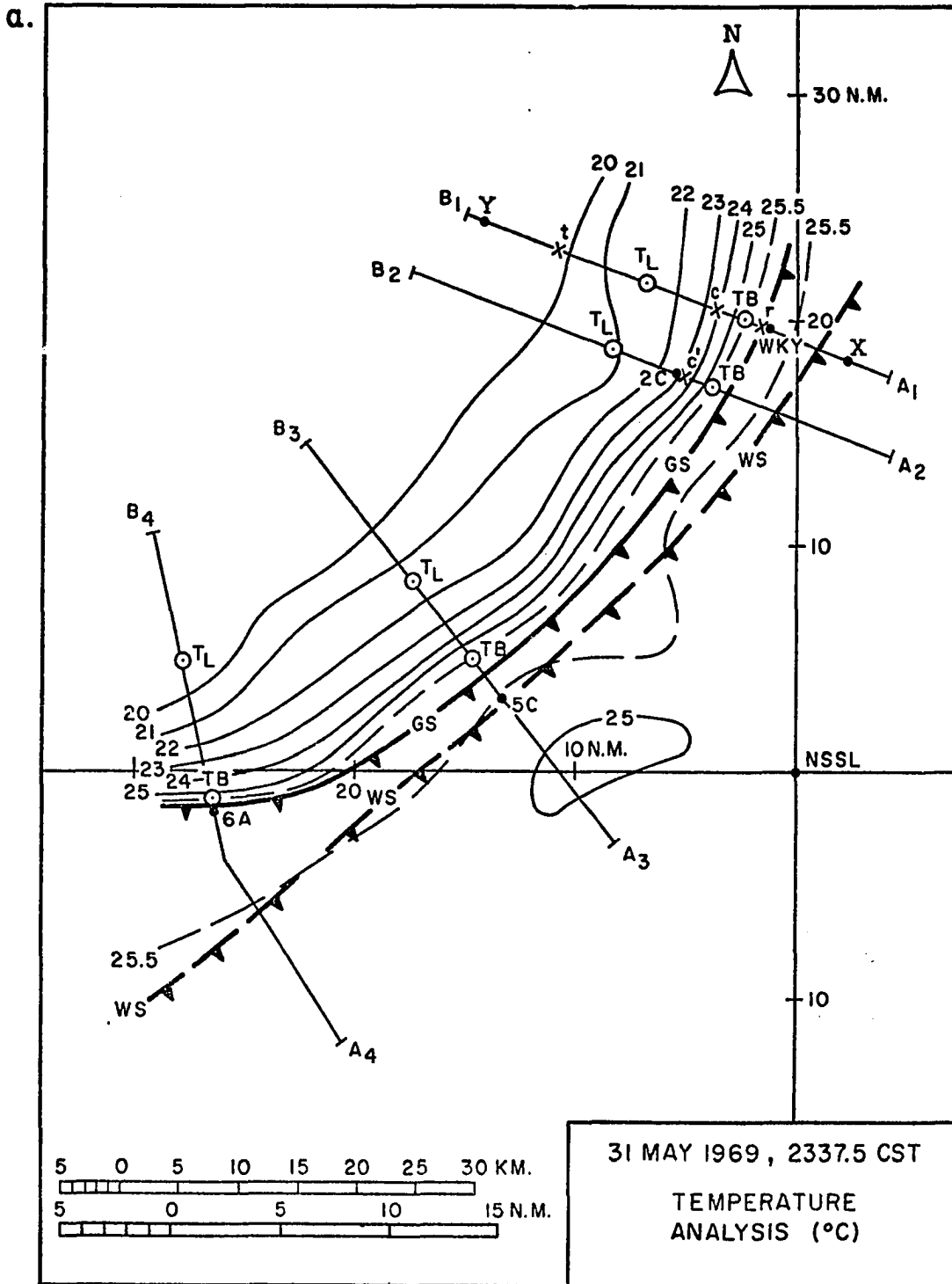


Fig. 11. Network and tower temperature analyses. Significant features are marked and labeled on the respective fields as before. See Fig. 10 for the recorded temperature variations at particular network stations.

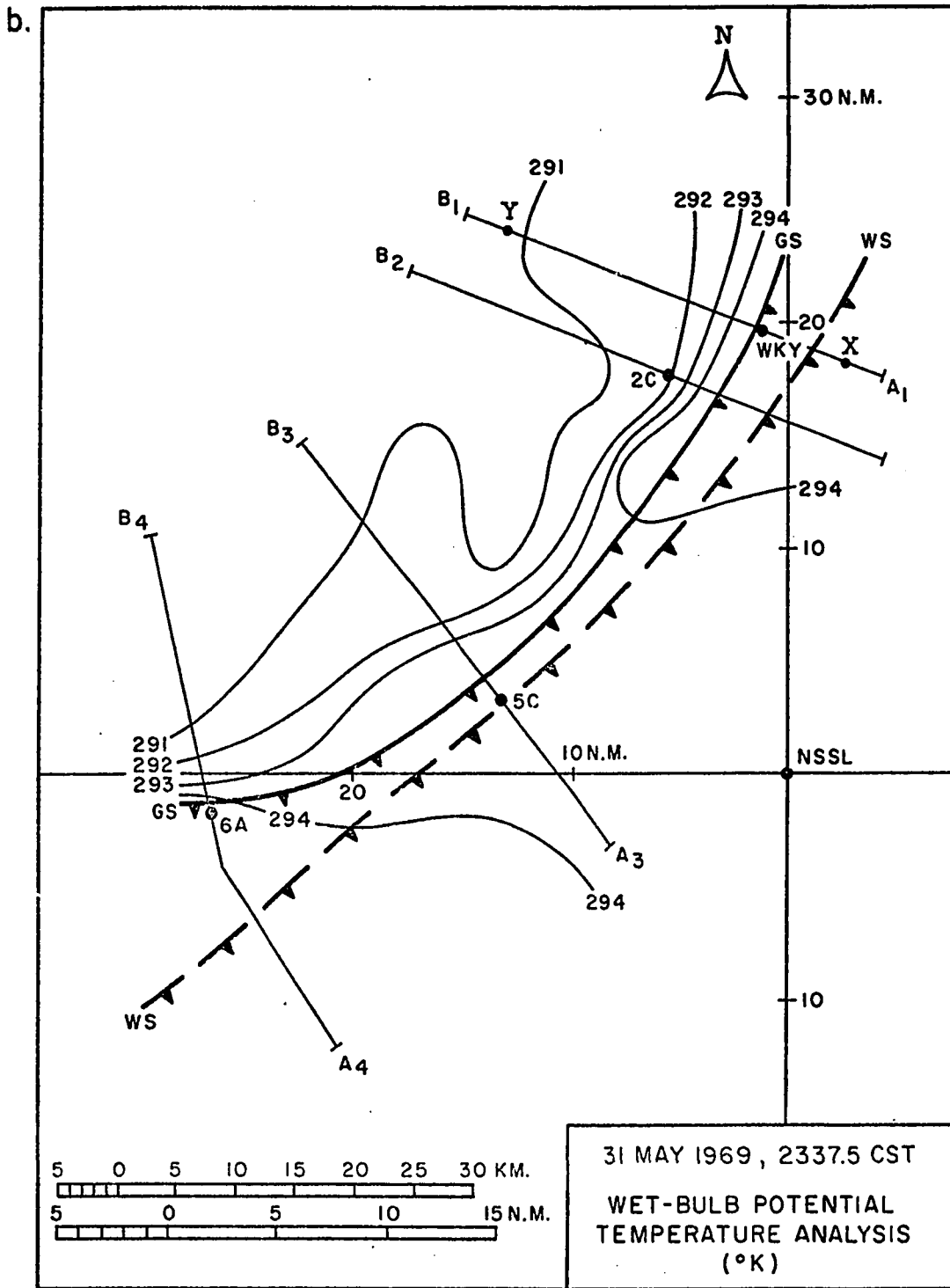


Fig. 11 cont.

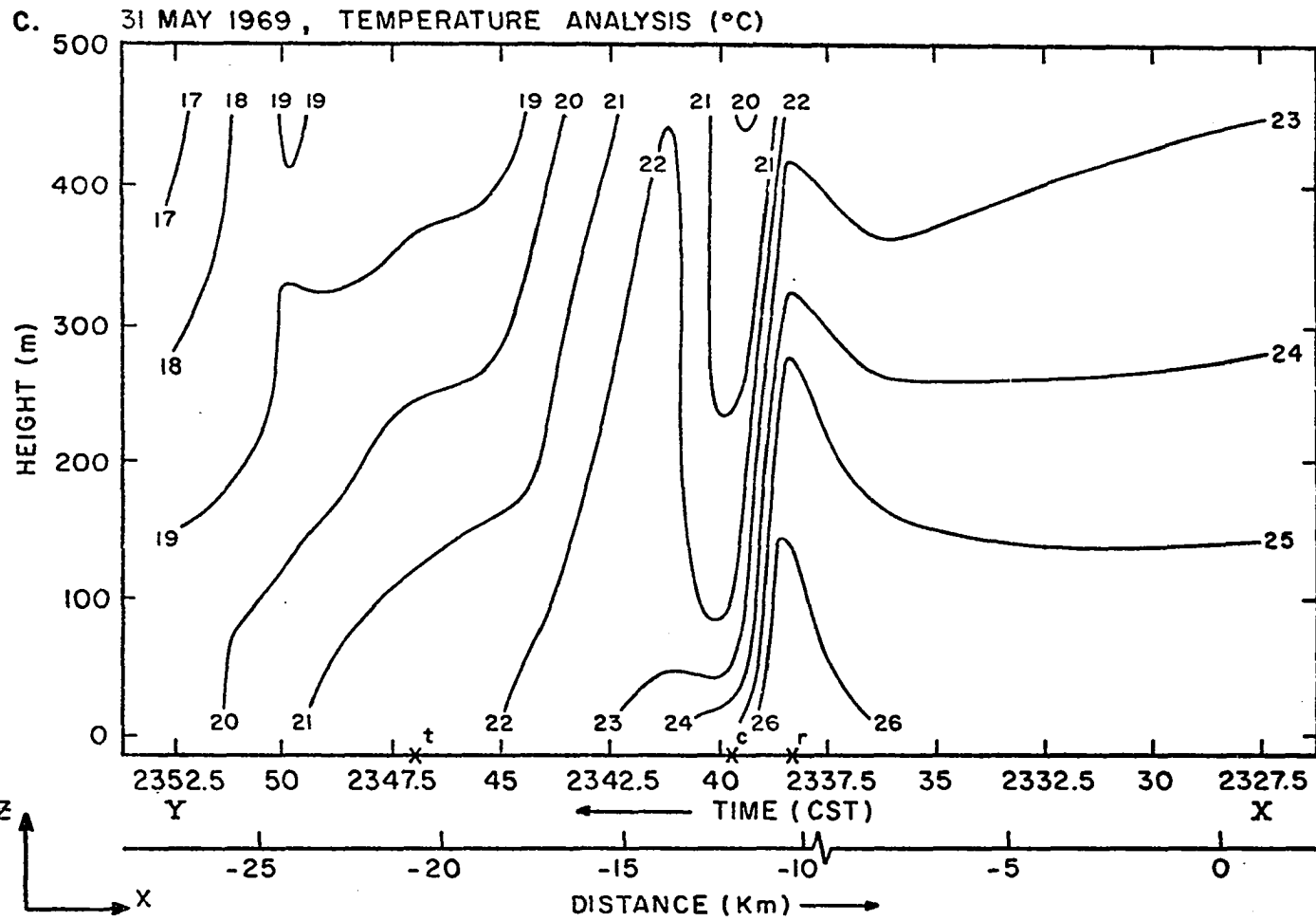


Fig. 11 cont.



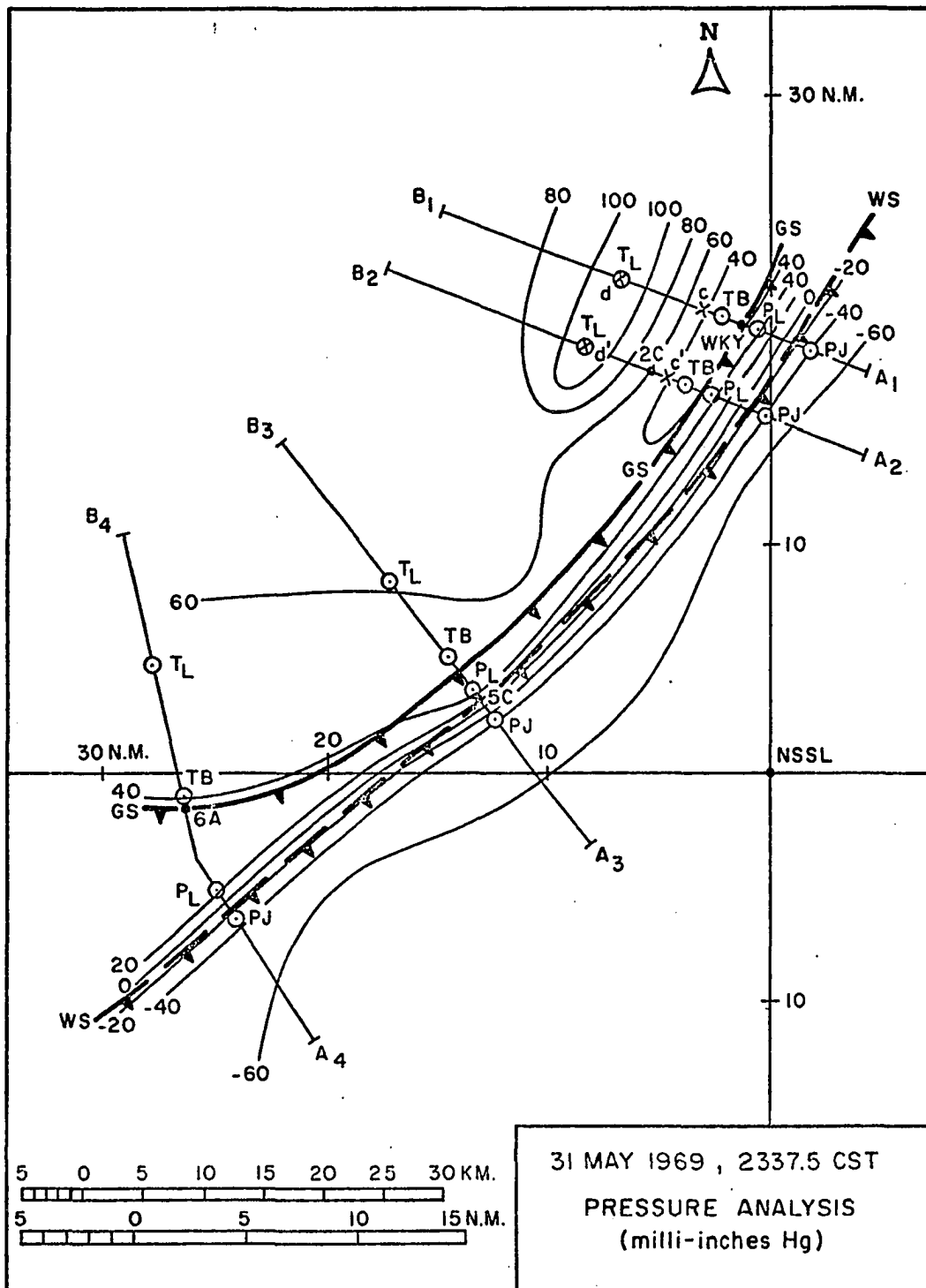


Fig. 12. Surface pressure analysis. The pressure values are deviations from the large scale pressure trend (shown for WKY in Fig. 10). Significant features in the wind speed analysis (Fig. 9e and 9f), temperature analysis (Fig. 11), and spatial pressure variations (Fig. 10) are marked and labeled identically in the above pressure field.

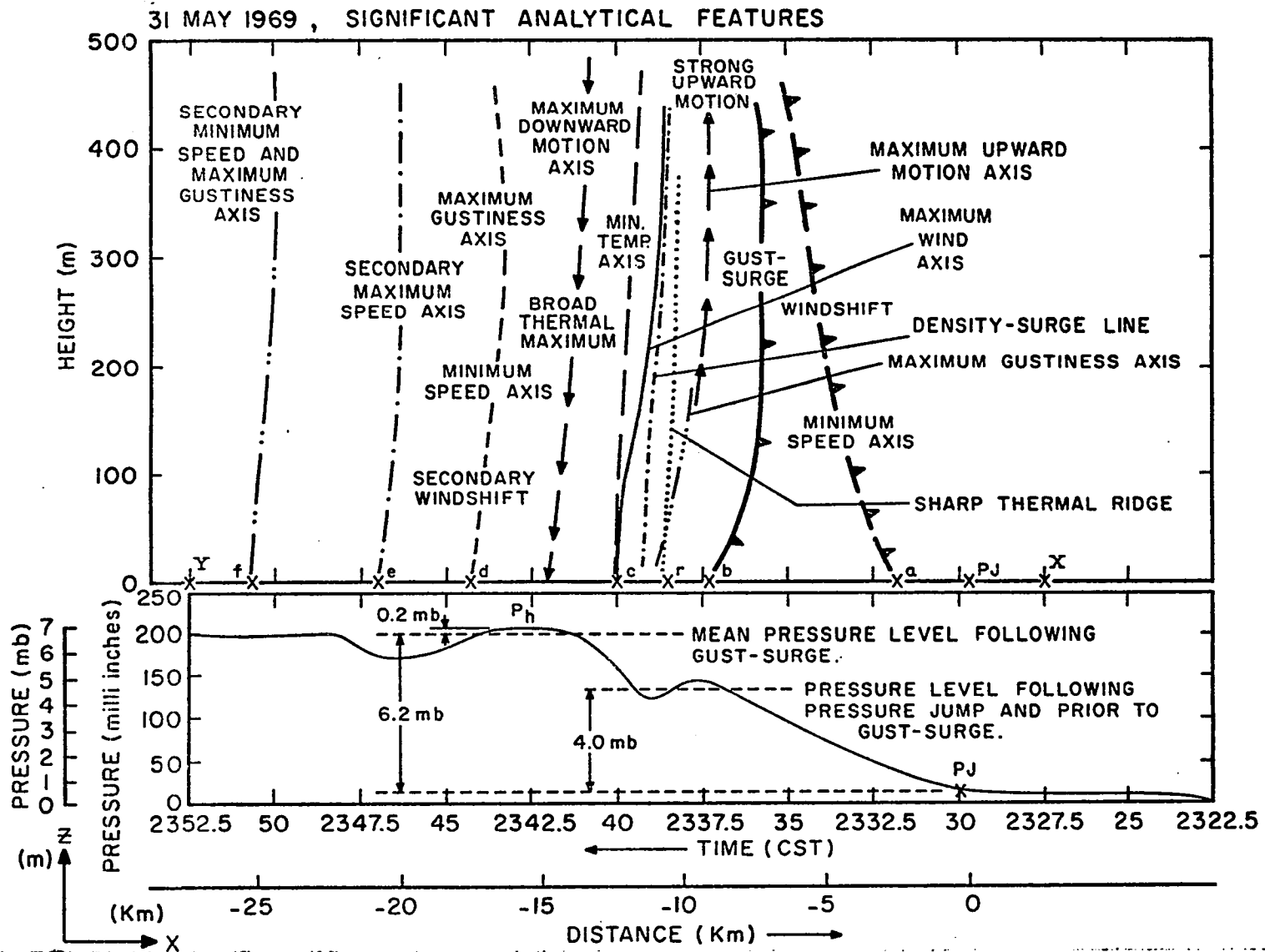


Fig. 13. Schematic of the important analytical features of the wind and thermal structure of the windshift and gust front at WKY (upper). The surface pressure profile at WKY is also shown (lower).

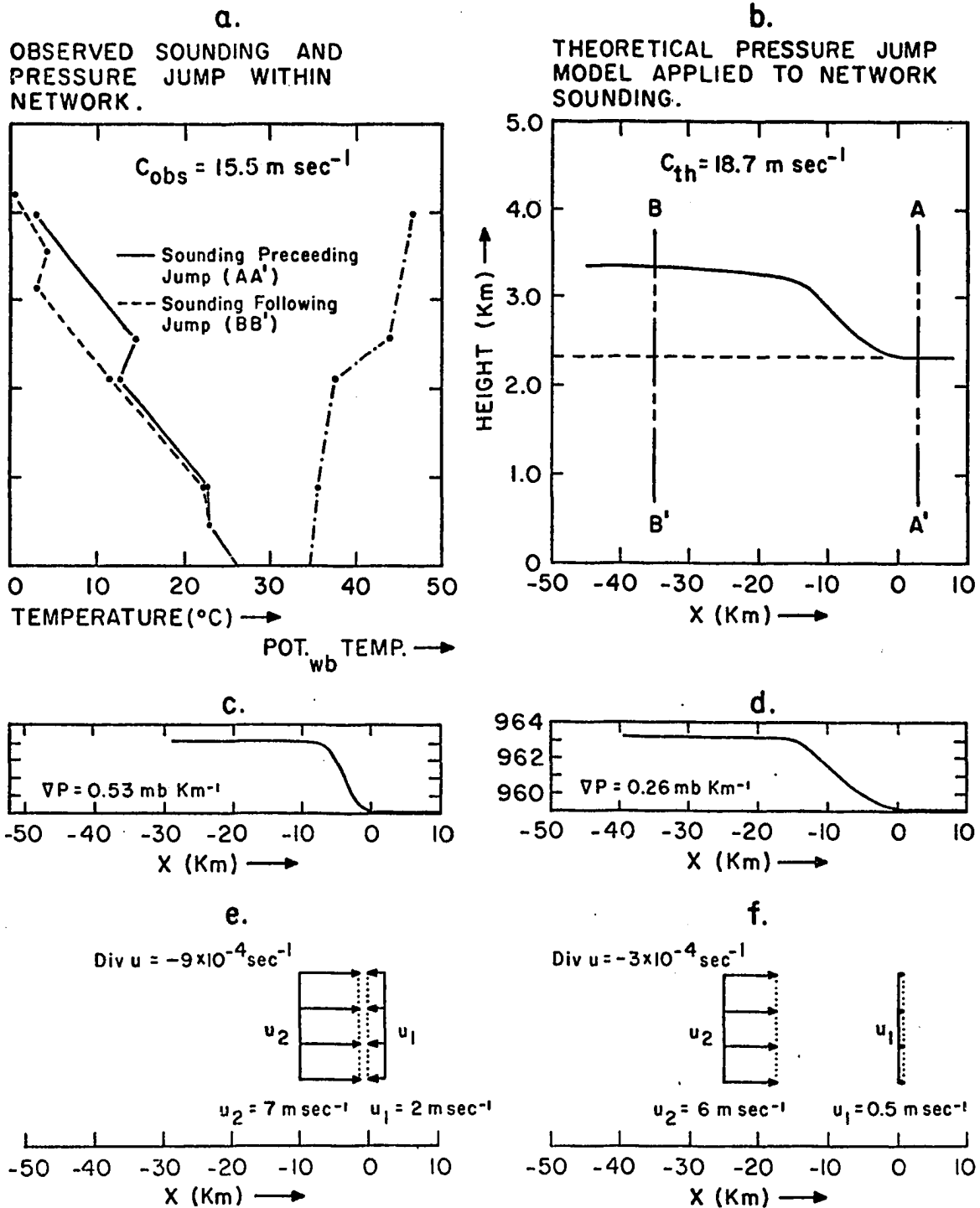


Fig. 14. Comparison of the observed and theoretical pressure jump of 31 May 1969. (a) Ambient and wet-bulb potential temperature profiles obtained from the 1800 CST TIK rawinsonde modified in the lowest 500 m for the WKY tower conditions at 2300 CST. (b) Profile of the thermal inversion through the gravitational wave "jump" as obtained by application of Tepper's (1955) pressure jump model to the inversion layer shown in (a). (c) Typical surface pressure profile through the observed pressure jump. (d) Computed hydrostatic pressure profile at the surface beneath gravitational wave in (b). Windshift across the observed (e) and theoretical (f) pressure jump.

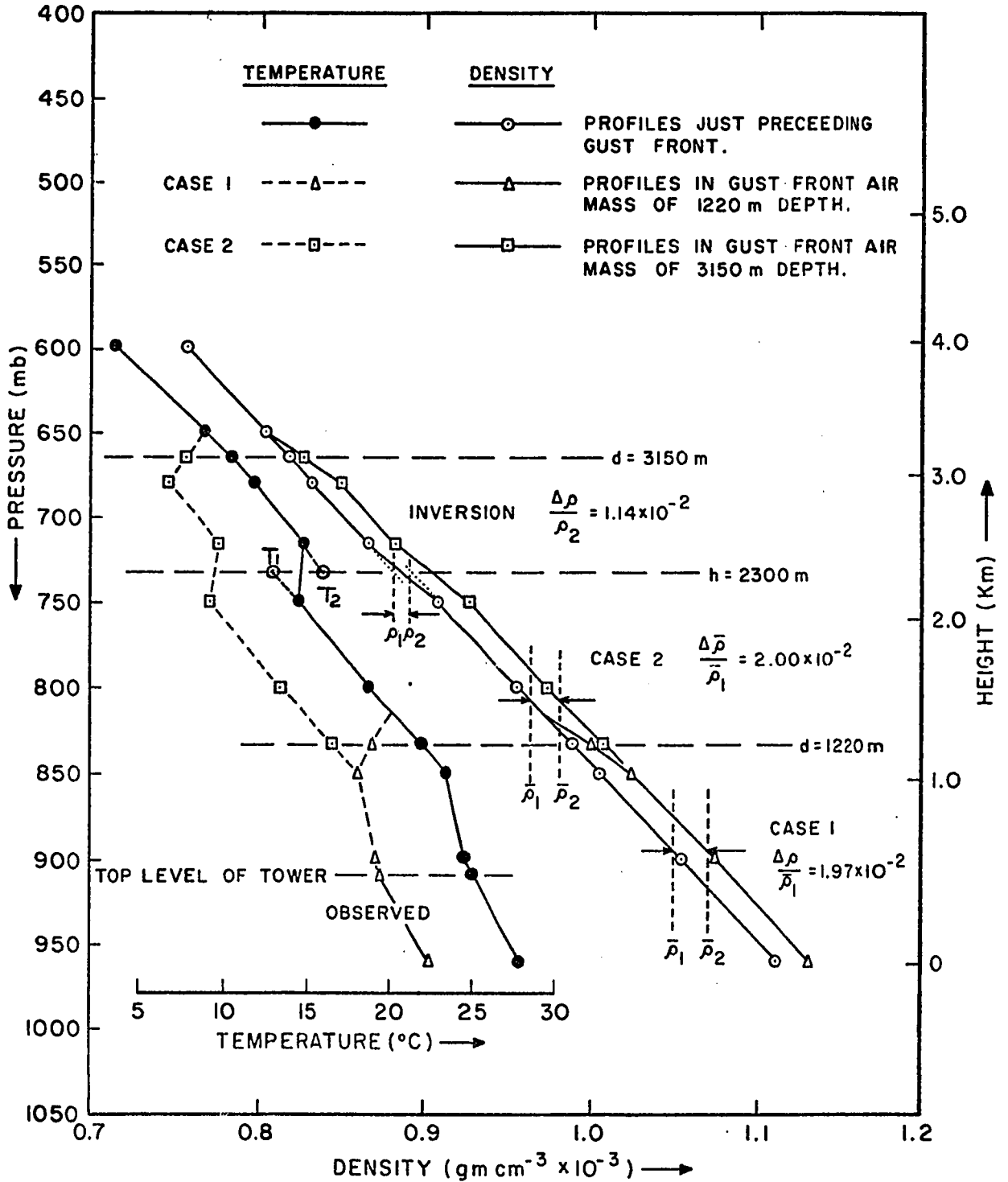
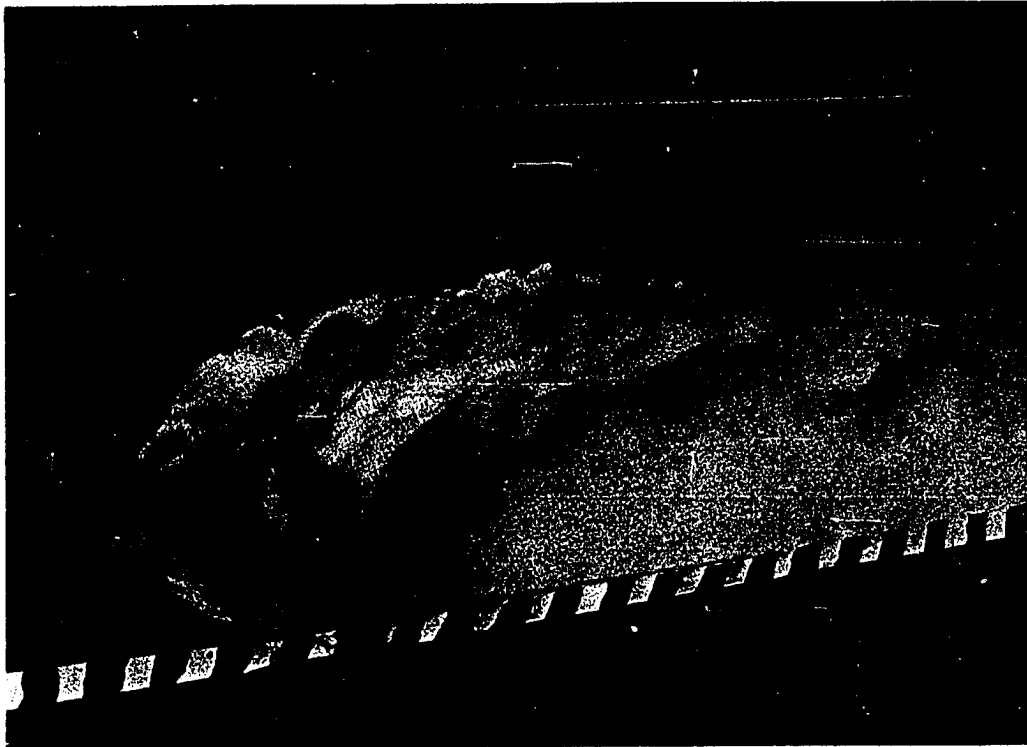


Fig. 15. Vertical profiles of temperature and density at WKY just prior to and just following passage of the gust surge, 2300 and 2345 CST, respectively.

a.



b.

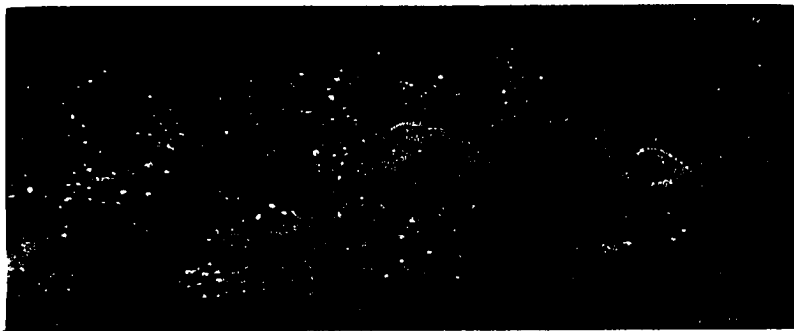


Fig. 16. (a) A saline "density current" (gravity current) propagating from right to left along the bottom of a transparent tank filled with pure water. Give attention to the slightly elevated head and the turbulent mixing in its wake. (b) A saline current (flowing from left to right) revealing the formation of bulges which are swept backwards and roll up in the form of billows and then break up (after Simpson, 1969).

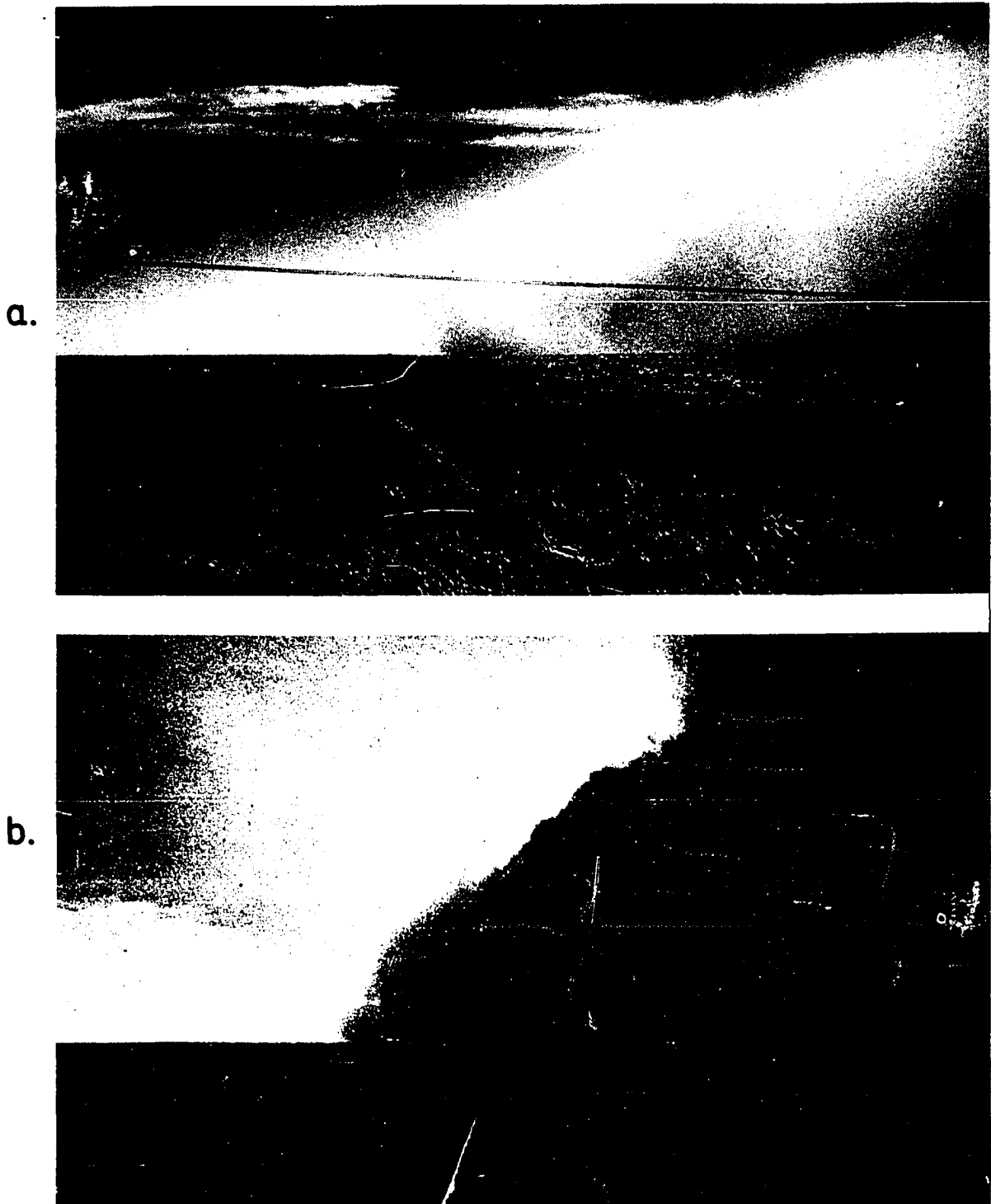


Fig. 17. Atmospheric gravity currents. (a) Cold front in Kansas (courtesy of Yih, 1969). (b) Haboob in Sudan (courtesy of Simpson, 1969). The haboob is usually found just ahead of an active or dissipating squall line but a few cases have revealed it to be associated with a strong dry cold front. In both (a) and (b) the front is moving from right to left.

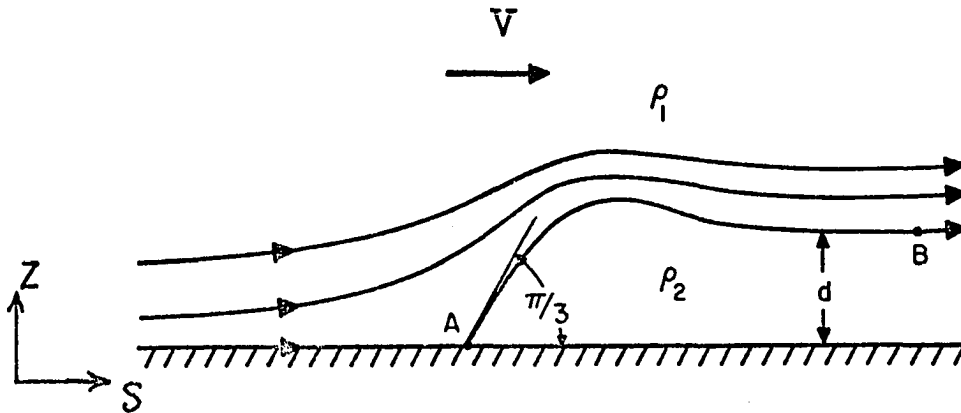


Fig. 18. Schematic flow model of a gravity current relative to a coordinate axis translating to the left with the speed of the current,  $V$ . In this system the gravity current is stationary while the ambient fluid flow is towards the right at speed  $V$ .

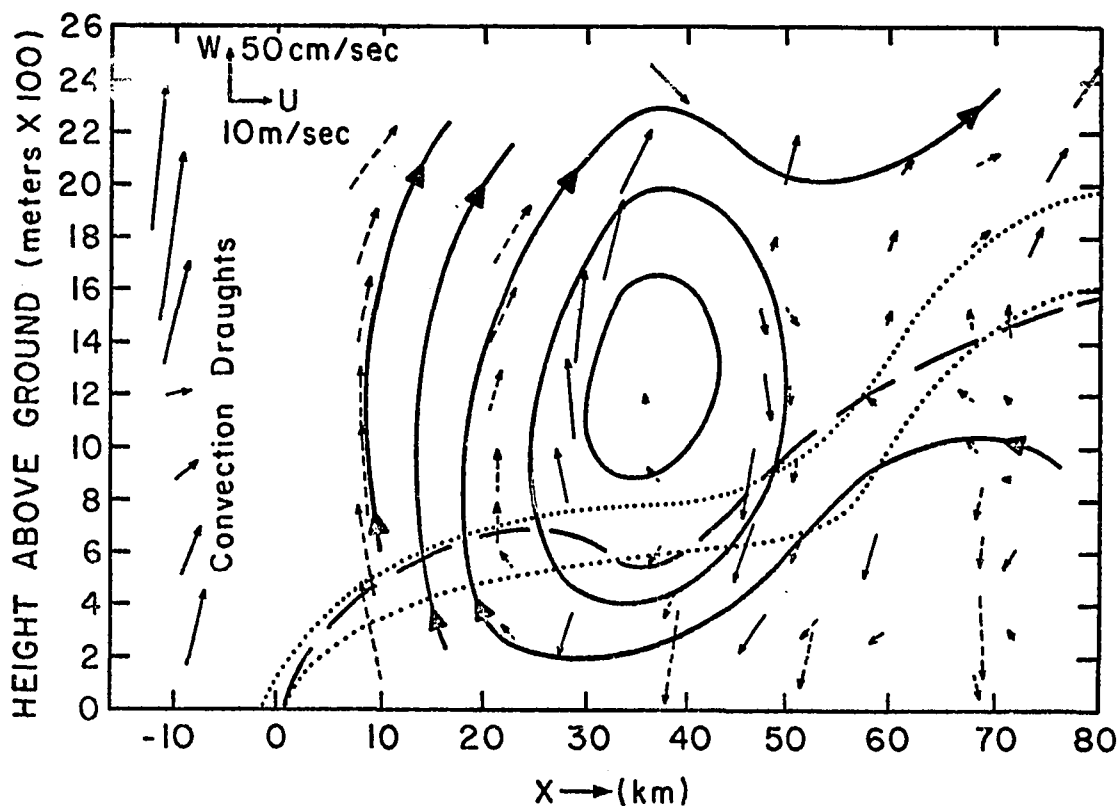


Fig. 19. A composite analysis of the wind field near the leading edge of a cold front in Australia (after Berson, 1958). The dashed and dotted curves represent zones of maximum vertical wind shear (assumed to correspond approximately to the frontal surfaces) for a single front as determined from "pibal" wind measurements at three different locations. Note the dip or level region in the shear profiles in the vicinity of 40 km from the leading edge of the front. The flow pattern is depicted relative to a coordinate axis translating to the left along with the frontal boundary. The streamlines are drawn roughly to fit the plotted wind vectors.



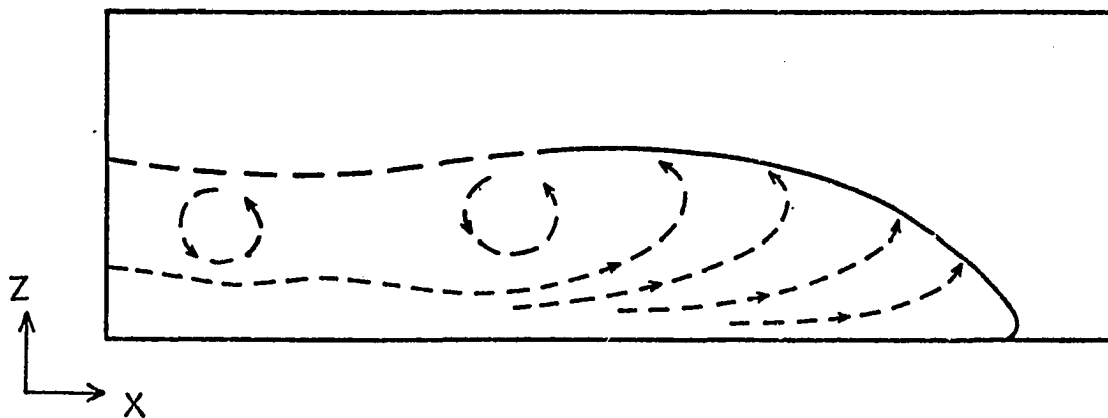


Fig. 20. Internal circulation pattern of laboratory gravity currents as seen by a coordinate axis translating to the right with the speed of the head (after Middleton, 1966).

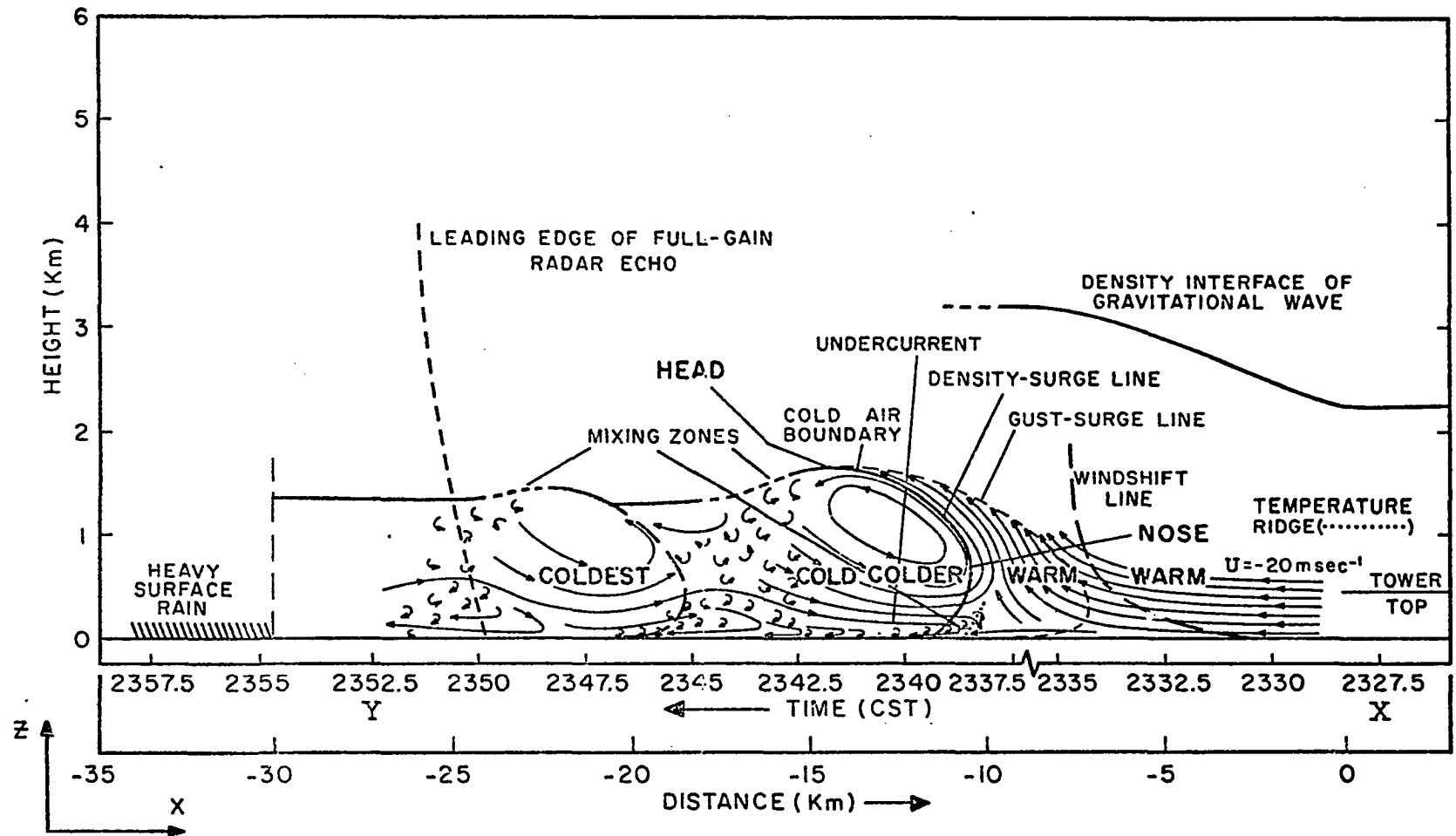


Fig. 21. A composite schematic model combining the features of the analyzed and deduced structure of the windshft and gust front leading the squall line of 31 May 1969 (See the text for discussion).